ABSTRACT

Title of Document: THERMOPHYSICAL PROPERTIES AND BOILING HEAT TRANSFER OF SELF-ASSEMBLED NANOEMULSION FLUIDS.

JIAJUN XU, Doctor of Philosophy, and 2013

Directed By: Associate Professor, Bao Yang, and Department of Mechanical Engineering

Recently, society has witnessed a blossom of the development of electronics, communications, and auto-computing industries, and this trend is going to continue through this century. The power dissipation density has been increased drastically because of the continuous miniaturization and the multiplication of speed of operation and data transfer. Today, it is not unusual to see heat fluxes of 200 W/cm^2 in a power module, a figure that is expected to increase up to 1000 W/cm^2 in the near future. Thermal management of such high flux is quickly becoming the bottleneck to improvements in electronic and optoelectrical devices. Most efforts to improve thermal management technology in the past has been devoted to improving transport

processes, such as jet impingement, and microchannels. Much less attention has been paid to the fact that the existing fluids themselves possess poor thermal transport properties.

In this study, Nanoemulsion fluids have been developed to overcome barriers of state-of-the-art heat transfer fluids via forming self-assembled liquid nanodroplets in conventional heat transfer fluids to elevate their heat transfer capability. A systematic investigation on nanoemulsion fluids especially their applicability in thermal management of high heat flux devices was done on the following topics: (a) the preparation of several nanoemulsion heat transfer fluids and their inner structure characterization; (b) investigation of thermophysical and phase change heat transfer characteristics in both pool boiling and flow boiling conditions; (c) optimization of nanoemulsion fluids for better thermal performance and to identify the influence of different dispersed phase, base fluid and surfactants and their concentration, on (1) inner structure and thermophysical properties, and (2) on the phase change heat transfer characteristics; (d) analytical/numerical modeling and simulation of the nanoemulsion fluids and their enhanced thermophysical properties.

Overall, nanoemulsion fluids with greatly enhanced heat transfer properties, especially, the phase change properties has been developed and demonstrated here. Potential applications and the future of nanoemulsion fluids are discussed too.

EXPERIMENTAL AND THEORETICAL STUDY OF THERMOPHYSICAL PROPERTIES AND BOILING HEAT TRANSFER OF SELF-ASSEMBLED NANOEMULSION HEAT TRANSFER FLUIDS.

By

JIAJUN XU

Dissertation submitted to the Faculty of the Graduate School of the
University of Maryland, College Park, in partial fulfillment
of the requirements for the degree of
Doctor of Philosophy
2013

Advisory Committee:
Associate Professor Bao Yang, Chair
Professor Ashwani Gupta
Assistant Professor Amir Riaz
Senior Lecturer Chandra Thamire
Associate Professor Kennth Yu (Dean's representative)

Dedication

To my wife Pearl, my son Francis, my parents and my parents-in-law.

Acknowledgements

I would like to thank my advisor, Dr. Bao Yang for his guidance, support, and encouragement through the last four years. I would also like to thank Dr. Ashwani Gupta, Dr. Amir Riaz, Dr. Chandra Thamire, and Dr. Kenneth Yu for serving on my dissertation committee, reviewing my dissertation and giving me valuable suggestions.

I would like to thank Dr. B Hammouda for helping me conduct the SANS experiments and Dr. Xinan Liu for aiding me during bubble dynamics imaging.

Table of Contents

List of Tables

List of Figures

Nomenclature

Acronyms and Abbreviations:

AC	Alternating Current
CHF	Critical Heat Flux
DA	Change in interfacial area
DG	Free energy of formation
DS	Change in entropy of the system
DEB	Aromatic
DC	Direct Current
DLS	Dynamic Light Scattering
EMT	Effective Medium Theory
EG	Ethylene Glycol
FC	Fluorocarbons
HEC	Hydroxyethyl Cellulose
HC	Hamilton-Crosser model
HTC	Heat Transfer Coefficient
HJ	Hasselman-Johnson model
HTFs	Heat Transfer Fluids
ONT	Onset of Nucleate Boiling
PAO	Polyalphaolefin
PCMs	Phase-Change Materials
PEO	Polyethylene Oxide

PG	Propylene glycol
ROM	Rule of Mixture
SAS	Small Angle Scattering
SAXS	Small Angle X-ray Scattering
SANS	Small Angle Neutron Scattering
T	Temperature
TEM	Transmission Electron Microscopy
NBHTC	Nucleate Boiling Heat Transfer Coefficient

Symbols:

A	Area, m^2
$A+$	Coefficient
B+	Coefficient
C	Constant
C_f	Heat capacity, kJ/kg
Db	Diffusivity
D	Diameter,m
F	Force, N
G	Interfacial thermal conductance, W/K
G_T	Temperature gradient, K/m
h	Convective heat transfer coefficient, $W/m^2.K$
h_b	Boiling Heat Transfer Coefficient, , $W/m^2.K$
$I_{current}$	Electrical current, A

I	Intensity
k	Thermal conductivity, W/m.K
k_B	Boltzmann constant, m^2 kg s^{-2} K^{-1}
K	Constant
L	Length, m
m	Mass, kg
n	Constant
Nu	Nusselt number
P	Electrical power, W
P_r	Prandtl number
q	Wave vector, m^{-1}
r	Radius, m
$\mathbf{r}$	Radius, vector
R_a	Rayleigh number
Re	Reynolds number
R_h	Hydrodynamic radius, m
R_k	Kapitza resistance, K/W
t	Time, s
T	Temperature, K
V	Voltage, V
Vol	Volume, m^3

Greek Letters:

k	Thermal conductivity ratio

ρ	Density, kg/m^3
ϕ	Volume fraction, R
μ	Dynamic viscosity, Pa.s
ν	Kinematic Viscosity, Pa.s
σ	Surface Tension, N/m
τ	Delay Time, s
ω	Frequency, Hz
η	Constant
δ	Uncertainty

Subscripts

b	Boiling
CHF	Critical Heat Flux
d	Departure
f	Fluid
fg	Fluid to gas phase change
g	Gas
l	Liquid
LG	Liquid-gas
s	Solid
sat	Saturation
sf	Solid to fluid
SG	Solid-gas

SL	Solid-liquid
W	Wall

Chapter 1: Introduction

Motivation:

Cooling is one of the most important technical challenges faced by a range of diverse industries: microelectronics, optoelectronics, and, especially, power electronics [1-8]. This technology gap is the result of the higher frequencies and component densities of today's electronics and the higher currents and switching frequencies of new power electronics. The advances in semiconductor materials and more precise fabrication techniques have the unfortunate side effect of generating higher amounts of waste heat within a smaller volume. Today, it is not unusual to see heat fluxes of 200 W/cm^2 in a power module, a figure that is expected to increase over 1000 W/cm^2 in the near future. [1, 3-7]. Two ranges of heat flux can be loosely identified relative to the magnitude of the heat dissipation and the type of coolant permissible in a particular application. These are the high-flux range, with cooling heat flux requirements on the order of 10^2-10^3 W/cm^2, and the ultra-high-flux range, with heat fluxes of 10^3-$10^5 W/cm^2$. How to dissipate such high heat flux with limited space efficiently has become one of the challenging problems nowadays.

Thermal management of such high flux is the bottleneck of improvements in electronics and power electronics. The need for higher capacity and more complex cooling systems is limiting the full potential of the advances in electronics and power electronics. One solution is the development of novel improved heat transfer systems and their kernel components. One important component of these heat transfer systems

that has received little attention is the cooling fluid used inside. The inherently poor heat transfer properties of some of the coolants, lubricants, oils, and other heat transfer fluids used in today's thermal systems limit the capacity and compactness of the heat exchangers that use these fluids. Therefore, there is an urgent need for innovative heat transfer fluids with improved thermal properties over those currently available.

In this study, it is intended to introduce some recent developments in another type of engineered phase changeable heat transfer fluids, in which nanostructured elements made of phase change materials (PCMs) are introduced to increase the effective heat capacity of the base fluids [9-16]. This paper starts with the discussion on the introduction of nanoemulsion fluids, which can be liquid-vapor PCM fluids or liquid-solid PCM fluids, depending on the phase transition behavior of dispersed phase [9-13, 15]. It is followed by discussion on characterizing their thermophysical and boiling heat transfer properties. Both material synthesis and property characterization of these nanostructured phase changeable fluids will be covered. In these fluids, the phase changeable elements formed inside are typically smaller than 50nm in size, and remain stable during phase transition.

This study is not intended to serve as a complete description of all phase changeable fluids available for heat transfer applications. The selection of the coverage was influenced by the research focus of the author and reflects his assessment of the field.

Approaches Currently Available

Improving transport processes

Lots of effort to improve heat removal capability has been devoted to improving transport processes[17, 18] in the past, such as using single-phase convection in small-diameter channels[19], single-and two-phase flow in porous media, and two phase flow in microchannels. In order to achieve high heat flux cooling using single-phase convection, high inlet pressure is required to force the working liquid; and with high heat flux, the temperature increase along the length of the microchannel is significant. Both of these effects place stress on the chips.

Two-phase cooling

Due to the need of high-flux dissipation, two-phase cooling is also widely used. One method of removing high heat flux density is to use immersion cooling, with phase change of a dielectric liquid coolant on the chip surface. However, the most significant problem is that the heat transfer fluid of choice: common heat transfer fluids have inherently poor thermophysical properties and especially their phase change properties[20, 21]: they either have too high saturation temperature or have low saturation temperature, and usually have very low critical heat flux (CHF), typically below 100W/cm^2.

Similar to single-phase heat transfer, some improvement in CHF can be obtained through the use of more complex geometries, such as arrays of micro-jets directed into the microchannels[22]. However, changes in geometry alone produce only

modest improvements in CHF; more significant improvements have been demonstrated only by cooling the refrigerant to well below room temperature and by allowing the surface temperature to exceed safe operation temperature.

Another constraint in using conventional heat transfer fluid is due to the stringent material and electrical compatibility requirements in applications that prohibit the use of water in direct contact with current-carrying components. It appears that none of the approaches mentioned above can solve the demanding heat dissipation problem, thus, innovative cooling solution is urgently needed. The most common heat transfer fluids are listed here in Table 1.1. Among them, many successful heat transfer solutions involve direct fluid contact or spray cooling using a dielectric fluid, such as, Polyalphaolefin (PAO), a highly branched, compact, and very stable synthetic hydrocarbon that offers exceptional heat transfer performance over a wide temperature range.

Table 1.1 Common heat transfer fluids

Coolant	Freezing Temp (oC)	Flash Temp (oC)	Viscosity (Kg/m/s)	Thermal Conductivity (W/m/k)	Specific Heat (J/kg/K)	Density (kg/m3)
Aromatic (DEB)	<-80	57	0.001	0.14	1700	860
Silicate-ester(coolanol 25R)	<-50	>175	0.009	0.132	1750	900
Polyalphaolefin (PAO)	<-50	>175	0.009	0.137	2150	770
Silicone	<-110	46	0.0014	0.11	1600	850
Fluorocarbon	<-100	None	0.0011	0.06	1100	1800
EG/Water (50:50 v/v)	-37.8	None	0.0038	0.37	3285	1087
Ethanol/Water 40:60 (wt/wt)	-40	29	0.002	0.4	3560	935
PG/Water 50:50 v/v	-35	None	0.0064	0.36	3400	1062

Adding solid, highly conductive particles

Other approaches such as the strategy of adding solid, highly conductive particles to improve thermal conductivity of fluids has been pursued since Maxwell's theoretical work was first published more than 100 years ago [23]. Early studies were confined to millimeter or micrometer-sized solid particles dispersed in fluids. In the past decade, researchers have focused on suspensions of nanometer-sized solid particles, known as nanofluids [1-4, 8, 14, 24-63]. In general, the application of nanofluids in heat transfer area focuses on three important directions: thermal conductivity[1, 2, 4, 24, 26, 28, 30, 37, 39, 52, 53, 64], convective heat transfer[1, 32, 38, 44, 58, 59, 64], and boiling heat transfer[14, 34, 43, 44, 54, 56, 58, 59, 61]. Thermal conductivity, the most important parameter responsible for enhanced heat transfer, has been extensively studied. Many research reported a high thermal conductivity enhancement with nanofluids, even in the case of very small particle volume fractions. Some of them reported abnormal increase of thermal conductivity. Recent work from International Nanofluid Property Benchmark Exercise (INPBE) started a benchmark work on the thermal conductivity of nanofluids, and their data analysis reveals that the thermal conductivity of nanofluids increase with particle concentration and aspect ratio while the effective medium theory can well explain the experimental data; no anomalous enhancement of thermal conductivity was achieved [4]. For convective heat transfer, most of the study report enhancement in heat transfer rate in different nanofluids. However, some inconsistent behavior were reported that the heat transfer coefficient can be lower than base fluid under certain nanoparticle loading which suggests that the particle shape or aspect ratio is an important factor to determine the

thermal performance of nanofluids apart from the effective thermal conductivities[31, 32, 65]. Boiling heat transfer using nanofluids has also received lots of attention, especially the peak heat flux or called critical heat flux. As the nanoparticles can increase the thermal conductivity of base fluids, it is widely expected that the boiling heat transfer would be enhanced as well. However, inconsistent experimental results about boiling heat transfer coefficient of nanofluids were reported while the effect on critical heat flux is more consistent. However, the results are later confirmed that the CHF increase in nanofluids increased not due to the effect of the nanofluids but due to the nanoparticle deposits on the heater surface [34, 43, 47, 66, 67]. Flow boiling is becoming popular due to the emerging needs for high flux cooling of electronic components. The main issue is the clogging problem if nanofluids are to be used in microchannel systems; the surface deposition during two-phase flow is another challenge [44, 54, 62]. So far, some deeper understanding of the mechanisms behind the observed thermal properties of the nanofluids has been achieved but more research is still needed [64, 68-70].

Liquid Mixture

A number of experimental studies of boiling dilute emulsions have been performed by Bulanov and co-workers in the past 25 years [71-76]. Dilute emulsions are those in which the low boiling point liquid is the dispersed component and makes up less than 5% of the mixture by volume. They found that very high degrees of superheat are necessary to cause of dispersed component, similar to the findings of Mori et al.[77], and they reason that this is because droplets, not in contact with the heated surface,

must undergo spontaneous nucleation. They also show evidence for a boiling mode that they call chain activation of nucleation sites, in which, the explosive boiling of one highly–superheated droplets causes nearby droplets to boil as well. Early experimental studies by Bulanov et al.[71, 72] found that boiling dilute emulsions have several favorable characteristics. In these studies the low-boiling–point liquid is water, and is dispersed in oil that has high saturation temperature. In both pool and flow boiling it is found that the heat transfer coefficient is always higher for the emulsion than for the pure oil. However, one unfavorable characteristic identified in dilute emulsion boiling is the high degree of superheat required to initiate boiling of the dispersed component, often 60^{o}C or more. This suggests that the suddenness of the boiling of highly-superheated droplets is essential to the heat transfer improvement, possibly because this action causes turbulence in the surrounding liquid. He has developed some model of boiling dilute emulsions based on these experimental results to explain the nucleation process but there are some contradictory assumptions regarding to the temperature profile in the thermal boundary layer and no satisfactory explanation available yet.

Very high degrees of superheat are necessary to cause the nucleation of dispersed component. In both pool and flow boiling, it is found that the heat transfer coefficient is always higher for the emulsion than for the pure oil. Roesle et al tried liquids of different low-boiling points to lower the nucleation temperature of emulsion system[78]. Their FC72-in-Water dilute emulsion shows lower convective heat transfer coefficient and high superheat to initiate boiling as well. For the pentane-in-

water emulsion, similar trend is observed.[71-76] However, there is yet no detailed understanding of how the boiling process occurs, and the experimental data in the literature is quite limited. Another major hindrance to understanding the behavior of boiling emulsions is their opaque nature, which makes visual observation of the boiling emulsion very difficult.

Proposed Approaches

Most research on thermal fluids to date has focused on how to increase thermal conductivity. Our study will introduce the concept of using PCM particles to increase the effective heat capacity of thermal fluids. Both the heat capacity and thermal conductivity of the fluids strongly influence the heat transfer coefficient. For example, for a fully-developed turbulent flow of a single-phase fluid, the convective heat transfer coefficient, h, can be described in terms of thermal conductivity, k_f, and specific heat, C_f, as $h \propto k_f^{0.6} C_f^{0.4}$ [79]. If the particles are made of PCMs, the effective specific heat of the PCM fluid will be increased by a factor of $1+\frac{\alpha \cdot H_{PCM}}{\Delta T \cdot C_f}$, where α is the weight fraction of the PCM particles in the fluid, HPCM is the latent heat of fusion of the PCM per unit mass, and ΔT is the temperature difference between the heat transfer surface and the bulk fluid. For example, a 5% mass fraction of hexadecane (melting point, 291 K) may enhance the effective heat capacity of FC-72 by up to 100% at ΔT=10 K, according to our preliminary calculation. Therefore, the use of PCMs as the dispersed particles will be able to boost the thermal properties of

thermal fluids much more significantly than non-PCM particles at the same volume fraction.

Current PCMs available for thermal fluid application can be divided into two main categories: solid-liquid transition and liquid-vapor transition. The thermophysical properties of state-of-the-art PCMs with potential use in thermal fluids are listed in Table 1.2. Liquid-vapor phase change materials, such as ethanol and water, have a much larger latent heat, but a condenser is needed for condensation of vapor. Solid-liquid phase change materials have small volume change during phase transition, and therefore the suspension of solid-liquid phase change particles can be used in the thermal management system designed for single phase fluids.

Table1.2: PCMs with potential use in thermal fluids. [80, 81]

Category	Compound Name	Phase Change Point (oC)	Thermal Conductivity (W/mK)	Latent Heat (J/g)
Solid-Liquid	Water	0	0.6 (liquid)	334
	Myristic Acid + Capric	24	0.15 (liquid)	147
	CaCl2.6H2O	29	0.56 (liquid)	192
	Na2SO4.10H2O	32	0.54 (liquid)	251
	Paraffin C17	22	0.15 (liquid)	215
	Paraffin C18	28	0.15 (liquid)	245
	Paraffin C19	32	0.15 (liquid)	222
	Capric Acid	32	0.15 (liquid)	152
	Zn(NO3)2.6H2O	36	0.47 (liquid)	147
	Indium	157	82 (solid)	29
Liquid-Vapor	FC-72	56	0.06(liquid)	88
	ethanol	78	0.2 (liquid)	855
	water	100	0.6 (liquid)	2260

Nanoemulsion fluids are now developed to overcome barriers of state-of-the-art heat transfer fluids via adding liquid nanodroplets inside to elevate the heat transfer capability of conventional heat transfer fluids [9, 10, 13, 15]. In which nano elements made of phase change materials (PCMs) are introduced to increase the effective heat capacity of the base fluid. The added liquid forms liquid nanodroplets (typically measure less than 100 nm in length) by self-assembly without the need of external shear induced rupturing and are thermodynamically stable. This innovative system is designed to have superior thermophysical properties, and especially, higher heat transfer capability with higher heat dissipation limit and wider operation temperature range. Nanoemulsion fluids are also expected to bring forth a novel solution to the alarmingly increased heat dissipation demands with high adaptability in multi-scale cooling devices.

Here, based on most widely used applications, the following PCM heat transfer fluids are chosen as the candidate for the base fluids for nanoemulsion heat transfer fluids development:

1. PAO are hydrocarbons of paraffinic and iso-paraffinic type (including mineral oils) used in a variety of direct cooling of electronics parts as well as in cooling transformers. Many petroleum based aliphatic compounds meet the Food and Drug Administration (FDA) and United States Department of Agriculture (USDA) criteria for incidental food contact. These petroleum-based fluids do not form hazardous degradation byproducts. Most of these fluids have a non-discernible odor and are nontoxic in case of contact with skin or ingestion. PAO-based fluids have

replaced the silicate-ester fluids in a variety of military electronics (and avionics) and cooling applications in the last decade.

2. Fluorocarbons are Fluorinated compounds such as perfluorocarbons (i.e., FC-72, FC-77) hydrofluoroethers (HFE) and perfluorocarbon ethers (PFE) have certain unique properties and can be used in contact with the electronics. These fluids are non-combustible and non-toxic.

Chapter 2: Fundamentals of the nanoemulsion fluids

Definition of nanoemulsion fluids\

One fluid is dispersed into another immiscible fluid as self-assembled nanodroplets to create a "nanoemulsion fluid", which differs fundamentally in boiling from bulk fluids and conventional emulsion [9, 10]. Those nanodroplets are reverse micelles swollen with added fluid and stabilized by the surfactant molecules. Nanoemulsion fluids are part of a broad class of multiphase colloidal dispersions. Some nanoemulsion fluids can be spontaneously generated by self-assembly without the need of external shear and are suited for thermal management applications [82-93]. Table 2.2 is the comparison between self-assembled nanoemulsion fluids and conventional emulsions.

Table 2.2: Comparison of nanoemulsion fluids and emulsions

No	*Property*	*Nanoemulsion fluids*	*Emulsion*
1	Appearance	Transparent	Turbid
2	Interfacial tension	Ultra low (usually <<1 mN/m)	low
3	Droplet size	<50 nm	>500nm
4	Stability	Thermodynamically stable, long shelf-life	Thermodynamically unstable
5	Preparation	Self-assembly	Need of external shear
6	Viscosity	Newtonian	Non-Newtonian

It is clear from Table 2.2 that the nanoemulsion fluids outshine the emulsion in multi aspects which makes them a good candidate for heat transfer applications.

Surfactants

Introduction

Surfactant is a generic term for a surface-active agent, which literally means active at a surface and is used here to help the formation of nanoemulsion fluids. It is fundamentally characterized by its tendency to adsorb at surfaces and interfaces when added in low concentrations to an aqueous system. Surfactants have a unique long-chain molecular structure that is composed of a hydrophilic head and a hydrophobic tail as illustrated in Fig. 2.1. They have a natural tendency to adsorb at the liquid-vapor interface with their polar head oriented towards the aqueous solution and the hydrocarbon tail directed towards the vapor. Based on the nature of the hydrophilic part of the molecule, which is ionizable, polar, and polarizable, surfactants are generally categorized as anionics, nonionics, cationics, and zwitterzionics[92].

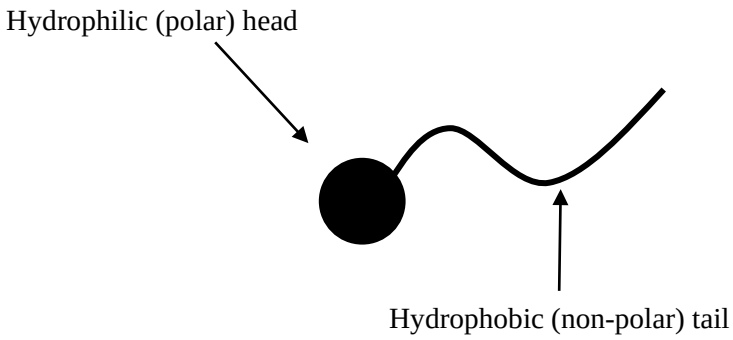

Fig. 2.1 Schematic illustration of the structure of a surfactant molecule

Surface tension and micelles

Surfactant additives in aqueous solutions naturally tend to diffuse towards the vapor-liquid interface and subsequently get adsorbed on it. Depending upon their chemistry (ionic and molecular structure) and orientation at the interface, some desorption may also occur. The primary effect of the surfactant adsorption-desorption process at the vapor-liquid interface is to reduce the surface tension of the solution. This entire process is time-dependent and it manifests in a dynamic surface tension behavior at an evolving vapor-liquid interface (as in ebullience), which eventually reduces to an equilibrium value after a long time span.

Surface tension reduction of an aqueous solution decreases continually with increasing concentrations till the critical micelle concentration (CMC) is reached, at which point the surfactant molecules cluster together to form micelles. All surfactants in their solutions show significant changes in adsorption behavior at or around their respective CMC. The CMC is characterized by micelle formation, or micellization, which is the property of surface-active solutes that leads to the formation of colloid-sized clusters at particular concentration; additives form aggregates in the bulk phase or a surfactant cluster in solution that are termed micelles. Different shapes and sizes of micelles exist depending upon the surfactant type and its packing, concentration, solution temperature, pressure of other ions, water-soluble organic compounds in the solution, and typical micelles are shown in Fig. 2.2. However, the micelle is a dynamic entity and its structure and shape can change with time. Further aggregation

above a certain temperature, referred to as the cloud point, leads to the separation of the liquid phase that gives the solution a turbid appearance.

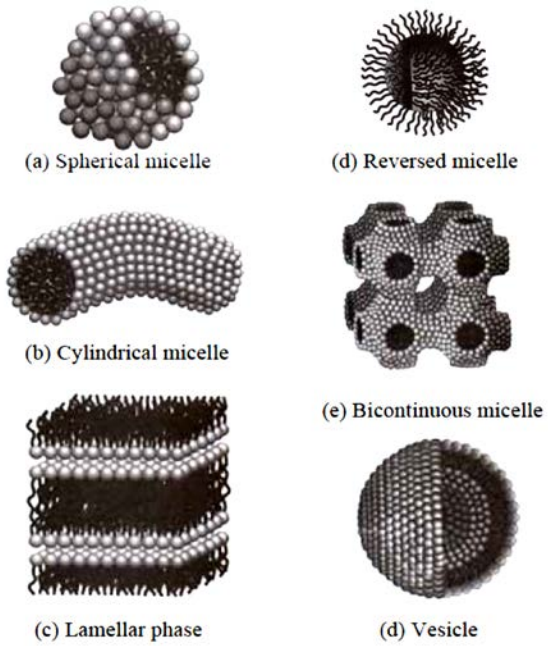

Figure 2.2 Different structures inside micelle systems[92]

Formation of nanoemulsion fluids

Self-assembled nanoemulsion fluids are thermodynamically stable, and the formation of these fluids can be explained using thermodynamic theory [84-88, 91, 93-95]. The nanoemulsion fluid consists of one oil phase, one water phase, and certain surfactants. The adding of surfactant lowers the surface tension of the oil–water interface, and the change in entropy of the system is given by Equation 2.1,

$$DG_f = \sigma DA - T \cdot DS \qquad (2.1)$$

where DG_f is the free energy of formation, σ is the surface tension of the oil–water interface, DA is the change in interfacial area on nanoemulsification, DS is the

change in entropy of the system which is effectively the dispersion entropy, and T is the temperature. The change in DA is very large due to the large number of nanosized droplets in the nanoemulsion fluids. However, the interfacial tension γ is very small (usually <<1 mN/m), and therefore the increase in the surface energy, γ DA could be small. On the other hand, the entropy arising from the mixing could be very large. The favorable entropic contributions also arise from dynamic processes such as surfactant diffusion in the interfacial layer and monomer-micelle surfactant exchange. So, the entropy of mixing can be large enough to compensate for the positive interfacial free energy and to give the nanoemulsion system a free energy lower than that of the unmixed components. Self-assembled nanoemulsion fluids can be formed via self-assembly, and are in fact thermodynamically stable.

Nucleate Boiling Basics

Thermal management solutions

Figure 2.3 provides a graphical representation of the variation of required temperature difference with surface heat flux for a variety heat transfer conditions and cooling fluids. The figure suggests that for a maximum available temperature difference of 40K, natural convection and forced convection air cooling are only effective for removing heat fluxes up to approximately 0.5kW/m^2 and 2.5kW/m^2, respectively. Despite this fact, air cooling dominated microprocessor thermal management schemes in the 1990s, but only through the aggressive exploitation of high density extended surfaces and various heat spreading and air handling techniques.

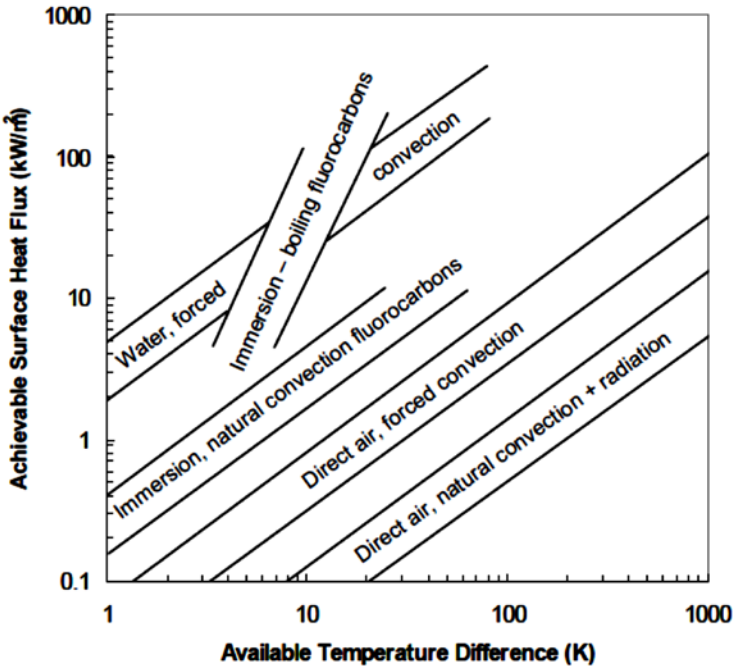

Figure 2.3 Variation of achievable surface heat flux with available temperature difference for various heat transfer modes ad fluids [96]

Boiling Heat Transfer

The definition of the heat transfer coefficient $h = q/\Delta T$ may be rearranged to explicitly state the relationship between temperature difference and heat flux shown in Figure 2.4.

Thus, the steep slope of the boiling band in Figure 2.4 indicates heat transfer coefficients significantly higher than those typically achievable with single phase convective cooling. Even though boiling heat transfer can provide for the removal of a large range of heat fluxes over a small temperature range, there are limits to its applicability and effectiveness which must be considered in the design of passive,

immersion cooled systems. The boiling curve of Fig.2.4, discussed in detail in the following subsections, shows the relationship between heat flux and superheated surfaces that is typically observed in heat flux controlled heat transfer from a surface immersed in an, otherwise, quiescent pool of liquid.

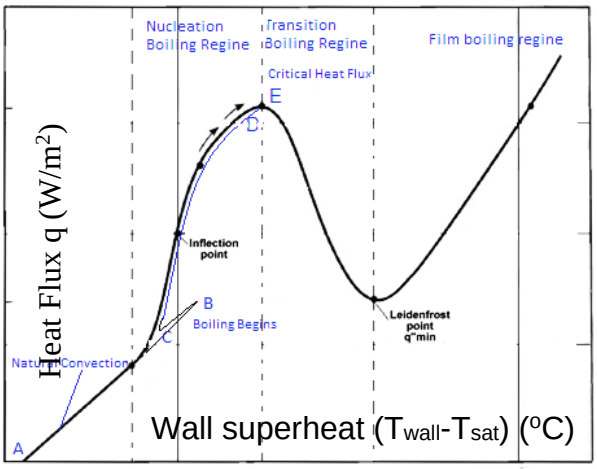

Figure 2.4 Typical pool boiling curve

Single Phase Natural Convection and the onset of nucleate boiling

The portion of curve between points A and B in figure 2.4 represents single convection. Characterized by the relatively low q" vs ΔT slope. Point B represents the onset of nucleate boiling where the surface temperature is high enough to begin bubble nucleation. Once one bubble is generated, it may trigger other nucleation sites, and many more bubbles immediately follow. When this happens, the surface cools very quickly, and its temperature drops very rapidly to point C.

Once nucleate boiling has been established where bubbles are generated at and emanate from distinct nucleation sites on the surface. Boiling may be sustained below

point C until the boiling heat transfer rate approaches the single phase convection rate, and the last nucleation sites that make this possible. Rough surfaces with nucleation sites that require little superheat to create a bubble embryo, or those that already contain a minute pocket of trapped gas that can serve as a bubble as a bubble embryo, may show little or no difference between the increasing and decreasing heat flux curves. In general, the required temperature difference between points B and C required to initiate nucleation is highly statistical in nature but may as high as 30ºC for high wetting liquids and highly polished surfaces.

Fully developed nucleate boiling

The portion of the curve between point C and D in Fig 2.4 represents the nucleate boiling regime. The steep slope in this region illustrates the high heat transfer coefficients associated with nucleate boiling. Significant increases in heat flux maybe obtained with very modest increases in temperature. This steep slope is why the nucleate boiling regime is of prime interest in electrics cooling applications.

Despite its highly non-linear temperature dependence, nucleate boiling often correlated as a linear function of superheat via a temperature dependent boiling heat transfer coefficient

$$Q_b = h_b A_{surface}(T_{surface} - T_{sat}) \qquad (2.2)$$

Recognizing the heat transfer contribution of bubbles agitating the liquid and drafting hot liquid away from a boiling surface. Rohsenow defined a bubble Reynolds number and bubble Nusselt number and developed a correlation for saturated nucleate pool boiling that may be expressed in the form

$$h_b = \mu_f h_{fg} \sqrt{\frac{g(\rho_f - \rho_g)}{\sigma}} \left(\frac{c_p}{h_{fg} Pr^s C_{sf}} \right)^{\frac{1}{r}} (T_w - T_{sat})^{\frac{1}{r}-1}) \qquad (2.3)$$

With fluid properties evaluated at the saturation temperature. The constant C_{sf} has been interpreted as reflecting the influence of cavity size distribution on bubble generation for a given fluid/surface combination, and includes the effect of contact angle. It is also assumed to be independent of pressure and is not included in the Rohsenhow correlation due to a lack of data. For the experimental data on which the equation was based, s was found to range from 0.8 to 2.0 but was centered on a value of 1.7 for "clean" surfaces. The parameter r may fall between 1/5 and ½ but is often taken to equal a value of 1/3, following the Rohsenow derivation. In practice, all three parameters may be determined empirically to best fit the data. While the literature contains many studies about evaluating the boiling equation for a wide variety of fluids and surfaces, no unifying or predictive trends for these constants have been identified as of yet. Note that s and C_{sf} appear only once in the equation and they appear together with s as the exponent of Prandtl number with C_{sf} multiplying it. However, while the Prandtl number may be expected to vary with pressure, C_{sf} is assumed to be independent of pressure. In the absence of data spanning a range of pressures, a value of s=1.7 may be assumed.

Critical heat flux

As the nucleate boiling process continues to higher and higher heat fluxes and approaches point E in Fig. 2.4, an increasing amount of vapor is being generated, and it becomes difficult for fresh liquid to reach the surface. Point E represents the critical heat flux, where the large volume of generated vapor presents fresh liquid from

replenishing the supply at the surface. As a result, the surface becomes blanked by a thin layer of vapor and increases greatly in temperature (point D to E). The region of the curve that passes point E represents the film boiling regime, where the dominant modes of heat transfer are conduction and radiation across the vapor blanket. If the surface temperatures drop below Leindenfrost point, the vapor blanket becomes unstable, breaks up and the liquid is allowed to come in contact with the surface to reinitiate the nucleate boiling process (point h).

As the temperature excursion from points E in Fig. 2.4 can be on the order of 100^{o}C or more, electronics cooling applications are most often restricted to the single phase and nucleate boiling regimes, with CHF as an absolute upper limit. Therefore, in order to take advantage of the high heat transfer coefficients associated with nucleate boiling, it is necessary to stay below the CHF limit of a given system to prevent catastrophic failure. The well-known Kutateladze-Zuber CHF relation was developed for saturated pool boiling on large, thick, upward-facing horizontal plates.[97]

$$q''_{CHF} = \frac{\pi}{24} h_{fg} \sqrt{\rho_g} [\sigma_f g(\rho_f - \rho_g)]^{1/4}) \qquad (2.4)$$

The Zuber analytical treatment considered the Taylor instability criterion for coalesced bubble vapor columns and defined CHF as occurring when the liquid-bubble interface becomes unstable. More recent research has suggested that, for horizontal heaters, lateral bubble coalescence creates dry patches on the surface that eventually reach the Leidenfrost temperature and cause CHF. Mudawar derived an interfacial lift-off model for CHF on vertical surfaces based on an analysis of Kelvin-Helmholtz waves. Their resulting equation is identical in form to Eq 2.4, despite

being based on a different mechanism. Regardless of its derivation, equation 2.4 remains relatively accurate and in particular, captures the effect of pressure on CHF.

Spontaneous nucleation

Spontaneous nucleation refers to the formation of vapor nuclei in a superheated liquid independent of nucleation sites on a solid surface. There are two approaches used to predict the degree of superheat necessary to cause spontaneous nucleation. One approach is based on the mechanical stability of a fluid defined by an appropriate equation of state. The other approach considers the microscopic density fluctuations present in fluids, predicted by statistical mechanics.

Spontaneous nucleation generally does not occur in engineering practice because boiling will occur at nucleation sites on a heated solid surface well before the liquid becomes sufficiently superheated to cause spontaneous nucleation. The conditions necessary for spontaneous nucleation are discussed in the following sections. Experimental results are generally in good agreement with the theoretical prediction of the limits of superheat.

Thermodynamic limit of superheat can be predicted for a Van der Waals fluid. In Fig 2.5, curve ABCDEF represents an isotherm for a Van der Waals fluid with temperatures less than the critical temperature. The curve ABEF represents an isotherm as is commonly taught in engineering thermodynamics, where the straight BE represents a saturated mixture.

Consider the behavior of a Van der Waals fluid as it is slowly expanded isothermally from a compressed liquid state. The fluid will proceed along the curve shown in Fig 2.5 to state B, where it is saturated liquid. If the liquid expands further, the expected behavior is for nucleation sites to become active on the walls of the vessel containing the fluild. The fluid will then become a saturated mixture and follow the line BE. If no nucleation sites are present, however, the liquid will instead continue along the Van der Waals curve towards state C, entering the meta-stable liquid state. This process can continue only up to state C. It is impossible for a Van der Waals fluid to exist in stable equilibrium between state C and D because dP/dV>0. State C therefore represents the thermodynamics limit of superheat.

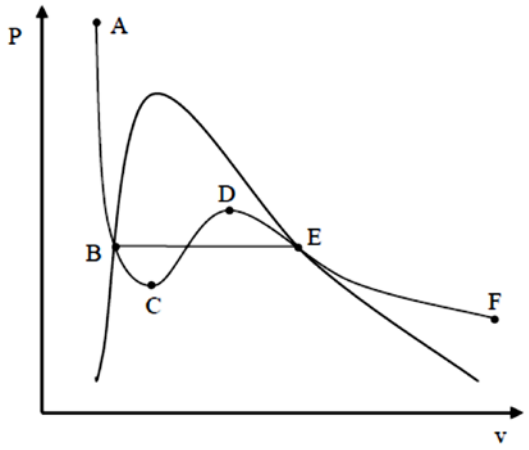

Fig. 2.5 Isotherm curve of the liquid

This approach is not limited to Van der Waals fluids: any fluid that exhibits a “Van der Waals loop” will have a meta-stable liquid state with an upper bound where the slope of the P-v curve crosses through zero. In fact, for most fluids the thermodynamic limit of superheat predicted using the Van der Waals equation of state is a bit too low when compared to experimental results. Other equations of state give

more accurate results, although, there is some difficulty in accurately modeling the state of meta-stable fluids using data from the stable liquid and vapor regions. The kinetic limit of superheat is found by considering the density fluctuations that occur in all fluids. In liquids, these density fluctuations take the form of microscopic vapor bubbles.

Nucleate boiling is suppressed in a number of ways, including, using glass capillary tubes, pulsed heating, and the floating droplet method. A drawn and annealed glass capillary tube has an exceptionally smooth surface that contains few, if any, nucleation sites. Large degrees of superheat were first studied using this method. In the pulsed heating method an electrical heating elements (such as a fine wire or a film heater) is immersed in the liquid under study. A pulse of electrical current applied to the heater causes the surface temperature to rise rapidly at a rate of 107 c/s or more. Both nucleate boiling and spontaneous nucleation occur on the heater surface in the first several tens of microseconds, but the time scale is so short that the nucleate boiling does not dominate and spontaneous nucleation may be observed. This temperature allows observation of higher nucleation rates than other methods, although the short time scales involved make observation and measurement of the phenomenon challenging. The final technique, the floating droplet method uses conditions most similar to those found in dilute emulsions.

One of the first uses of the floating droplet method was by Moore. Moore created droplets of Freon-12 in water in a heated test chamber held at high pressure, and then

superheated them by slowly reducing the pressure in the chamber while holding temperature constant.

Nucleate Boiling inside Nanoemulsion Heat transfer fluids

Brief Introduction

As the nanoemulsion heat transfer fluids a complex colloid system which includes multi components and internal exchange processes. It makes the study of nucleate boiling processes inside these fluids even more difficult. So based on others' previous work on different colloid systems, we have summarized the following possible mechanism inside the nanoemulsion fluids during nucleate boiling.

Surface Wetting Effects on Nucleate Boiling

Surface wettability is very important in nucleate boiling process. It generally refers to the manifestation of the molecular interactions between liquids and solids in direct contact at the interface, and is generally reflected in the contact angles. In multiphase heat transfer, the nature and dynamics of surface liquid-solid contact often plays a dominant role.

The liquid-solid system can be either completely wetting, or have different degrees of wetting, or be complete non-wetting as schematically illustrated in Fig 2.6. Knowledge of the intermolecular interactions, both within the liquids, and across the liquid-vapor and liquid-solid interfaces, is an important part of charactering surface wettability or contact angle. When a drop of liquid is placed on solid substance, it

may spread so as to increase the liquid-solid and liquid-gas interfacial areas. Simultaneously, the solid-gas interfacial area decreases and the contact angle theta between the drop and solid is reduced. The value of theta can be seen as a measure of the balance between the tendency of the drop to spread so as to cover the solid surface and to contract in order to minimize its own surface area.

The degree of spreading is governed by the surface tension of the liquid σ_{LG}, the surface tension of the solid σ_{SG}, and the interfacial tension of the liquid and the solid σ_{SL}. These forces essentially represent the liquid-gas, solid-gas, and solid-liquid interfacial tensions; and their interactions are depicted in Fig. 2.6.

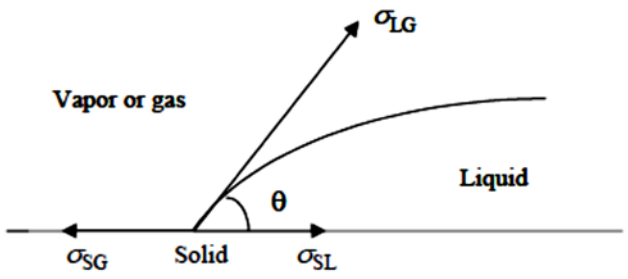

Fig. 2.6 Liquid-Vapor Surface Tension Diagram

The surface free energy of the solid σ_{SG} tends to spread the drop, i.e., to shift the three phase point forward or along the surface. Thus, spreading is generally favored on high energy surfaces. The interfacial tension σ_{SL} and the horizontal component of the surface tension force $\sigma_{LG}cos\theta$ act in the opposite direction. At equilibrium state, the resultant force is thus zero and this expression is very well known as Young's

equation and has become the basis for understanding the phenomenon of contact angle or surface wetting on solid surfaces.

The phenomenological modeling of mechanisms for heat and fluid transport in nucleate boiling is still not completely developed, and is the subject of much study. One reason for this is the complexity of interfacial contact at the surface, which is affected by intermolecular forces. Given that the primary heat transfer is by evaporation and its efficiency is directly related to nucleation site density and bubble dynamics, surface wetting becomes an important predictor. To characterize the inter-relationship, insights are often obtained from a visual observation of the ebullience.

As a critical determinant of nucleate boiling, active nucleation site density is found to be a function of wettability and heat flux, and it directly accounts for the energy transfer by ebullience at the heater surface [98-101] have systematically studied the effect of pure liquid wettability on the active nucleation site density and onset of nucleate boiling (ONB) in pool boiling. They have correlated their data for active site density as a function of the wall superheat and contact angle, and pointed out that the fraction of the nucleated cavities decreases as the wettability of the surface increases. The wettability of the surface in their collective work was changed by controlling the degree of oxidation of the heater surface.

Nucleate Pool Boiling with Surfactants

Another interesting effect of surfactant is that small amounts of surfactant additives in water tend to change and enhance the boiling heat transfer in water by essentially modifying nucleation and the concomitant bubble dynamics. The importance of surfactant-enhanced boiling heat transfer has been widely recognized, and many studies have investigated the pool boiling behavior in aqueous surfactant solutions under atmospheric conditions. A recent review of this body of work was provided [102].

Boiling with surfactant additives is a very complex process. Besides the effects of heater geometry, its surface characteristics and wall heat flux level, the bulk concentration of additive, surfactant chemistry (ionic nature and molecular weight), dynamic surface tension of the solution, surface wetting and nucleation cavity distribution, marangoni convection, surfactant adsorption and desorption, and foaming are some of the factors that appear to have a significant influence [103-106].

Also, the bubble dynamics (inception and gestation → growth → departure) has been found to be considerably altered with reduced departure diameters, increased frequencies, and decreased coalescence [104]. A direct correlation of the heat transfer with suitable descriptive parameters for all of these effects, however, remains elusive because of the complicated nature of the problem.

A variety of different predictive parameters and mechanisms have been proposed to describe the complex phase-change process, but much of the focus has been on the effect of reduced interfacial tension. Because of the highly dynamic nature of the nucleate boiling, typically in the range of 0-100 ms [107], the dynamic surface tension of the aqueous surfactant solution instead of the equilibrium surface tension has been proposed as a predicator of the nucleate boiling process [106]. Furthermore, the addition of a small amount of surfactant to water, not only changes the liquid-vapor interfacial behavior, but, more importantly, it also alters the solid-liquid interfacial characteristics. All the factors related to surface wettability thus get affected; including one of the most important ones in nucleate boiling - active nucleation density.

The wetting of aqueous surfactant solutions is further found to be influenced by the additive's chemical structure. The presence of the ethoxy or ethylene oxide (EO) group in its molecular-chain, in particular, increases the overall size of the polar head and makes the surfactant more hydrophilic[108]. This increases surface wettability due to the adsorption of surfactant molecules on the solid surface. The concomitant influence on the active nucleation site density and dynamic contact angle should therefore be taken into consideration in characterizing nucleate boiling of aqueous surfactant solutions.

Nucleate Pool Boiling with Polymers

Thermal processing of fluid media to produce biochemical, pharmaceutical, personal care, and hygiene products is a very complex heat transfer problem. For nucleation

inside aqueous solution with polymers, a variety of factors play a role, and they include the type of polymer, its molecular weight and concentration, solution rheology and interfacial properties (surface tension and wettability), heated surface geometry, and heat flux levels among others.

Several studies have investigated nucleate pool boiling characteristics of polymeric solutions under atmospheric conditions. In one of the earliest studies on the effects of polymer additives on boiling of water on a plate heater, they [109] found the heat transfer to be enhanced in HEC-H and PA-10 solutions. While both additives make the solution more viscous with a shear-thinning flow behavior, HECH has surface-active properties as well (i.e., it reduces surface tension of the solution appreciably) and a lower molecular weight (M = 2×105); for PA-10, M = 106. The combined effects of nucleation site density and solution concentration on boiling are reported. Appreciable enhancement was observed in aqueous HEC solution on a 600 grit roughened surface, whereas no apparent enhancement was observed for the same solution on a much smoother surface. The experimental data, however, indicate deterioration in boiling heat transfer for very dilute aqueous polymeric solutions when compared to that of pure water.

The changed boiling heat transfer in polymer solutions is also displayed in a markedly different bubbling behavior (shape and size of bubbles, their growth rate, foaming, and nucleation frequency, etc.) compared to that of pure water [110]. Bubbles of smaller sizes and regular shapes are released from the heater with higher

frequencies than seen in pure water, and they rise in a more orderly fashion. Adjacent bubbles tend to coalesce less due to the effects of normal stresses and longitudinal viscosity in thin films formed between them. They also suggest that the change in the wetting angle along with a reduction in surface tension for HEC-H solutions account for the observed decrease in bubble sizes. The changes in the interfacial characteristic are perhaps a direct consequence of the molecular adsorption dynamics of the additive.

Polymers are typically large molecules, macromolecules, or agglomerates of smaller chemical units called monomers, and are broadly classified as biological or nonbiological macromolecules. Their addition in water primarily increases the solution viscosity, which tends to increase with concentration as well as the molecular weight of the polymer, and often, display a shear-rate dependent shear-thinning rheology. With the exception of some surface-active polymers (or polymeric surfactants) such as hydroxyethyl cellulose (HEC) and polyethylene oxide (PEO), most polymeric solutions do not show any significant change in surface tension σ. The viscosity of the polymer solution, however, can influence σ measurements considerably, especially at higher viscosity and bubble frequency [105, 111].

The reduced surface tension in solution of surface-active agents is largely brought about by the molecular adsorption of the additives to the vapor-liquid interface. The time scales of this process vary from order of seconds to minutes depending upon the polymer chemistry and its concentration in solution, which is possibly due to the slow

processes of diffusion transport of polymer molecules to the interface and their subsequent reorientation [112]. This dynamic adsorption process, along with time scales of 10-100 ms for boiling bubble dynamics in water [107], thus results in a rather complex interfacial behavior that significantly alters the nucleate pool boiling in polymeric solutions

Scope of Study

As stated previously, developing and characterizing the heat transfer properties of these novel nanoemulsion heat transfer fluids is not only important in revolutionizing the heat transfer properties of conventional heat transfer fluids, but also in providing novel heat transfer approaches to meet the demanding ultra-high heat flux dissipation needs. The presence of phase-changeable nanodroplets inside base heat transfer fluids changes the thermophysical properties of the base fluids and especially, their phase change heat transfer capability. This, however, along with fluid rheology change and the complex nature of nucleate boiling, results in a complex two-phase problem, which is investigated in this dissertation. The primary scope of this study addressing the many facets of the problem is summarized in the following:

1. Development of nanoemulsion heat transfer fluids with greatly enhanced thermal properties including thermal conductivity and phase change heat transfer coefficient for high heat flux electronic cooling

2. Characterization of the inner structure of the prepared nanoemulsion heat transfer fluids using small angle neutron scattering technique

3. Thermal conductivity and Rheology measurement and characterization of the prepared nanoemulsion heat transfer fluids

4. Pool and flow boiling heat transfer study to help understand the unique phase change heat transfer characteristics inside these nanoemulsion fluids

5. Visualization and recording of nucleate pool boiling inside nanoemulsion heat transfer fluids in order to qualitatively study the nucleation process and ebullience

6. Numerical simulation and modeling of the thermal transport process of nanoemulsion heat transfer fluids

Chapter 3: Preparation and Characterization Methods for Nanoemulsion Fluids

Preparation of nanoemulsion fluids

There are mainly two approaches to prepare nanoemulsion fluids: the spontaneous emulsification method and the phase inversion method[93]. Figure 3.1 shows the typical phase behavior diagram of a ternary system that contains two immiscible so-called oil and water phases and an amphiphilic surfactant component. The term "water" refers to a polar phase while "oil" is used for an apolar organic phase. When a system has a composition that lies in the shaded areas, a nanoemulsion fluid, either oil-in-water or water-in-oil, can be formed via self-assembly[92, 113].

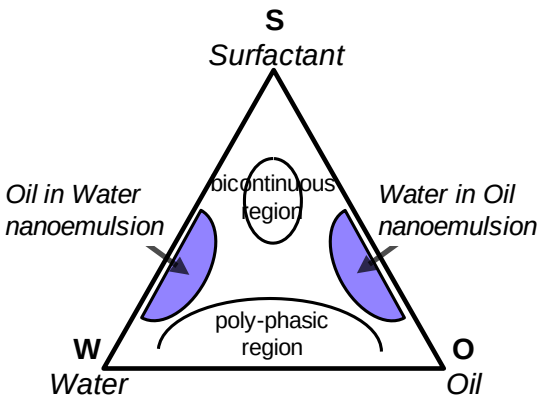

Fig. 3.1: Schematic phase diagram of a water-oil-surfactant ternary system. The shaded areas are regions where self-assembled nanoemulsion fluids are found.

Phase inversion of nanoemulsion fluids occurs upon addition of excesses of the dispersed phase or in response to temperature. This method makes use of changing

the spontaneous curvature of the surfactant layer. For non-ionic surfactants, this can be achieved by changing the temperature of the system, forcing a transition from an oil-in-water nanoemulsion at low temperatures to a water-in-oil nanoemulsion at higher temperatures (transitional phase inversion). During cooling, the system crosses a point of zero spontaneous curvature and minimal surface tension, promoting the formation of finely dispersed oil droplets.

Nanoemulsion fluids prepared

As a widely used heat transfer fluid with poor thermal properties, PAO based nanoemulsion fluids are mainly developed and investigated here. Meanwhile, another popular dielectric heat transfer fluids: Fluorocarbon based fluid mixture is also investigated here.

The nanoemulsion fluids developed are listed below:

Nanoemulsion fluids	***Sample group 1***	***Sample group 2***
	FC72/FC40 mixture*	
PAO based	Ethanol-in-PAO Nanoemulsion fluids	Water-in-PAO Nanoemulsion fluids

*: is not nanoemulsion fluids but listed here for summary

The two groups of PAO-based nanoemulsion samples all belong to the “Water”-in-“Oil” microemulsion where the PAO is used as the oil phase of the microemulsion system and one ionic surfactant is used as the surfactants to form stable “water-in-oil”

nanoemulsion system. The Fluorocarbon based fluids are FC72 simple mixture with FC40 fluid and they are miscible to each other.

The Figure 3.2 shows the picture of water-in-PAO nanoemulsion heat transfer fluids prepared:

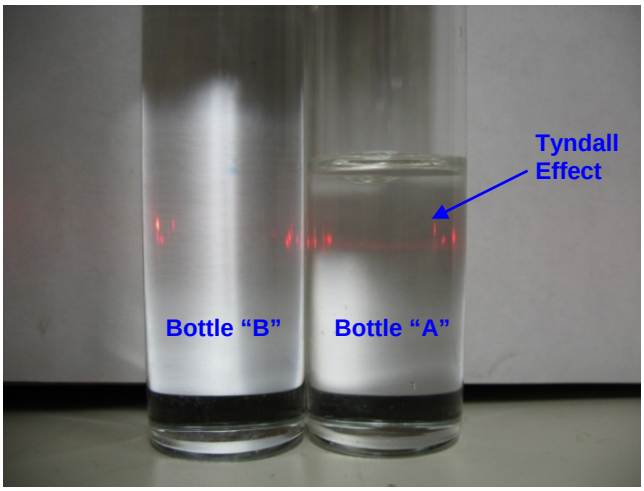

Fig. 3.2: Pictures of water/PAO nanoemulsion fluids (Bottle A) and pure PAO (Bottle B). Liquids in both bottles are transparent. The Tyndall effect (i.e. a light beam can be seen when viewed from the side) can be observed only in Bottle A when a laser beam is projected through Bottles A and B.

The Ethanol-in-PAO nanoemulsion is also shown here for comparison. It looks transparent and of no color too.

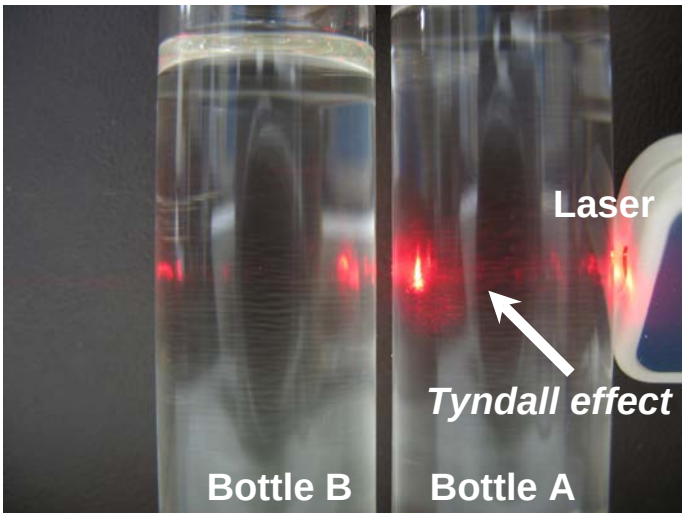

Figure 3.3 Pictures of Ethanol/PAO nanoemulsion fluids (Bottle A) and pure PAO (Bottle B). Liquids in both bottles are transparent. The Tyndall effect (i.e. a light beam can be seen when viewed from the side) can be observed only in Bottle A when a laser beam is projected through Bottles A and B.

Experimental Characterization Methods

Microstructure Characterization

The microstructure of nanoemulsion fluids can be affected by many factors, including different surfactant and concentration, dispersed liquid and concentration, molar ratio of dispersed liquid to surfactant, temperature, pH value, and salinity [95, 114-119]. The characterization of the micro structure of nanoemulsion fluids is a challenging task. In the past, small angle X-ray scattering (SAXS), small angle neutron scattering (SANS), dynamic or laser light scattering (DLS), transmission electron microscopy (TEM), and nuclear magnetic resonance (NMR) have been used for the structure

characterization. In addition, the measurement of nanoemulsion properties, such as viscosity, electric conductance, thermal conductivity, dielectric permittivity, electrophoretic birefringence, ultrasonic interferometry, and ultrasonic absorption can also provide information on the internal microstructure.[82, 114, 120-125]

Small-angle scattering methods

Small-angle X-ray scattering (SAXS) and small-angle neutron scattering (SANS) are the two complementary techniques known jointly as small-angle scattering (SAS). SAS patterns are collected at very small angles (a few degrees) and are capable of delivering structural information in the resolution range between 1 and 25 nm, and of repeat distances in partially ordered systems of up to 150 nm in size. The conceptual experiment and theory is the same for X-rays and neutrons, the differences are the physics of the X-ray (electro-magnetic radiation) versus neutron (neutral particle) interactions with matter. X-rays is sensitive to electron density while Neutrons have zero charge and negligible electric dipole which can therefore travel long distances in material without being scattered or absorbed. In addition, SANS uses the deuteration method to enhance its contrast, indicating that SANS can measure either naturally occurring contrasts or artificial contrasts introduced through deuteration. One shortcoming of SANS is the intrinsically low flux of neutron sources compared to the orders of magnitude of higher fluxes for X-ray sources.

SAS includes the four basic steps used in all scattering techniques: monochromation, collimation, scattering and detection. SAS data analysis can be performed at many levels. The initial level consists of a “follow the trends” type of approach using

standard plot methods. The next level uses nonlinear least squares fits to obtain realistic models. The final trend makes use of the sophisticated shape of reconstruction methods in order to obtain insight into the structure and morphology within the investigated sample. The detailed data reduction and fitting procedure is in Appendix.

Dynamic light scattering method

Dynamic light scattering (DLS) is another technique used to determine the size distribution profile of small particles in suspensions or polymers in solutions. [116, 126-131] Dynamic light scattering (DLS) provides a way to measure the velocity autocorrelation function and the relaxation time. The motions of the particles in fluids cause the intensity of scattering light to fluctuate with time due to the interference effects from neighboring particles, much like a fluctuating diffraction grating. The normalized temporal autocorrelation $g^2(q;\tau)$ of the scattered light intensity I is given by:

$$g^2(q;\tau) = \frac{\langle I(t)I(t+\tau)\rangle}{\langle I(t)\rangle^2} \qquad (3.1)$$

where $g^2(q;\tau)$ is the autocorrelation function at a particular wave vector, q, and delay time, τ, and I is the intensity. The particle size can be determined from the curve fitting of $g^2(q;\tau)$. Unlike the SANS, the DLS only applies to the "dilute" colloidal suspensions (often <<1 vol%).

Transmission electron microscopy method

Transmission electron microscopy (TEM) is a very important technique for the study of microstructures because it can directly produces images at high resolution and it can capture the microstructural transition [114, 132-134]. However, the direct application of TEM to nanoemulsion fluids is often prohibited because (1) the high vapor pressure of nanoemulsion fluids makes them incompatible with the low pressures (< 1-5 torr) in TEM; (2) chemical reactions and the consequent change in nanoemulsion systems could be induced by the electron beam in TEM; and (3) the based fluid and the dispersed phase often give insufficient contrast in TEM images. Two special TEM techniques are developed for fluid samples: (1) the cryo-TEM analyses in which samples are directly visualized after fast-freezing and freeze-fracture in the cold microscope[132, 135] and (2) the Freeze-Fracture TEM technique in which a replica of the specimen is imaged under room temperature conditions. [133, 134, 136-139]

Thermophysical properties characterization methods

Thermal conductivity

Low thermal conductivity is a primary limitation in the development of energy-efficient heat transfer fluids that are required in many industrial applications. Conventional heat transfer fluids have relatively poor thermal conductivity compared to metals. [140]. It has been reported that the dispersed liquid nanodroplets could alter thermal conductivity of the base fluids. However, because of the absence of a theory for the thermal conductivity of nanoemulsion heat transfer fluids, an

investigation of the effect of nanodroplets on the thermal conductivity will be conducted.

Nanofluids, i.e., colloidal suspensions of solid nanoparticles, and more recently, nanoemulsion fluids have attracted much attention because of their potential to surpass the performance of conventional heat transfer fluids [1-22]. The coolants, lubricants, oils, and other heat transfer fluids used in today's thermal systems typically have inherently poor heat transfer properties which have come to be reckoned as the most limiting technical challenges faced by a multitude of diverse industry and military groups. A number of studies have been conducted to investigate thermal properties of nanofluids with various nanoparticles and base fluids. However, the scientific community has not yet come to an agreement on the fundamental effects of nanoparticles on thermal conductivity of the base fluids. For example, many groups have reported strong thermal conductivity enhancement beyond that predicted by Maxwell's model in nanofluids [1,2,23,24]. Consequently, several hypotheses were proposed to explain those unexpected experimental results, including particle Brownian motion, particle clustering, ordered liquid layer, and dual-phase lagging [18,21,25-28]. Recently, however, an International Nanofluid Property Benchmark Exercise reported that no such anomalous enhancement was observed in nanofluids [22].

In this study, nanoemulsion fluids are employed to investigate the effects of nanodroplets on the fluid thermal conductivity. These fluids are spontaneously generated by self-assembly while the droplet size inside is within nanoscale.

There are two widely used methods to measure the thermal conductivity of nanoemulsion fluids which includes: 1. the transient hot-wire technique and 2. 3ω-wire method [1, 2, 4, 8, 10, 13, 24, 28, 39, 52, 141-144]. In the transient hot-wire method, thermal conductivity value is determined from the heating power and the slope of temperature change versus logarithmic time. The 3ω-wire method is actually a combination of the 3ω method and the hot-wire method. Similar to the hot-wire method, a metal wire suspended in a liquid acts as both heater and thermometer. A sinusoidal current frequency is passed through the metal wire and generates a heat wave at frequency 2ω. The temperature rise at frequency 2ω in the metal wire can be deduced by the voltage component at frequency 3ω. The thermal conductivity of the liquid, *k*, is determined by the slope of the 2ω temperature rise of the metal wire with respect to the frequency ω,

$$k = \frac{p}{4\pi l}\left(\frac{\partial T_{2\omega}}{\partial \ln \omega}\right)^{-1} \qquad (3.2)$$

where p is the applied electric power, ω is the frequency of the applied electric current, l is the length of the metal wire, and $T_{2\omega}$ is the amplitude of temperature oscillation at frequency 2ω in the metal wire. One advantage of this 3ω-wire method is that the temperature oscillation can be kept small enough (below 1 K, compared to about 5 K for the hot-wire method) within the test liquid to retain constant liquid properties. Calibration experiments were performed for hydrocarbon (oil), fluorocarbon, and water at atmospheric pressure. The literature values were reproduced with an error of <1% as shown below in Figure 3.4.

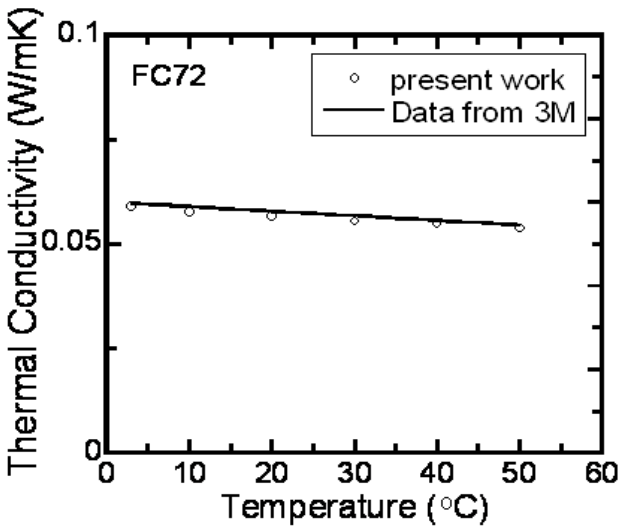

Fig. 3.4**:** Calibration of $3\omega - wire$ method using FC72 and compared with literature value

Viscosity

Viscosity is a measure of the resistance of a fluid which is being deformed by either shear stress or tensile stress. Viscosity is another macroscopically observable parameters that characterize a nanoemulsion fluid, and it may range anywhere between a low viscous fluid and a gel state. [10, 90, 143, 145] It is an important quantity for many practical applications of nanoemulsion fluids especially those used for hydraulic fluids. For instance, pumping such systems might be of interest in their application, and here viscosity plays an important role. Viscosity can be determined form the equation below:

Viscosity is defined by considering the force applied in the course of flow of a fluid, and its dissipation per unit area and velocity gradient is the viscosity

$$F = \mu A \frac{u}{y} \qquad (3.3)$$

where F is the stress force, u is the velocity, A is the area and μ is the proportionality factor called dynamic viscosity. The kinematic viscosity ν is related to the dynamic viscosity by dividing by the density ρ of the fluid, $\nu = \frac{\mu}{\rho}$.

Viscosity of a nanoemulsion fluid depends largely on its microstructure, i.e., the type of aggregates that are present, on their interactions, and on the concentration of the system. So the viscosity can be used to monitor structural changes in the nanoemulsion system. In order to do so, one has to compare the experimental data to theoretical expressions that give the viscosity expected for certain model systems.

The general behavior is that whenever a second phase is dispersed in a solvent this should lead to an increase in the bulk viscosity which was discovered by Einstein, who derived a formula that describes the increase in viscosity as a function of the volume fraction of dispersed material for the case of compact spherical particles that have a sticky surface (no-slip condition).

$$\mu_r = 1 + 2.5\phi \qquad (3.4)$$

where μ_r is the relative viscosity, and ϕ is the volumetric fraction of encapsulated water nanodroplets. Equation 3.4 is valid for hard spheres, but it is modified for the case of a dispersion of liquid spheres in another liquid medium.

Viscosity measurements were carried out using a rotating cylinder rheometer (Brookfield DV-I Prime) that provides a continuous sensing capability for rapid viscosity measurement, and simultaneous viscosity and temperature measurement.

Boiling heat transfer characterization methods

Pool Boiling

The pool boiling heat transfer properties are investigated using standard pool boiling test set-up with a thin platinum wire heater immersed inside test fluid. The control system and are shown in Figure 3.6 where the basic experiment follows the Nukiyama wire heating method[146]. A glass tank (($L \times W \times H$) $7.8cm \times 3cm \times 5.2cm$) is used to hold the test samples and the tank is put inside one large water bath to maintain the test fluid at constant temperature. A platinum wire 25μm in diameter and 3cm long suspended is used as both the heater and the thermometer which is connected via four wire method.

Four-terminal sensing is also known as Kelvin sensing, after William Thomson, Lord Kelvin, who invented the Kelvin Bridge in 1861 to measure very low resistances. Each two-wire connection can be called a Kelvin connection. A pair of contacts that is designed to connect a force-and-sense pair to a single terminal or lead simultaneously is called a Kelvin contact.

When a Kelvin connection is used, current is supplied via a pair of force connections (current leads). These generate a voltage drop across the impedance to be measured

according to Ohm's law V=RI. This current also generates a voltage drop across the force wires themselves. To avoid including that in the measurement, a pair of sense connections (voltage leads) are made immediately adjacent to the target impedance (shown as connection 2 and 3 in Fig. 3.5). The accuracy of the technique comes from the fact that almost no current flows in the sense wires, so the voltages drop V=RI is extremely low.

It is conventional to arrange the sense wires as the inside pair, while the current wires are the outside pair. If the current and voltage sense connections are exchanged, accuracy can be affected because more of the lead resistance is included in the measurement. In some arrangements, the force wires are very large compared to the sense wires which can be very small. If the force and sense wires are exchanged at the instrument end, the sense wire could burn up from carrying the force current. The technique is commonly used in low-voltage power supplies, where it is called remote sensing, to measure the voltage delivered to the load independent of the voltage drop in the supply wires. It is also common to provide 4-wire connections to low-value, high-power resistors. They are often known as "current-sensing shunts" rather than simple resistors in this case.

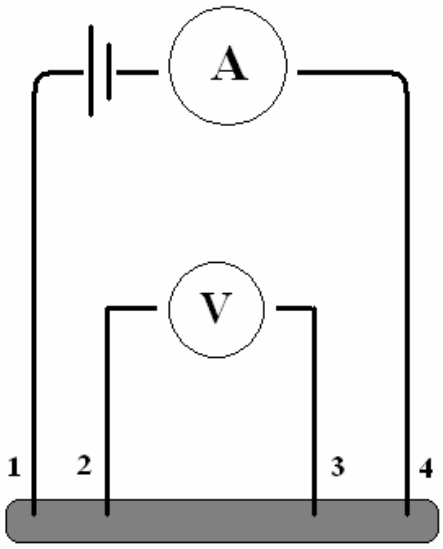

Fig. 3.5: 4-Wire method.

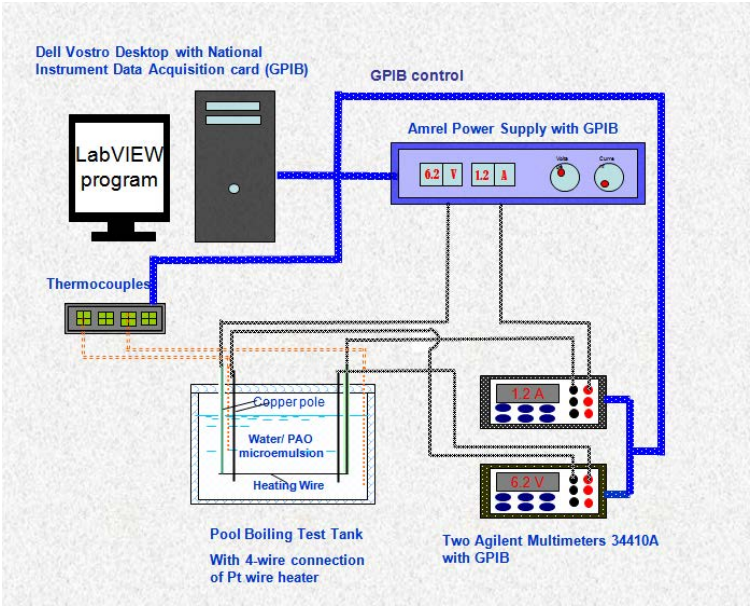

Fig. 3.6: Pool boiling apparatus scheme for pool boiling test

Flow Boiling

The flow boiling heat transfer experiments were also conducted on a platinum wire 25μm in diameter and 3cm long suspended inside an aluminum channel (inner

channel dimension($L \times W \times H$ 7cm*2.7cm*1cm) as shown in Figure 3.7. This platinum wire serves as both the heater and the thermometer. The interface angle of the wire with flow can be adjusted among 0^o, 45^o and 90^o. It is heated electrically by use of a DC power supply, and so the dissipated heat can be calculated directly from its voltage and resistance. Programmable DC power supply (ePower SPS150) provides the voltage and two Agilent Multi-meters (34410A and 34401A) are used to record voltage and current on the heater. The wire temperature can also be determined from its electrical resistance. The electric resistance of the platinum wire has a linear relationship with its temperature. The temperature coefficient of the platinum wire is found to be 0.00399 C^{-1}. Two thermocouples are used to measure the bulk temperature of the fluids. The flow rate is maintained at 0.2L/min for current tests, but can be varied between 0.12 and 2.2L/min via the MAG drive gear pump (model number: FG213 and its mechanical data is attached in Appendix. The flow rate is monitored by a flow meter (King instrument company).

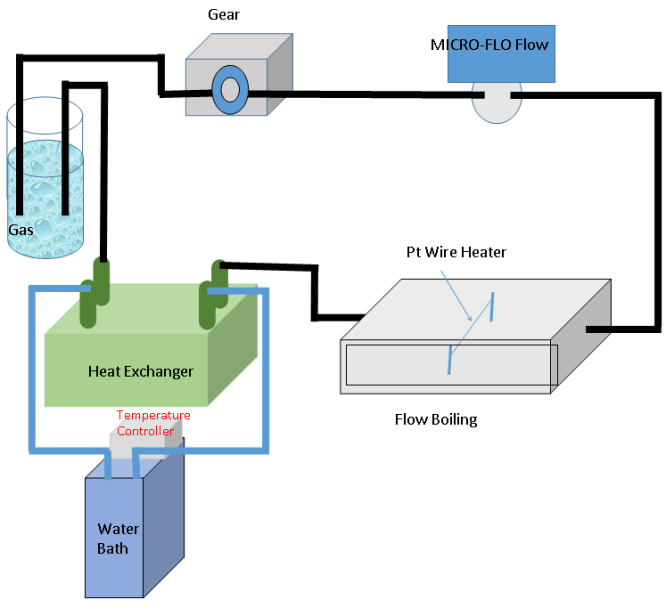

Fig. 3.7: Flow boiling test apparatus

For both the pool and flow boiling, the following targets are focused: 1. Identify the effect of surfactants on the nucleate boiling heat transfer. 2. Identify the effect of added low boiling point nanodroplets on the nucleate boiling heat transfer 3. Compare the effect of different surfactants and their concentration on boiling heat transfer characteristics of nanoemulsion fluids 4. Identify the effect of other base solvent fluids on the nucleate boiling heat transfer 5. Identify the effect of other boiling conditions (wire heater incline angle, subcooling) on boiling heat transfer characteristics of nanoemulsion fluids.

Measurement uncertainties

Table 3.1: Uncertainty of measurement variables

Measured Quantity	**Value and Uncertainty**	
	Range	$\pm(\%\ of\ Reading + \%of\ range)$
$\Delta V_{voltage\ sensor\ probes}$	100.0mV	0.0030+0.0030
	1.0V	0.0020+0.006
	10V	0.0015+0.0004
$I_{current}$	1.0mA	0.007+0.006
	10.0mA	0.007+0.02
	100.0mA	0.010+0.004
	1.0A	0.050+0.006
Temperature (Type K)	-50 to 1382^{O}F	1^{O}F
Flow meter	1GPM	± 3% to ± 6% of Full Scale

The uncertainties can be determined from the measurement uncertainties using calculus and the principle of superposition of errors. In general, for a variable that is a function of several variables, $F = F(a, b, c, \ldots)$, the squares of the uncertainty in F is

the sum of the square of the uncertainties due to each independent variable, $\delta F = [\left(\frac{\partial F}{\partial a}\delta a\right)^2 + \left(\frac{\partial F}{\partial b}\delta b\right)^2 + \left(\frac{\partial F}{\partial c}\delta c\right)^2 + \cdots]^{0.5}$ where δa denotes the uncertainty in a. Under most circumstances, the variation in the wire is less than 2 degree, and only, becomes significantly larger at very low current, when the voltage difference across the current sensing resistor is very small. The uncertainty in critical heat flux is also small and less than 3% for each measurement.

For both the pool and flow boiling test rig, consistency test is carried out to verify the usability of the system by testing the same fluid at multiple times using the different wire heaters (same material and length, just take from different section of the platinum wire bundle) and same wire heater before and after multiple boiling tests.

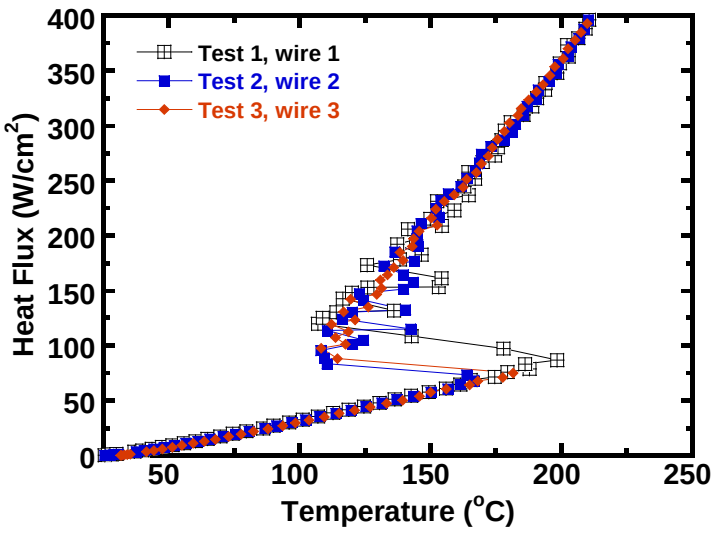

Figure 3.8 Consistency test using different wires in same sample

It can been from the Figure 3.8 shown above that, the different surface conditions such as surface roughness can affect the incipience of bubble on the heater surface which can delay or advance the nucleation as shown in Figure 3.9, however, after the

boiling happens, the three different curves follow almost the same line and it confirms that the surface roughness has a negligible effect on the boiling inside nanoemulsion fluids which is also consistent with others' findings.

It has been reported in others' study that the boiling of nanofluids can contaminate the heater surface[58, 61, 70] due to the sedimentation of nanoparticles on the heater surface which might be the reason for the observed enhanced heat transfer inside nanofluids. So here, to investigate whether there is contamination during boiling test inside nanoemulsion fluids, we tested the boiling curve of the same wire inside ethanol before and after several pool boiling tests inside nanoemulsion fluids to verify the repeatability of the test and also measured the resistance of the wire heater to identify any contamination to the heater. The results are summed up in the figures below:

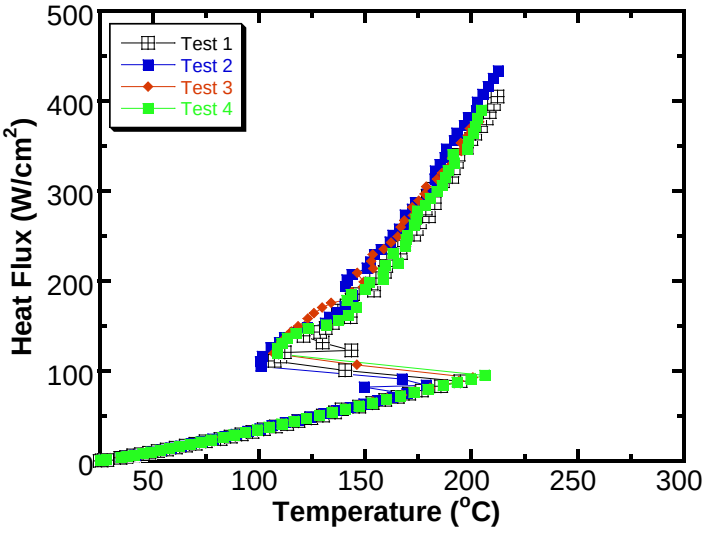

Figure 3.9 Consistency test using same wire for multiple tests

It can be seen here that all the boiling curves using same wire in same ethanol ethanol follow almost the same trend which confirms that there is no contamination on the heater surface during the boiling test of nanoemulsion fluids.

To further verify that, we also tested the resistance of wire heater for six hours continuously while it is immersed inside nanoemulsion fluids and undergoes nucleate boiling. The result is shown below:

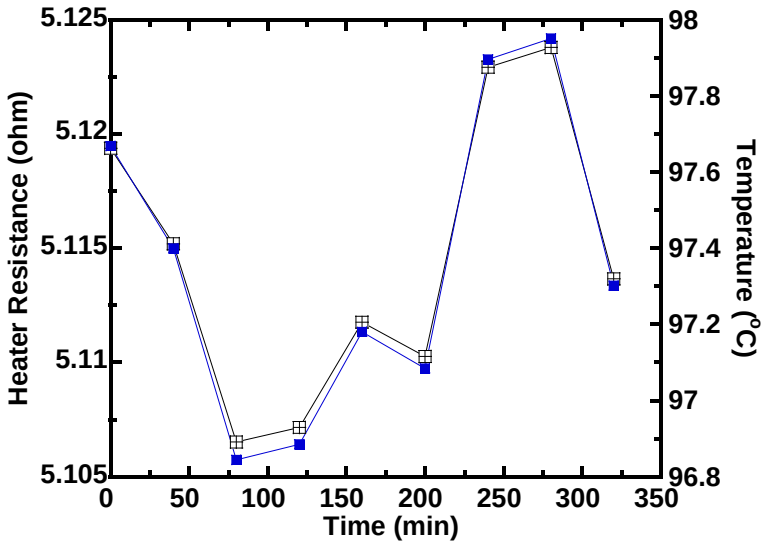

Figure 3.10 Consistency test for heater resistance

Visualization methods

Introduction

In-situ visualization is a very powerful method to characterize the bubble morphology during nucleation process and the methods of indicating flow patterns may be broadly classified into two groups: first, static methods, i.e those applied to boundary

surfaces, and second, kinetic methods, i.e. those applied in the fluid itself, either in the free stream or in the boundary layer.

Static methods

Because there is “no slip” of a fluid continuum at a solid boundary, surface methods of visualization cannot strictly be regarded as illustrating fluid motion. They can, however, indicate the gross distribution of shear stress and therefore of velocity gradient for steady flow and from this some characteristics of the flow in the boundary layer may be deduced.

In air flow good indication of velocity gradient at the surface have been obtained by evaporation and sublimation methods. A somewhat similar technique, which depends on different rates of solution of a surface coating, has been developed for water flows. These methods of indicating flow behavior may be described as static techniques. They don’t faithfully indicate disturbances in the main flow even though the latter may affect the flow in the boundary layer.

Kinetic Methods

The oldest of these methods, applicable to flow in an open channel, consists simply of scattering on the liquid surface a light power (such as aluminum or lycopodium) and illuminating the particles.

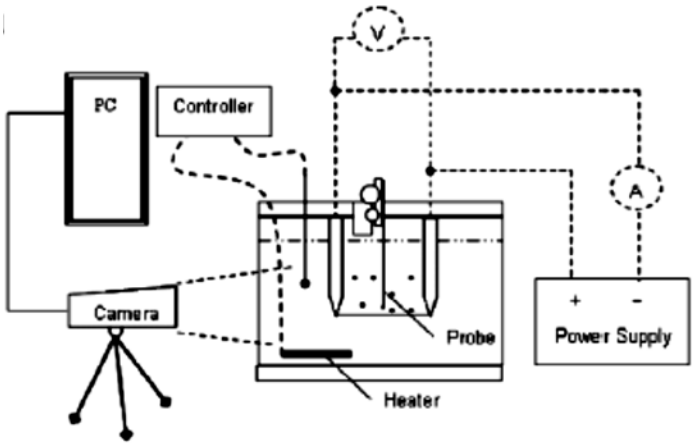

Fig. 3.11 High speed camera test set-up

In our study, we focus on studying the bubble nucleation dynamics under pool boiling condition to have a better understanding of the effect of nanodroplets on the incipience of boiling process and the possible reason for the enhanced heat transfer capability. We use Phantom V640 high speed camera to capture the bubble nucleation rate and bubble morphology. The Phantom V640 high speed camera can capture image at resolutions of 2560 x 1600 @ 1,500 fps and the shutter speeds down to 1 microseconds with supports for 8- and 12-bit pixel depth. Depending on the memory size on the camera, it can record video at different length and frame rate per second with different resolution. In our study, we want to capture the whole boiling range, so there is a compromise between the frame rate and resolution in order to keep the whole video file size less than 8 Gb. Our setting for the experiments is at a resolution of 800*640 @ 100f/s, which gives us an approximately 10 minutes recording length. The high-speed camera set-up is shown in Appendix.

Chapter 4: Ethanol-in-PAO Nanoemulsion Fluids

Introduction

Ethanol also known as methyl ethanol, is a chemical with the formula CH_3OH (often abbreviated MeOH). It has boiling a temperature of 64.7°C, which is much lower compared to base PAO fluid. It is proposed that adding low boiling temperature ethanol will alter the boiling heat transfer characteristics of based PAO fluid via forming phase-changeable ethanol nanodroplets inside.

The picture of the formed Ethanol-in-PAO nanoemulsion fluid is shown below: the following Figures 4.1 are the pictures of Ethanol-in-PAO nanoemulsion heat transfer fluids prepared with ionic surfactant and pure PAO fluid. They are transparent to natural lights but can be identified using Tyndall Effect [10, 13, 15, 39]. These nanodroplets formed inside are in fact swollen micelles in which the outer layer is composed of surfactant molecules having hydrophilic heads and hydrophobic tails which scatter the laser light and show the Tyndall effect.

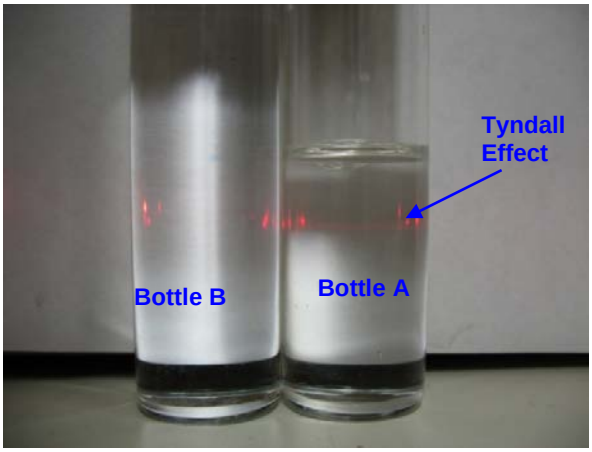

Fig. 4.1: Pictures of Ethanol-in-PAO nanoemulsion fluids from left to right

Structure characterization using SANS and DLS

The structures of the three groups of samples are characterized using the Small Angle Neutron Scattering (SANS) technique as introduced in previous section. In our SANS experiment, samples are prepared using deuteration methods to achieve the needed contrast between the droplets and the solvent. SANS measurements are conducted on the NG-3 (30 m) beamline at the NIST Center for Neutron Research (NCNR) in Gaithersburg, MD. Samples are loaded into 2-mm quartz cells and kept under room temperature.

The scattering intensity I versus the scattering vector $q = 4\pi \sin(\theta/2)/\lambda$ is plotted to represent the SANS data, where λ is the wavelength of the incident neutrons, and θ is the scattering angle. The approximation $q = 2\pi\theta/\lambda$ is used for SANS (due to the small angle θ). The empirical models are used to fit the SANS data with the IGOR Pro software under the protocol from NCNR NIST.[10, 147, 148] Detailed data reduction procedure is introduced in Appendix.

The SANS data for Ethanol-in-PAO nanoemulsion heat transfer fluids with four surfactants are summarized and compared as follow:

Ethanol-in-PAO nanoemulsion fluids	PAO (g)	Ethanol (g)	Ethanol-Nanodroplets Radius (A)
Sample 1	13	0.06	2.69
Sample 2	13	0.11	5.29
Sample 3	13	0.175	7.44
Sample 4	13	0.05	5.27
Sample 5	13	0.13	5.55
Sample 6	13	0.2	5.9

The SANS scattering intensity versus the wave length for the six samples are shown below:

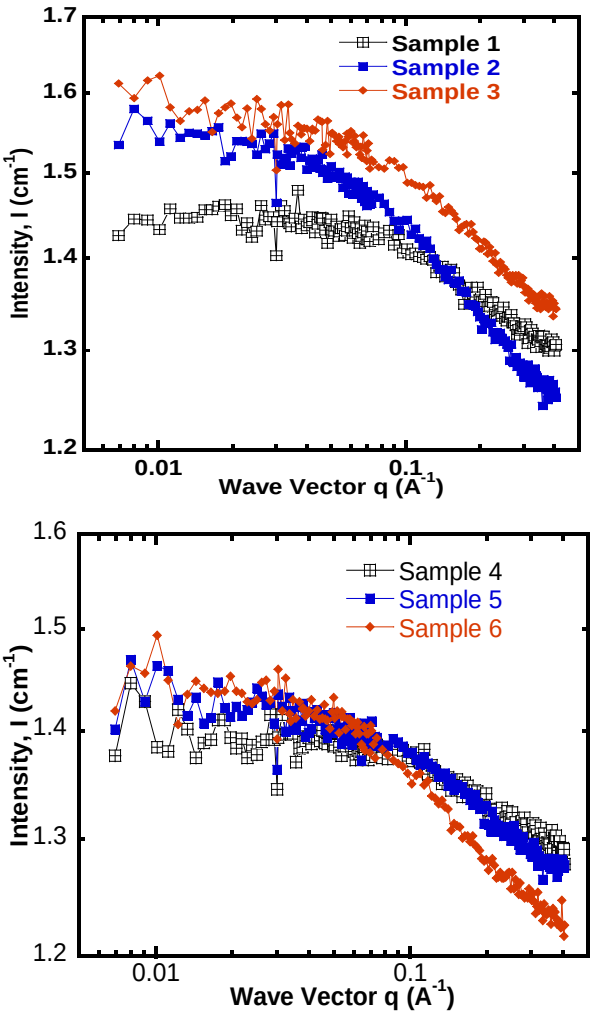

Figure 4.2 SANS data Intensity versus wave vector for Ethanol-in-PAO nanoemulsion fluids

It can be seen here that the intensity curves fall very close to each other at different ethanol concentrations in Figure 4.2 (a) and (b). In Figure 4.2(a) with lower surfactant concentration, the variation with ethanol concentration is less apparent compared to previous samples with non-ionic surfactants in both low q and high q range; in Figure 4.2(b) , the effect of ethanol is even less obvious where all three curves fall together

with gradually decreased higher q region. In both high and low surfactant samples, the inner structures are very different from those with non-ionic surfactant, and the different types of surfactant have a strong effect on inner structure in nanoemulsion fluids.

Following standard SANS data reduction and analysis procedure, the radii of the ethanol nanodroplets inside are reduced, shown in Figure 4.3 below:

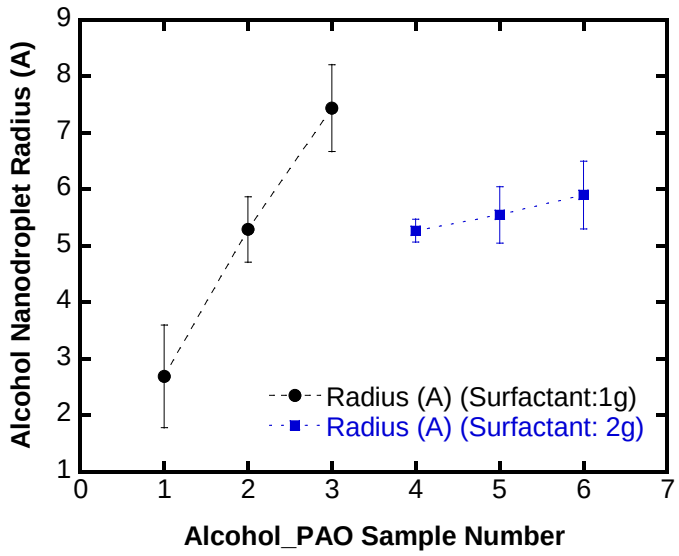

Figure 4.3 Ethanol Nanodroplets Radius inside Ethanol-in-PAO nanoemulsion fluids with different surfactant concentrations

It can be also seen here that the inner ethanol nanodroplets size still increase linearly with higher ethanol concentration at fixed surfactant concentration, but at different scales. The higher concentration of surfactants tends to keep the size of inner ethanol core to be constant. It is helpful to image the surfactant molecules try to attach to the surface of ethanol molecule with the addition of more ethanol while the one with high surfactant concentration can surround more ethanol molecules and keep the size to be

nearly constant because they always try to form the system which least surface energy. However, the uncertainty of the measured inner nanodroplets size is increased, partially due to the different interfacial layer organization for charged molecules inside ionic surfactant solution and partially, for the relatively smaller size which is closer to the resolution limit of SANS. It is also noteworthy that here the concentration of surfactant has a dominating effect, which keeps the radius of ethanol nanodroplets to be almost constant at higher concentrations, as shown in Figure 4.3. It can be seen clearly here that the molar ratio of ethanol/surfactant has a strong effect on inner structure and nanodroplets size inside Ethanol-in-PAO nanoemulsion fluids, which is also expected to affect their thermophysical properties.

Viscosity

One of the most easily observed macroscopic properties of colloidal systems is their flow behavior, and among them, viscosity is one important rheological property of liquid suspensions that can be easily measured.

Viscosity, as it is observed for a given system, depends largely on the structure, i.e., the type of aggregates that are present, their interactions, and the concentration of the system. In principle, rheological measurements contain information regarding these parameters, and dynamic rheological experiments can also yield information on the dynamics of the given system.

The first general fact about viscosity in colloidal system had been studied since Einstein: whenever a second phase is dispersed in a solvent this should lead to an increase in the bulk viscosity and the solid theoretical description of this effect is given by the Einstein equation as,

$$\mu_{sus} = \mu_{fluid}(1+2.5\phi) \qquad (4.1)$$

where μ_f is the viscosity of base fluids and ϕ is the volume fraction of solid dispersed particles. This equation holds only if the suspension is dilute, i.e., the volume fraction of solid particles ϕ is not more than 0.03, when the interactions between solid particles are negligible.

Einstein's formula is valid for hard spheres, but it is modified for the case of a dispersion of liquid spheres in another liquid medium. For that case Taylor obtained the expression

$$\mu_{sus} = 1+\phi\left(\frac{\mu_s + 2.5\mu_d}{\mu_s + \mu_d}\right) \qquad (4.2)$$

Where μ_s is the viscosity of the solvent and η_d that of the dispersed phase. This expression reduces to Einstein's equation for the case of hard spheres and will yield lower values for η_{sus} (with a lower limit of a factor of 1 instead of 2.5 for the case where $\mu_s \gg \mu_d$.

It might be noted here that accordingly the viscosity given in Einstein's equation is valid only for relatively dilute systems. With increasing particle concentration, the flow around one particle begins to be affected by other particles in the neighborhood

and the assumption does not hold any more. Solid particles, then, experience hydrodynamic interactions and the viscosity is not only linearly dependent on the particle concentration ϕ ,but also on some higher order ϕ^2 , ϕ^3 ,… This effect of hydrodynamic interactions on viscosity of suspensions was studied by Batcherlor[149], and he concluded that the coefficient of the second-order term was 6.2, that is

$$\mu_s = \mu_{fluid}(1 + 2.5\phi + 6.2\phi^2 + ...)) \qquad (4.3)$$

This equation enables the calculation of the viscosity of suspensions at a particle concentration up to 10 vol%. Besides, nanoemulsion fluids are usually Newtonian fluids, i.e., their viscosity is independent of the applied shear stress. For such a situation, the applied shear stress does not affect the equilibrium structure, and for this case, viscosity measurements can yield information regarding this equilibrium structure.

Here, it has been seen that the concentration of surfactant and added ethanol has a strong effect on the nanoemulsion fluids' inner structure, and as the rheological properties depend heavily on the inner structure, the rheological property of ethanol-in-PAO nanoemulsion fluids is measured and compared here. In order to have a better understanding of their rheological properties and the dependence upon the surfactant concentration and added ethanol, the commercial viscometer is used for viscosity measurement. Since, the concentration of ethanol that can be added inside is very limited, the focus here is on the effect of the different kinds of surfactants and their

concentration. Effect of ethanol on the formed Ethanol-in-PAO nanoemulsion fluids will also be investigated.

The effect of the surfactant concentrations are shown below in Figure 4.4 where similar surfactants of three different concentrations (4, 8, 16 % by mass) are compared here:

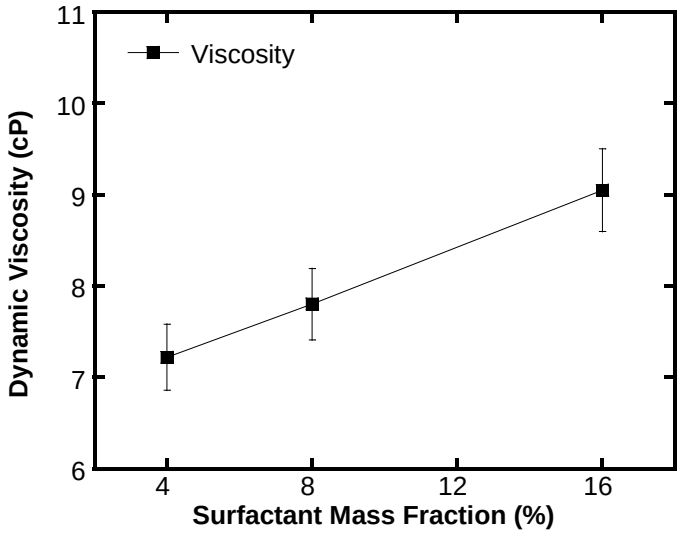

Figure 4.4 Viscosity inside Surfactant/PAO nanoemulsion fluids

Ethanol is added into previous surfactant/PAO mixture and their effect is also summarized as follow in Figure 4.5:

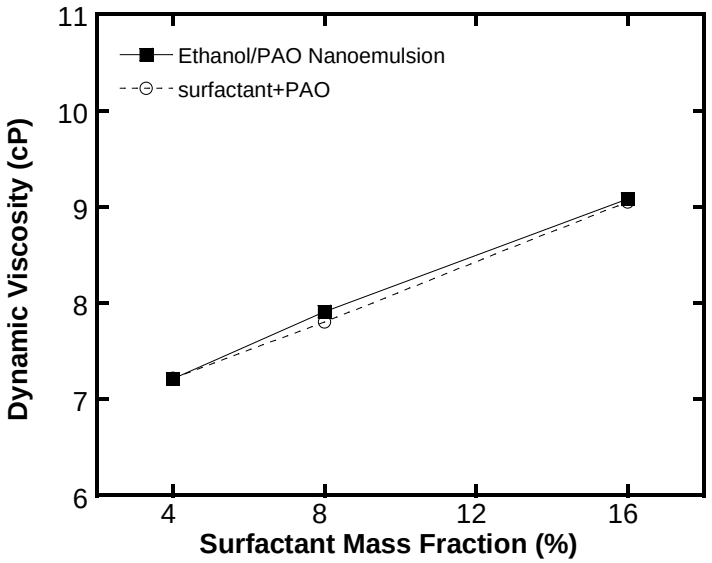

Fig 4.5 Viscosity inside Ethanol-in-PAO nanoemulsion fluids with different surfactants and concentrations

It is shown clearly here that the addition of ethanol will increase the viscosity in all three Ethanol-in-PAO nanoemulsion fluids, which agrees with Einstein prediction. Similarly, the addition of ethanol doesn't affect the trend of viscosity much and all of the viscosity increase with higher concentration of ethanol, but with different percentages.

Thermal conductivity

Thermal conductivity is another important thermophysical property, which has been used widely for indexing the heat transfer capability of heat transfer fluids that is, however, one to two order's lower in fluids compared to solid. So, lots of research has been carried out to enhance the thermal conductivity of conventional heat transfer fluids. Recent findings in nanofluids brought up a debate on the Brownian motion of nanosized particle and particle sedimentation on the enhancement of thermal conductivity observed in nanofluids. Here, ethanol (0.21 W/mK), which has a thermal

conductivity very close to that of base PAO fluid, (0.143 W/mK) is chosen here to help understand this phenomena as the ethanol nanodroplets inside are less than 5nm in DI, which will have a strong Brownian motion. The 3ω wire method has been used for the thermal conductivity measurement and the result is shown in Fig. 4.6 as below:

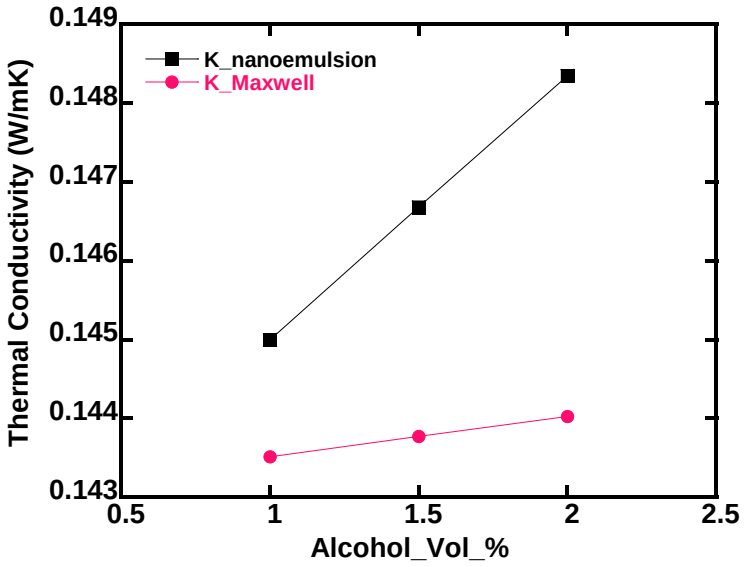

Fig 4.6 Thermal Conductivity inside Ethanol-in-PAO nanoemulsion fluids with different surfactants and ethanol concentrations

It can be seen here that for the Ethanol-in-PAO nanoemulsion fluids with various ethanol concentrations, the thermal conductivity is only increased very moderately, up to 1.3% increase. So, there is no strong effect of Brownian motion on thermal conductivity as observed in ethanol-in-PAO nanoemulsion fluids here.

On the other hand, the observed thermal conductivity all increase linearly with higher concentration of ethanol which is consistent with the trend observed in viscosity. One interesting observation here is that the surfactant has a strong effect on the

dependence of viscosity with ethanol concentration, and the only ionic surfactant gives a different thermal conductivity slope same as in the viscosity.

It can be seen that the classic Maxwell equation predicts similar increases of thermal conductivity inside ethanol-in-PAO nanoemulsion with higher loading of ethanol, but it under predicts the enhancement of thermal conductivity in both absolute value and trend. The Maxwell's equation for suspensions of well-dispersed, non-interacting spherical particles is,

$$k_{maxwell} = \frac{k_p + 2k_o + 2\phi(k_p - k_o)}{k_p + 2k_o - \phi(k_p - k_o)} * k_o \quad (4.4)$$

where k_o is the thermal conductivity of the base fluid, k_p is the thermal conductivity of the particles, and ϕ is the particle volumetric fraction. Equation 4 predicts that the thermal conductivity enhancement increases approximately linearly with the particle volumetric fraction for dilute nanofluids or nanoemulsion fluids (e.g., ϕ<10 %), if $k_p > k_o$ and there is no change in particle shape.

Pool boiling

So far, the viscosity and thermal conductivity inside Ethanol-in-PAO nanoemulsion fluids have been studied and they are found to depend heavily on the surfactant concentration and ethanol concentration as well. Now as discussed before, the boiling process can be affected by many factors such as surfactant and nanodroplets. With some many variables which can affect the nucleate heat transfer performance, it is very meaningful to carefully look into their effect. Here, in order to investigate the

possibility of using the nanoemulsion fluids as phase change heat transfer carrier, we focus on the nucleate boiling heat transfer coefficient (from nucleate part of boiling curve), onset temperature of boiling curve, and critical heat flux. We want to see the effect of forming nanoemulsion heat transfer with low-boiling point nanodroplets inside while comparing with the effect of surfactants solely. All the tests are carried out using 25um wire heater and following the configuration shown in the pool boiling introduction section. All test samples are kept at room temperature (25^{o}C) and 1 atm. The test and results are summarized and compared following the procedure: 1. Identify the effect of surfactants on the nucleate boiling heat transfer. 2. Identify the effect of added low boiling point ethanol on the nucleate boiling heat transfer. So, the pool boiling tests for the ethanol-in-PAO nanoemulsion fluids are carried out using the pool boiling set-up introduced before in section 3.

Using the pool boiling test rigs introduced before, the nucleate boiling heat transfer properties of ethanol-in-PAO nanoemulsion fluids are investigated and compared below.

Surfactant concentration effect on boiling curve:

Five concentrations of surfactant-in-PAO nanoemulsion fluids are investigated for the effect of added surfactants on the boiling properties: 13.3%, 7%, 3.7%, 1. 5% and 0% sample.

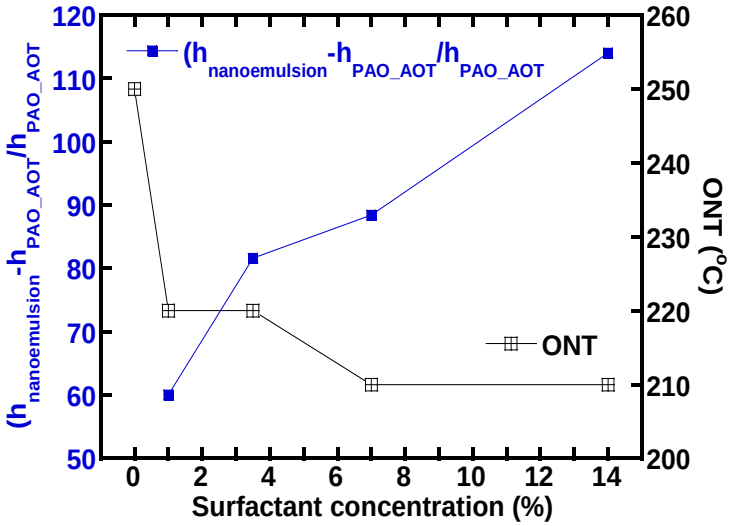

Figure 4.7 ONT and heat transfer coefficient enhancement for PAO at different surfactant concentrations

To further compare the effect of surfactants on the ONTs and boiling heat transfer coefficient, their dependence with surfactant concentration are plotted in Figure 4.8: the onset temperature of boiling (ONT) on the right y axis seems to decrease with higher surfactant concentration, then decreased slowly to around 220^{o}C, and then, decreased to 210^{o}C with more surfactant added. However, the ONTs for all PAO fluids with surfactants are still very high.

If, we compare the boiling heat transfer coefficients of PAO fluids with different surfactant concentrations, we can see the trend from the blue curve on the left y axis in Fig. 4.8. The base PAO boiling heat transfer coefficient is considered as 1 and all the other fluids are compared with them to see the effect of the surfactant. It can be seen that the heat transfer coefficient increases with higher surfactant concentration almost linearly and it increases sharply at highest surfactant concentration. At the

highest concentration of surfactant, it can increase the boiling heat transfer coefficient up to 110% .

Ethanol concentration effect on the boiling heat transfer of Ethanol-in-PAO nanoemulsion fluids

As stated before, the low boiling point ethanol is added inside to enhance the boiling heat transfer properties of the system, and here, the effect of ethanol and its concentration is summarized and shown in Fig. 4.8 below:

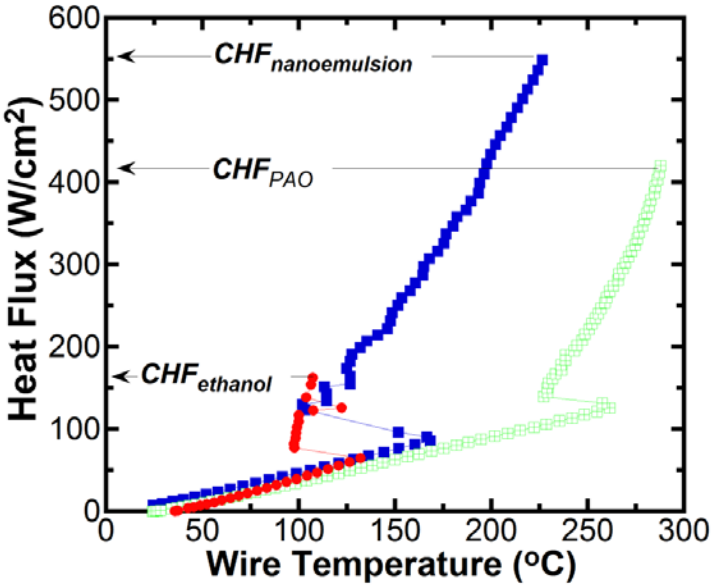

Figure 4.8 Pool boiling curve for Ethanol-in-PAO nanoemulsion fluids with pure Ethanol and PAO

It is shown clearly here that the adding of ethanol greatly shifts the boiling curve to the left with a lower ONT compared to pure PAO fluid. If compared with pure Ethanol, it can be seen that the nanoemulsion fluid have a much wider operation range(higher CHF and temperature range) compared to pure ethanol. The addition of

nanosized ethanol droplets can boost the boiling heat transfer coefficient upto 300% increase compared to pure PAO at 200^{o}C.

One thing worth noting here is that the nucleation temperature of ethanol-in-PAO nanoemulsion fluids are over 100 degree higher than their atmospheric boiling point and very close to thermodynamic limit of superheat or spinodal state of ethanol. The spinodal states, defined by states for which $\left.\frac{\partial P}{\partial V}\right|_{T,n} = 0$, represent the deepest possible penetration of a liquid in the domain of metastable states, and is not usually observed in conventional boiling process [150-152]. Similar phenomena have been reported in others' study of dilute emulsions [71, 72, 75, 76, 78], but no satisfactory explanation is available yet.

It is found that when the liquid vaporize after reaching their limit of superheat, the energy released could create a sound-shock wave, so-called vapor explosion. This sound wave would lead to strong fluid mixing within the thermal boundary layer, therefore, enhancing the fluid heat transfer. This might explain the observed greatly enhanced heat transfer after nucleation happens in these nanoemulsion fluids

Flow Boiling

To see the effect of flow motion on the boiling curve of these nanoemulsion fluids, here the ethanol-in-PAO nanoemulsion fluids are test here:

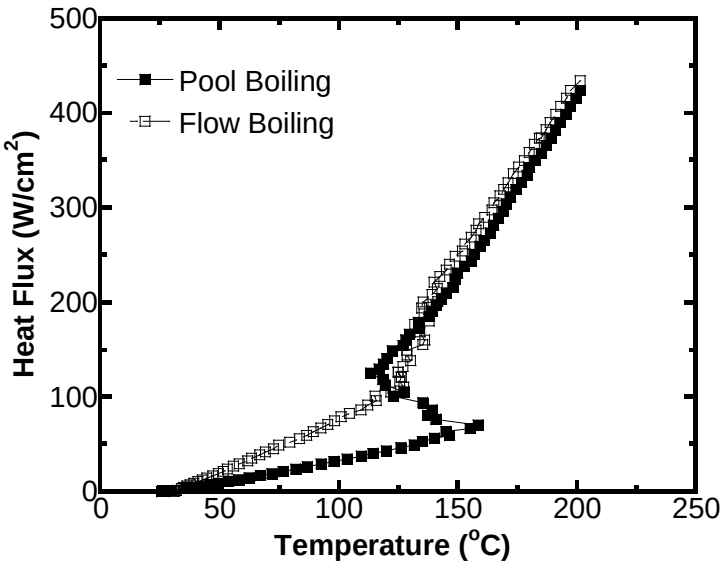

Figure 4.9 Comparison of flow and pool boiling curves for ethanol-in-PAO nanoemulsion fluids

It can been seen here that the solid black square is pool boiling curve and the hollow black square is the flow boiling—very similar to the trend observed in the ethanol-in-PAO nanoemulsion. Here the pool boiling and flow boiling fall together after the nucleation happens, while the difference is mainly at the natural convection part too. The flow motion eliminate the superheat needed for the incipience of boiling where the pool boiling has a roughly 40^{o}C degree superheat. The difference here is that even though the flow rate is controlled at the same, the flow boiling curve for ethanol-in-PAO falls lower than the flow boiling curve in ethanol-in-PAO nanoemulsion especially in natural convection part which might due to the different bubble dynamics and fluid viscosity.

Chapter 5: Water-in-PAO Nanoemulsion Heat Transfer Fluids

Structure Characterization

Figure 5.1 shows the SANS data for water-in-PAO nanoemulsion fluids with water volumetric concentration covering 1.8 Vol% to 10.3 Vol%. Two empirical fittings are used to find out the inner structure.

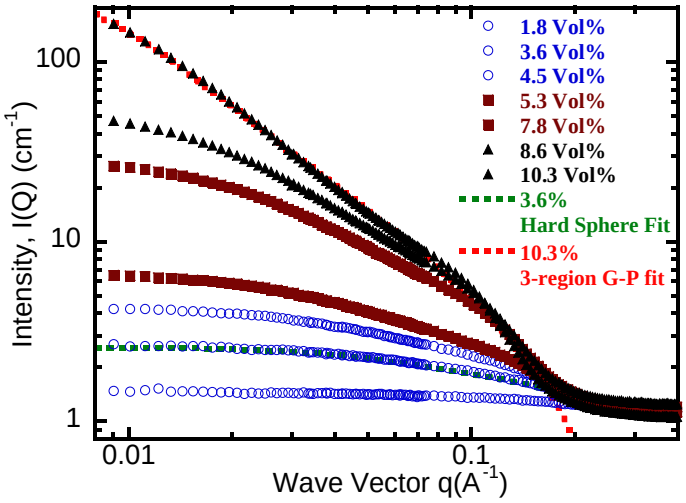

Fig. 5.1: SANS scattering curve Intensity I vs Wave Vector q with curve fitting

It can be seen in this figure that the neutron scattering curves fall in to different groups: for water loading of 1.8~4.5 %, the curves level off when the scattering intensity q is less than 0.1 A^{-1}. In contrast, the curves have a downward sloping shape for water loading of 5.3%~7.8 % while the curves shift to a more obvious ternary form for water loading of 8.6% and 10.3%. The hard sphere model fits well for low water concentration curves (i.e. 1.8~4.5 vol.%), the nanodroplet radii are found to be 13.2Å, 25.6Å, and 96Å for water loading 1.8 vol.%, 3.6 vol.%, and 4.5 vol. %, respectively. For higher water concentration (i.e. 7.8 ~10.3 vol.%), the hard-sphere

model doesn't fit well, especially, for scattering q less than 0.1 A^{-1} region, which suggests that those nanodroplets are not simply spherical. The 3-region Guinier-Porod empirical model is used to determine the nanodroplet geometry by fitting the SANS data, especially, for scattering q less than 0.1 A^{-1} region.

According to the 3-region Guinier-Porod model[153], there are two dimensionality parameter S_1 and S_2, and plus R_{g2} and R_{g1} are the radii of gyration for the short and overall sizes of the scattering object. The fitted curves give $S_2 = 0.22$, $S_1 = 1.4$ and $R_{g2} = 121\dot{A}, R_{g1} = 4.6\dot{A}$ for 10.3 Vol.% sample. For 7.8 Vol.% one, $S_2 = 0.18, S_1 = 0.97$ and $R_{g2} = 47.4\dot{A}, R_{g1} = 5.2\dot{A}$. The dimensionality parameters suggest that those nanodroplets have a cylinder-like shape. The SANS data suggests there is an inner structure variation with water loading inside water-in-PAO nanoemulsion fluids; the effect of its structure change on thermal properties will be introduced later.

Thermal conductivity

Figure 5.2 shows the thermal conductivity enhancement in water-in-PAO nanoemulsion fluids as a function of the loading of water from 0.47 Vol% to 8.6 Vol% at room temperature. Pure PAO is used for calibration and its measured value $k_{PAO} = 0.143 W/mK$ agrees well with literature value.[154]

It can be seen that the thermal conductivity increases linearly with water volume fraction. A maximum increase of 16% is observed at water volume concentration equals 8.6 Vol%. The observed enhancements in thermal conductivity agree with the predictions from the classic Maxwell equation, with the assumption of spherical droplets. The Maxwell's equation for suspensions of well-dispersed, non-interacting spherical particles is,

$$k_{maxwell} = \frac{k_p + 2k_o + 2\phi(k_p - k_o)}{k_p + 2k_o - \phi(k_p - k_o)} * k_o \quad (5.1)$$

where k_o is the thermal conductivity of the base fluid, k_p is the thermal conductivity of the particles, and ϕ is the particle volumetric fraction. Equation 5.1 predicts that the thermal conductivity enhancement increases approximately linearly with the particle volumetric fraction for dilute nanoemulsion fluids (e.g., ϕ<10 %), if $k_p > k_o$ and no change in particle shape.

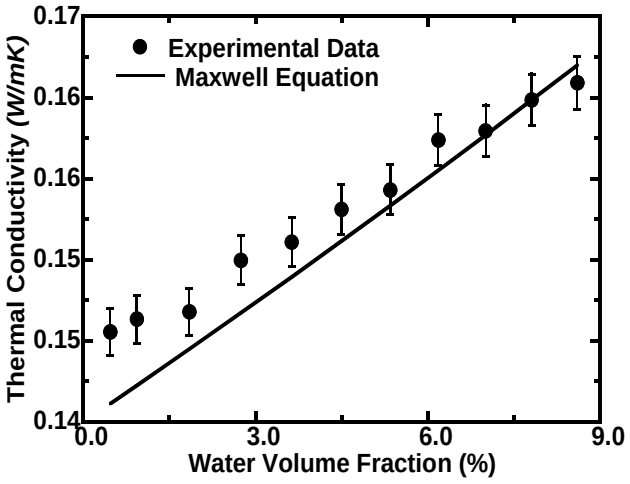

Fig. 5.2: Thermal conductivity of water-in-PAO nanoemulsion fluids versus water volume fraction. The prediction from the Maxwell equation is shown for comparison.

Viscosity

The dynamic viscosity of water-in-PAO nanoemulsion fluids was measured at room temperature; the viscosity's dependence upon the water volumetric concentration is shown in Figure 5.3. The calibration is carried out using the pure PAO and its dynamic viscosity is found to be 7.3 cP which compares very well with the literature values. The test samples exhibit a shear-independent characteristic of Newtonian fluids for the spindle rotational speed from 10 to 30 rpm. It can be seen in Figure 5.3 that the viscosity first increases with water concentration, then reaches a maximum at 5.3 Vol%, and then decreases. This trend is different from the thermal conductivity shown in Figure 5.2, and the maximum viscosity can be attributed to the attraction force between droplets within the nanoemulsion fluids. As the amount of water is increased, the surfactant molecules become hydrated, while releasing their counterions into water. The exchange of surfactants molecules and counter-ions between the droplets could make themselves charged oppositely. The interdroplet attraction increases with water concentration until the hydration process is complete. This leads to a maximum viscosity in Water-in-PAO nanoemulsion fluids. It also coincides with the nonlinear inner structure change upon the water concentration as seen in SANS measurement result in Figure 5.3.

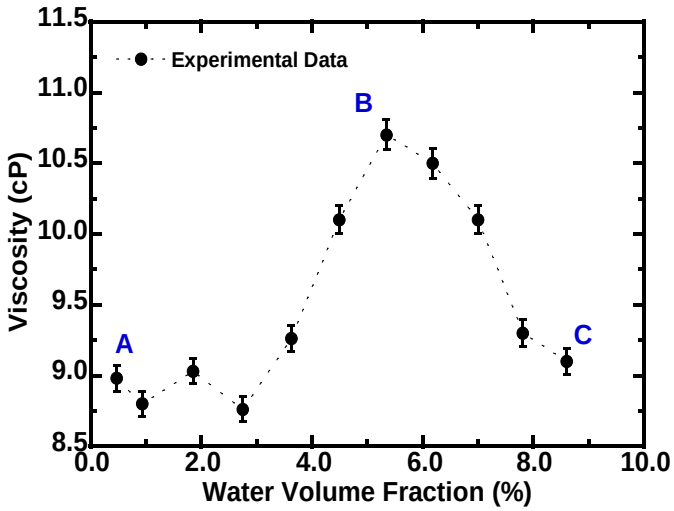

Fig. 5.3: Dynamic Viscosity of Water-in-PAO nanoemulsion fluids versus water volume fraction

Pool boiling characteristics

Effect of water concentration on the pool boiling curve

Variation of the pool boiling curves for the nanoemulsion fluids with water volumetric concentration below 4.5% are plotted in Figure 5.4 (a), and for concentrations above 5.3 vol. % in Figure 5.4 (b). As shown in Figures 5.4, all tested Water-in-PAO nanoemulsion fluids start to boil at around 170^{o}C. At low heat flux levels, single-phase natural convection appears to be the same for all Water-in-PAO nanoemulsion fluids and for pure PAO. This indicates that without phase transitions, water nanodroplets have insignificant effect on the fluid heat transfer, which is consistent with the measured thermal conductivity and viscosity described in the previous sections. At sufficiently large wall superheat (about 70 ^{o}C), nucleate boiling begins on the heater surface in these nanoemulsion fluids. After boiling incipience the

curves have a similar slope and appear to coincide for the Water-in-PAO nanoemulsion fluids with different water concentrations. The heat transfer coefficient (HTC) for the water-in-PAO nanoemulsion fluids has a 3.3 fold increase compared to pure PAO.

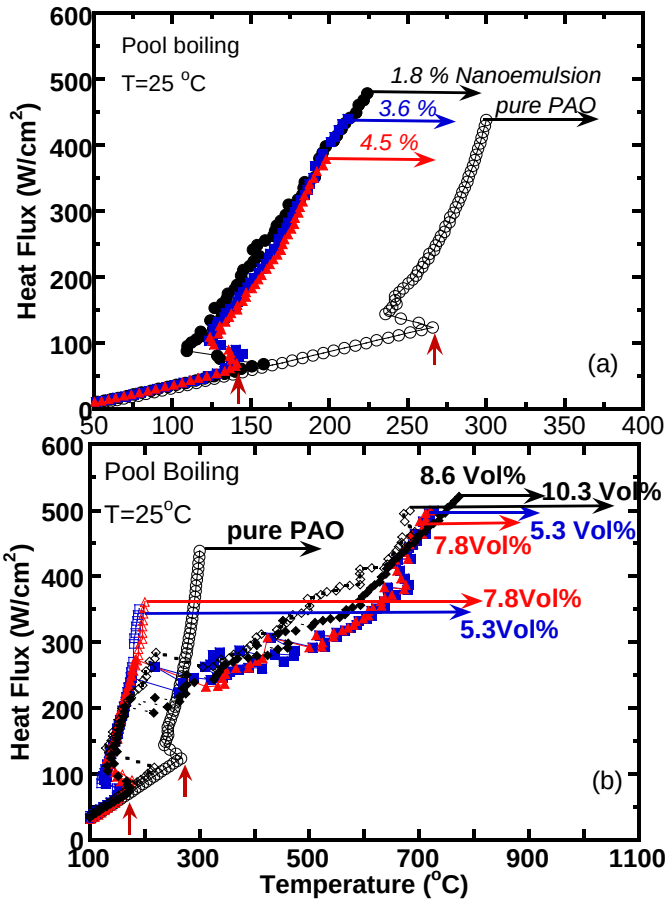

Fig. 5.4: Pool boiling curves for water-in-PAO nanoemulsion from 1.8 Vol% to 10.3 Vol%. The arrows in the figure represent where the burn out of wire occurs

An interesting phenomenon observed in the Water-in-PAO system is that pool boiling of the Water-in-PAO nanoemulsion fluids randomly varies between two different curves when the water concentration is larger than 5.3 Vol%, as shown in Figure 5.4(b). In one set of boiling curves, the wire burnout occurs right after the critical heat

flux is reached, without experiencing transition and film boiling. This set of curves is plotted with hollow symbols in Figure 5.4(b). In the other set of curves, they shift from nucleate boiling to transition boiling at a lower heat flux, and that the wire burns out in the film boiling regime. These curves are plotted in Figure 5.4(b) with solid symbols. If the water content is increased above 8.6%, the wire burnout always occurs in the film boiling regime. It was also observed experimentally that the probability of the occurrence of the first type of boiling curves decreases with increasing water loading. It might be related to the inner structure change with different water loading which was shown in SANS data that the water nanodroplets seem to change from sphere to elongated cylinder when the water concentration increases above 5.3 vol. %. No satisfactory explanation to this observed structure-property relation is currently available since the mechanism of nanoemulsion boiling is little known.

The probabilities of falling into which curve are also summarized in Table 1. In table 1, five tests are carried out for every water-AOT-PAO nanoemulsion fluid of water volumetric concentration from 5.3% to 8.6%. It can be seen that the occurrence of the 1st boiling curve (shown using solid symbols in Figure 3) or 2nd boiling curve (shown using hollow symbols in Figure 3) is random and affected by water concentration.

Table 5.1: Summary of chance of boiling curves for Water-in-PAO nanoemulsion fluids: water volume concentration from 5.3% to 8.6%.

Test	Water volume percentage				
	5.3%	6.2%	7%	7.8%	8.6%
1	1st	2nd	2nd	2nd	2nd
2	2nd	2nd	1st	1st	2nd
3	2nd	2nd	2nd	1st	2nd
4	1st	1st	2nd	2nd	2nd
5	1st	2nd	2nd	2nd	2nd

*1st and 2nd means the different boiling curves.

Subcooling effect

The effect of different subcooling conditions on the pool boiling process is also investigated. The initial temperature of Water-in-PAO nanoemulsion fluids is controlled to be 25°C and 50°C using water bath. The result for water-in-PAO nanoemulsion of water volumetric concentration of 6.2% is shown in Figure 5.5. It can be seen that the subcooling has an insignificant effect on the boiling curve before nucleation happens, but it affects the possibility of following the second boiling curve(as shown using the solid symbols). In addition, the critical heat flux (CHF) for lower subcooling ones is suppressed while the maximum heat flux on the Platinum wire heater is also decreased.

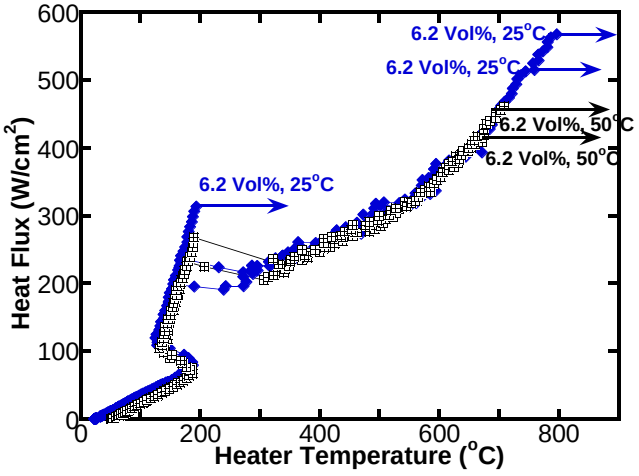

Fig. 5.5 Pool boiling curves for Water-in-PAO nanoemulsion fluids of water 6.2 Vol% at two different liquid temperatures: 25°C and 50°C.

The bubble morphology on wire is believed to affect the nucleation process and the heat transfer between wire and fluid, meanwhile the added nanodroplets are believed to be the main important factor inside the nucleation and their interaction.

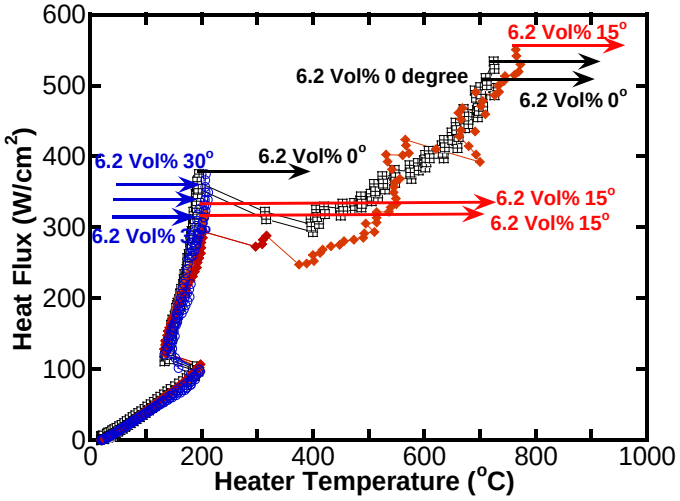

Fig. 5.6 Pool boiling curves for 6.2 Vol% Water-in-PAO nanoemulsion fluid at different inclination angles

For all the samples tested at 5.3 Vol% to 7.8 Vol% water loading, they all follow the similar trend. However, the dependence of CHF on orientation angles is not obvious based on our observation.

Possible reason

In addition, according to Mitsuhiro's study [20, 21, 30, 31], there are three different phases inside (oligomeric, transient, and monomeric phase), as shown in Figure 5.7, depending upon the water/AOT molar ratio. It describes the charging process and gives the explanation of maximum viscosity in another way. The oligomeric phase corresponds to the hydration process before completion, where the charged droplets agglomerates together to form oligomeric state while increasing the viscosity (Point

A to Point B in Figure 5.3). After reaching point B (5.3 Vol% or water/AOT molar ratio), it enters the transient phase where the added water keeps increasing the droplets size while neutralizing the charge and decreasing the attraction in between, which lowers the viscosity (Point B to Point C in Figure 5.3); the monomeric phase represents the phase in which individual, large droplets are dispersed inside solvent with weak interaction in-between which gives low and almost constant viscosity(range after Point C in Figure 5.3 which is not measured in our test but reported in others work).

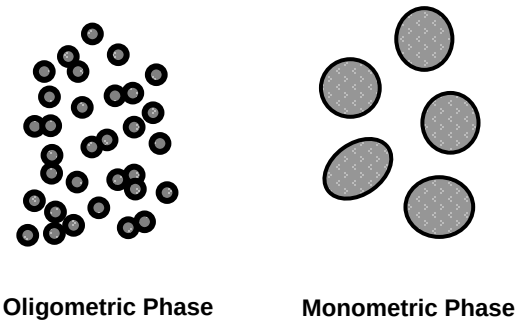

Figure 5.7 Schematic diagram for the Oligometric and Monomeric phase

The boiling curves are plotted separately in Figure 5.4 (a) and (b) because they can undergo two different boiling characteristics depending on the water volume concentrations. In Figure 5.4, the volume concentration of water is less than or equal to 4.5% (molar ratio). For all the water concentrations equal to or less than 4.5%, the boiling curve goes up, following the nucleation boiling curve after jumping back from boiling hysteresis, and then reaches a critical heat flux (CHF) that is equal to or less than 500W/cm^2 (CHF for 1.8 Vol%, 3.6 Vol% and 4.5Vol% ones are marked with arrow in Figure 5.4). However, if, water concentration is further increased, the boiling will change to be like in Figure 5.6 where the volume concentration of water is from

5.3% to 8.6% . The boiling curves after hysteresis can undergo two different boiling trends randomly: 1. same as the boiling curve for lower volumetric ones, it goes up following the nucleate boiling curve until reaching CHF which is shown in Figure 5.4 for 5.3 and 7.8 Vol%, using hollow symbols; 2. It will stop going up and jump to the right with a fast increase in temperature and slow increase in heat flux until the wire temperature is higher than the melting point of platinum. This boiling process for 5.3 and 7.8 Vol% is plotted with solid symbols of same the shape. The occurrence of either boiling curves for water volumetric concentration within 5.3% and 7.8% is random. However, if the water content is further increased, like 8.6% here, it will always undergo the latter boiling curve as shown with black solid symbol.

To help quantify the probability of the occurrence of first and second boiling mode, fives tests for each concentration are done for water volume concentration from 5.3% to 8.6% to see the chance of them being. It is concluded that the occurrence of nucleate (1st boiling curve) or mixed boiling (2nd boiling curve) is random and orderless. Overall, the chance of being mixed boiling increases with the higher water volumetric concentration. When the volume concentration is high enough like 8.6%, it will always undergo the latter one.

The occurrence of the two different boiling curves is found to be dependent upon the water concentration. One possible explanation is that the water concentration affects the inner structure of Water-in-PAO nanoemulsion fluids. As explained in the viscosity dependence of the water concentration [20, 21, 30, 31], lower volume

concentration (equal or less than 4.5%) ones are possibly in oligomeric phase (shown in Figure 5.7), where the water forms small droplets and then agglomerates inside the PAO solvent.

At high volume concentration (equal or higher than 8.6% here), there are only monomeric large water droplets (shown in Figure 5.7) inside, while for those with water concentration in between, they are likely to be within the transient phase. So, during the pool boiling test, these small droplets and oligomers get into contact with the hot platinum wire and the water inside quickly heats up and nucleate completely to form gas bubbles. These bubbles will leave the wire due to buoyancy, and this process continues until a maximum possible low rate in the counter flow of vapor away from the surface; the liquid towards the surface is reached where the wire temperature is increased to be higher than the melting point of platinum and the wire will break. However, it takes more heat and a longer time to vaporize the larger droplets in monomeric phase in contact with the wire before they can get enough buoyancy to leave the wire. So, they will remain attached to the wire and the locally vaporized water vapor will cover the wire which forms local film boiling and hinders heat transfer to the remaining water inside. The segment of wire underneath the bubbles was observed to be burning red. This local hotspot changes the heat and transfer pattern on the whole wire and the boiling curve as well. For those in between, the probability of oligomers being present at low water contents decreases and the phase boundaries shift to a low water content. Depending on the possibility of different structures of droplets meeting the wire, it may give the random occurrence

of the first or second boiling curve. However, more experimental data and in-vivo observation during pool boiling are needed to further clarify this phenomenon.

In summary, the thermophysical characteristics and inner structure dependence of water volumetric concentration in Water-in-PAO nanoemulsion fluids have been investigated experimentally. The thermal conductivity can be increased up to 16%, while the viscosity has a maximum value at water volumetric concentration equals to 5.3%. It has been found that the pool boiling characteristics are highly dependent upon the water volumetric concentration, which gives helpful advice on designing these kinds of nanoemulsion heat transfer fluids, via, carefully controlling the water volumetric concentration and the amount of water nanodroplets inside, to lower the boiling point by over 100^{o}C and increase the heat transfer coefficient by 3 times.

Chapter 6: Investigation of subcooling and heater orientation effect on the nucleate boiling heat transfer inside nanoemulsion fluids

Introduction

Boiling heat transfer has traditionally been thought of as a combination of free convection, vapor-liquid exchange, microconvection, transient conduction, and latent heat of vaporization. Vapor bubble dynamics associated with nucleation, bubble growth, departure, collapse, and subsequent rewetting of the heat surface characterize the classical ebullition cycle, which constitutes the central mechanism of heat transfer from a superheated wall during nucleate boiling in earth's gravity. Many researchers have characterized heat transfer from heater sizes much larger than the capillary length scale, L_b [155].

$$L_b = \sqrt{\frac{\sigma}{g(\rho_l - \rho_v)}} \qquad (6.1)$$

Such work has laid the foundation for the classical boiling curve and its constituent boiling regimes.

Experiments first conducted by Gunther and Kreith [156]showed that the majority of heat transfer during subcooled nucleate pool boiling can be attributed to microeconvection and not latent heat transport. For pool boiling near saturated conditions, Kim[157] showed that during one ebullition cycle, the majority of heat transfer occurs after the bubble departs through transient conduction and mciroconvection to the rewetting frequency. Methods aimed at increasing the bubble

frequency, such as electro-hydrodynamic pool boiling, have clearly shown an increase in attainable heat flux. Baboi et al [158]observed that dielectrophoretic forces tend to increase CHF by increasing the rate of bubble departure. Snyder et al,[159] while studying boiling from a platinum wire, observed an increase in nucleate boiling heat transfer and CHF in the presence of a strong electric field force co-linear with buoyancy. They concluded that the electric field acts to increase the forces acting on the bubbles promoting the rate of bubble departure. Such work characterizes the effect of two critical components of the ebullition cycle: the frequency of bubble departure or surface rewetting, f, and the bubble departure diameter, D_d.

The bubble departure diameter depends on the forces acting on the bubble during vapor bubble growth and departure. Surface tension, buoyancy, inertia of induced liquid motion, Marangoni or thermocapillary effects, and bulk fluid motion act to influence departure diameter. In addition, the magnitudes of these forces have been shown to be a function of bulk subcooling (ΔT_{sub}), gravity, wall superheat (ΔT_{sat}), the thermophysical properties of the fluid, heater geometry, surface characteristics, and pressure.

On the other hand, the surface characteristics of the heating element affect bubble generation and departure dynamics, which, in turn, affect the heat transfer coefficient. As previously mentioned, Straub showed that a smaller diameter wire was constantly

more effective at dissipating heat in 0g than in 1g, but a larger diameter wire was less able to withstand higher heat fluxes without wire burnout.

The surface orientation of the heater in nucleate boiling is also very important in immersed cooling technologies. Several researchers have tested the effect of heater surface orientation on boiling heat transfer. Notably, Nishikawa et al[160] studied pool boiling of water on a copper surface varying the angle of inclination from 90 degrees to -85 degrees. For low heat fluxes, decreasing the angle of inclination from 90 to -85 degrees enhanced boiling, resulting in a lower wall temperature for a given heat flux. For angles between 90 and -30 degrees, the bubbles swept along the heated surface, agitating and disrupting the superheated liquid layer, causing better mixing with the bulk fluid, which reduced the wall temperature. For angles between -60 and -85, heat transfer was augmented by the evaporation of a thin liquid film trapped between the elongated bubbles and the surface even though there was not much bubble agitation. Nishikawa et al, measured no effect of orientation on heat transfer on higher heat fluxes, and they attributed this observation to the vigorous effusion of vapor promoting efficient mixing with the bulk liquid at all orientations.

In his studies on pool boiling of Freon-11 on a copper surface for angles between 90 and -60 degrees, Chen[161] observed an enhancement similar to that reported by Nishikawa et al for low heat fluxes but, unlike Nishikawa et al., he found the same trend to persist at high heat fluxes. By combining a balance of the surface tension and buoyancy forces on a growing bubble with the thermodynamic equilibrium criterion

for the wall superheat required to grow a bubble from a cavity, Chen showed that the wall superheat decreased as the angle increased between 0 and 90 degree. For angles between 0 and -60 degrees, Chen measured a continued decreased in ΔT_w, which he attributed to bubble agitation of the superheated liquid layer as the bubble moved along the surface and to the premature shearing of growing bubbles by other moving bubbles. When the surfaces was rotated past -60 degrees, the bubbles no longer migrated away from the surface, thus, inhibiting mixing and the replenishing of liquid to the surface, which increased the wall temperature.

Pool-boiling critical heat flux of water on small plates: Effects of surface orientation and size are investigated by Soo Hyung Yang, Won-Pil Baek, and Soon Heung Chang.[162] They systematically performed two types of experiments: the first-phase experiment to clarify the CHF behavior at near the horizontal downward-facing position and the second-phase experiment to find out the general CHF behavior for overall inclination angles. The first- and second-phase experiment were performed for the inclination angles from −90° (horizontally downward position) to −40° using two plate-type test sections (20×200 mm and 25×200 mm) submerged in a pool of saturated water and for overall inclination angles from −90° to 90° using two plate-type test sections (30×150 mm and 40×150 mm) submerged in a slightly subcooled water pool, respectively. The CHF generally decreases as its inclination approaches to −90°, but there is a transition angle, at which the rate of decrease in the CHF suddenly changes. The measured CHF is lower for the wider test section due to the

increased difficulty of bubble escape and this size effect increases as the inclination angle approaches to −90°.

G. Prakash Narayan, K.B. Anoop, G. Sateesh, and Sarit K. Das studied Effect of surface orientation on pool boiling heat transfer of nanoparticle suspensions. Several investigators have found that there is a significant effect of surface orientation on pool boiling performance and mechanisms, when a pure liquid is boiled over tubular heating surfaces. However, there is no similar study reported in literature for pool boiling of nanoparticle suspensions. Based on their study, a smooth tube (average surface roughness 48 nm) of diameter 33 mm and length 170 mm is used at various inclinations (0°, 45° and 90°). Electro-statically stabilized water-based nanoparticle suspensions containing alumina nanoparticles (primary average sizes 47 nm and 150 nm) of concentrations 0.25%, 1% and 2% percent by weight were used. It has been found that there is a significant effect of surface orientation on the heat transfer performance. Horizontal orientation gave maximum heat transfer and the heating surface, when inclined at 45°, gave minimum heat transfer. Further, it was observed that surface–particle interaction and modified bubble motion can explain the behavior.

Victor Rudolph et al[163] studied the influence of droplet orientation on the flow directed organization of nanoparticles in evaporating nanofluid droplets. It is important for the efficiency of foliar applied fertilizers and contamination adhesion to the exterior of buildings. The so called “coffee ring” deposit resulting from the

evaporation of a sessile nanofluid drop on a hydrophilic surface has received much attention in the literature. Deposits forming on hydrophobic surfaces in the pendant drop position (i.e. hanging drop), which are of importance in foliar fertilizer and exterior building contamination, have received much less attention. In their study, the deposit patterns resulting from the evaporation of water droplets containing silica nanoparticles on hydrophobic surfaces orientated in the sessile or pendant configuration are compared. In the case of a sessile drop the well known coffee ring pattern surrounding a thin nanoparticle layer was formed. A deposit consisting of a thin coffee ring surrounding a bump was formed in the pendant position. A mechanism involving flow induced aggregation at the droplet waist, settling, orientation dependant accumulation within the drop and pinning of the contact line is suggested to explain the findings. Differences in the contact area and adhesion of deposits with surface orientation will affect the efficiency and rainfastness of foliar fertilizers and the cleanliness of building exteriors.

So we think the surface orientation of wire heater will have a strong effect on the boiling heat transfer inside nanoemulsion fluid and the effect of subcooling and wire heater orientation on the nanoemulsion fluids are investigated and summarized here. We use the similar test rigs and measure the effect of subcooling and wire heater orientation on the Water-in-PAO and Ethanol-in-PAO nanoemulsion fluids. The results are summarized as follow :

Subcooling effect on nucleate boiling in nanoemulsion fluids:

Subcooling effect on Water-in-PAO nanoemulsion fluids

It has been seen that the Water-in-PAO nanoemulsion fluids, the water concentration affects the boiling curves greatly. It is also well-known that the subcooling affects the nucleate boiling greatly, so here, to better understand the mechanism behind the random occurrence of two boiling curves, more tests are carried out under different liquid subcooling to see the subcooling effect on their boiling phenomena. The same experimental setup is used here except another water bath of 50°C is used for providing different subcooling. The temperature difference of the two thermocouples: one inside the test chamber and the other one inside the water bath are kept less than 0.2K before the test.

The result for the sample of water with volumetric concentration equals to 6.2% is shown in Figure 6.1. It can be seen that the lower subcooling has insignificant effect on the boiling curve before the nucleation happens, but it affects the possibility of turning into the second boiling curve. As shown in the Figure 6.1, that one out of the three tests exhibits the trend of the first boiling curve at 25°C, but they all follow the second curve at 50°C. A similar trend is also observed in all the other samples within $5.3\text{Vol}\% < \omega < 7.8\text{Vol}\%$, where lower subcooling gives a higher chance of following the second boiling curve. Based on our previous results, we may interpret that under lower subcooling, the inner structure is more close to monometric phase, based on our observation which is contradictory to Mitsuhiro's results that said lowering the subcooling will cause the oligomerization to go higher. However, considering boiling

is a complex phenomenon where hydrodynamics, heat transfer, mass transfer, and interfacial phenomena are all needed to be taken into consideration, there are two possible explanations for this divergence: 1. the decrease in radius is associated with an increase in the number of droplets which may agglomerate to certain limit and affect the nucleation process greatly; 2. the occurrence of the second boiling curve is also affected by the fluid's other properties which highly depend upon the temperature such as viscosity, Marangoni effect and each individual bubble growth process and energy transfer. However, more experimental and theoretical studies are still needed to fully understand this phenomenon.

Besides, the CHFs for lower subcooling ones are lower (around 450W/cm^2 for 50^{o}C compared to 560W/cm^2 at 25^{o}C) in either 1st or 2nd boiling curve as shown in Figure 7.1. Similar results are also observed in all the other samples tested which are consistent with previous research as well.

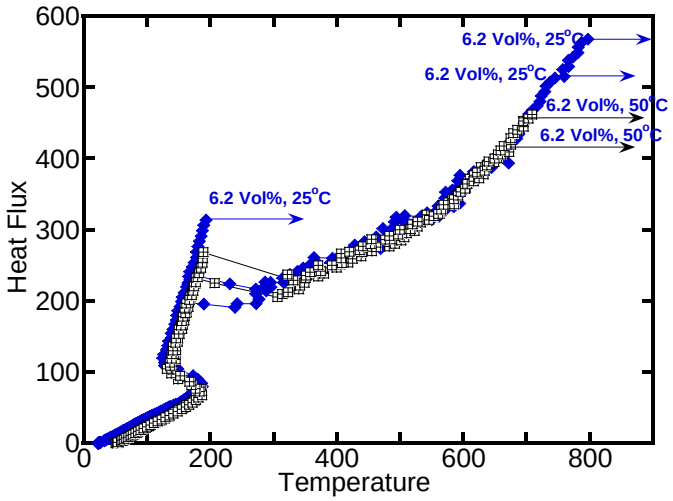

Figure 6.1. Pool boiling curves for Water-in- PAO nanoemulsion fluid of water 6.2 Vol% at two different liquid temperatures: 25^{o}C and 50^{o}C. The arrows in the figure represent where the burn out of wire occurs.

Subcooling effect on Ethanol-in-PAO nanoemulsion fluids

It has been seen that the Water-in-PAO nanoemulsion fluids, the subcooling can affect the boiling curves a lot. So here same test rig and procedure is used for Ethanol-in-PAO nanoemulsion fluids. The same experimental setup is used here except another water bath of 40°C and 60°C is used for providing different subcooling. The temperature difference of the two thermocouples is also kept less than 0.2 K before the test.

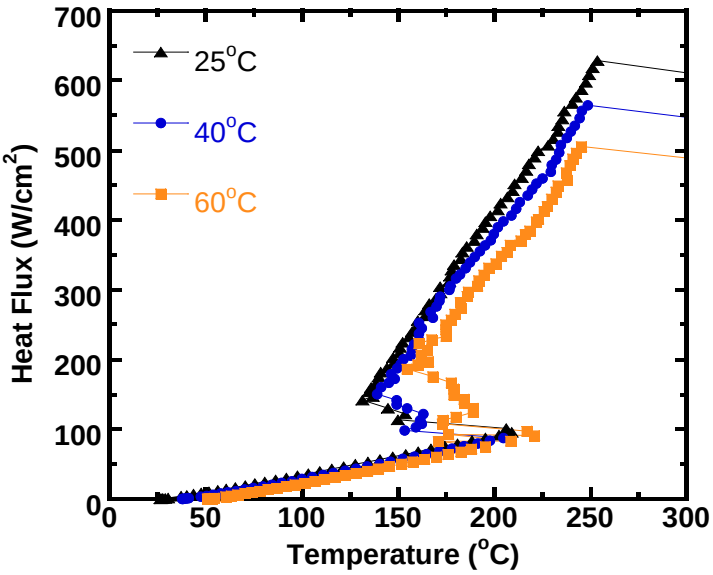

Figure 6.2. Pool boiling curves for Ethanol in PAO nanoemulsion fluid

It can be seen clearly in Fig. 6.2 that the three different symbols of different colors represent the nucleate boiling curve for the same Ethanol-in-PAO nanoemulsion fluids under different subcooling degrees. The black triangle represents the pool boiling curve of the Ethanol-in-PAO nanoemulsion at 20°C while the blue circle is the boiling curve at 40°C and the orange square is the one at 60°C. So here the increase of nanoemulsion fluid temperature or decrease of subcooling gradually shift

the boiling curve to the higher temperature side, which means it reduces the boiling heat transfer coefficient significantly. On the other hand, the heater temperature needed for the incipience of boiling doesn't change too much here which confirms that the nucleate embryo here is the ethanol nanodroplets, which was not sensitive to the temperature variation inside Ethanol-in-PAO nanoemulsion fluids while gas-dissolved bubble nucleation mechanism discovered a strong dependence upon the subcooling degree.

Heater orientation effect on nucleate boiling inside nanoemulsion fluids

Heater orientation on Water-in-PAO nanoemulsion fluids

It has been seen that the Water-in-PAO nanoemulsion fluids, the water concentration, and subcooling can affect the boiling curves greatly. Based on others' finding that the heater orientation can affect the bubble dynamics and heat transfer on heater surface, here the following test is carried out to investigate the effect of heater orientation on the nucleation inside the Water-in-PAO and Ethanol-in-PAO nanoemulsion fluids with same surfactant to eliminate the effect of surfactant on boiling.

Three different wire inclination angles (relative to horizontal): 0 degree, 15 degree and 30 degree of wire heater are used to investigate its effect on the nanoemuslion fluids. The result is shown in Figure 6.3 for 6.2 Vol% Water-in-PAO nanoemulsion fluids that the inclination angle has negligible effect on the boiling curve before nucleation, but it affects the chance of entering the second boiling curve which also

confirms with our previous findings that the inner structure inside have a strong effect on which boiling trend to follow. Based on the assumption of the microstructure inside the Water-in-PAO nanoemulsion fluids, the effect of the inclination angle can be less apparent for the those with oligomers structure inside compared with monomer ones because these large monomeric water droplets vaporized on the wire heater can quickly leave the wire at a large inclined angle which will lower the chance of following the second curve.

The three angles tested here are zero degree (horizontal), 15 degree and 30 degree. The tested samples are of water volume concentration between 5.3% and 8.6% because that is the concentration range where the boiling curves of the nanoemulsion fluids start to vary. It is shown in the figure 6.3 that the inclination angle has little effect on the boiling curve before nucleation happens, but it affects the chance of falling into the second boiling curve. Each inclination angle has been tested three times, and the times of falling into first curve increases from 1 to 2 and to 3 for inclination increase from 0 degree to 30 degree as shown in Figure 6.3. The higher inclination angle (from 0 degree to 30 degree), the higher the chance of being in first curve is which is consistent with our prediction. For all the other samples tested of 5.3 Vol% to 7.8 Vol% water loading, they all follow the similar trend. However, the effect of orientation angles on CHF is not obvious and is also strongly affected by falling into different boiling curves. So the inner structure can explain the phenomenon at room temperature.

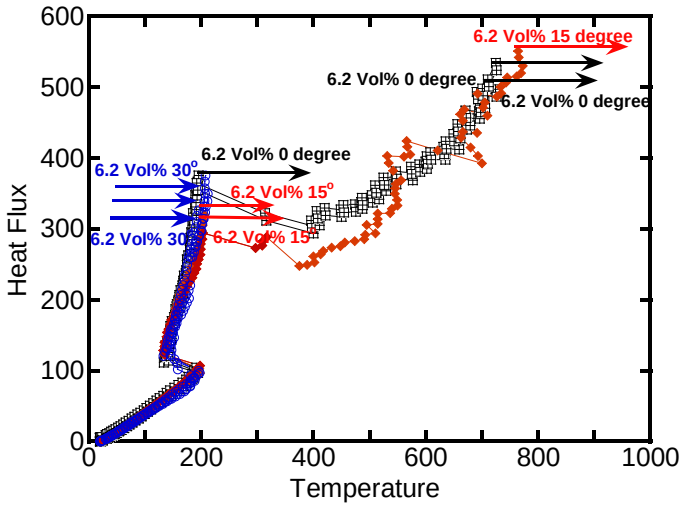

Figure 6.3. Pool boiling curves for Water in PAO nanoemulsion fluid of water 6.2 Vol% at three different wire inclination angles: 0 degree, 15 degree and 30 degree at room temperature. The arrows in the figure represent where the burn out of wire occurs.

Heater incline angle on Ethanol-in-PAO nanoemulsion fluids

It has been seen that in the Water-in-PAO nanoemulsion fluids, the incline angle of wire heater can affect the possibility of following two different boiling curves, but it does not strongly affect the CHF. So, here the effect of the wire incline angle is further verified using Ethanol-in-PAO nanoemulsion fluids.

The Ethanol-in-PAO nanoemulsion fluids with the same concentration are tested here using a similar testing rig as the Water-in-PAO nanoemulsion fluids.

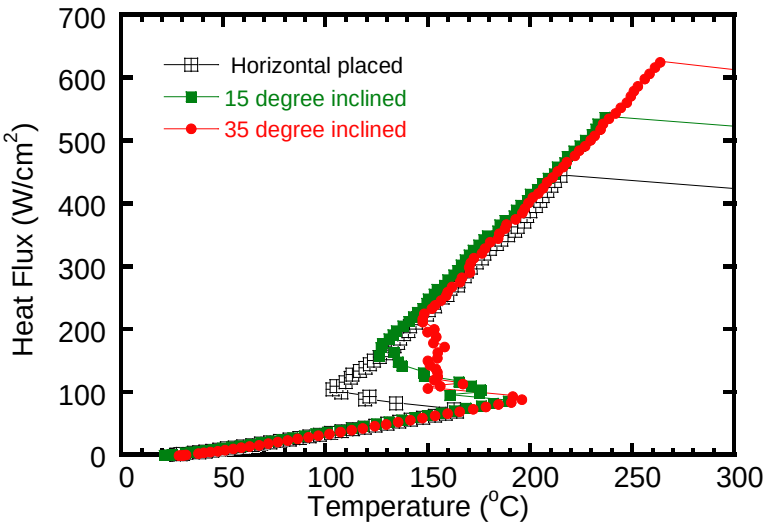

Figure 6.4. Pool boiling curves for Ethanol-in-PAO nanoemulsion fluid at three different wire inclination angles: 0 degree, 15 degree and 30 degree at room temperature. The arrows in the figure represent where the burn out of wire occurs.

It can be seen here that the change of incline angle strongly affect the boiling curve after the nucleation happens. The large inclination angle might affect the bubble dynamics on the wire heater, which can be seen from the difference on the nucleation boiling part right after incipience of boiling. However, the overall nucleate boiling heat transfer coefficient is kept the same for all three incline angles, while the CHF is greatly affected as well. As the ultra-high melting temperature of platinum and the ultra-thin diameter of the platinum wire, it makes the maximum sustainable temperature of the wire subject to the bubble number and movement on the wire. The larger incline angle might give an easier get-away of the bubbles formed on wire which gives a higher maximum sustainable temperature of the wire and thus higher CHF.

Effect of base liquid on nanoemulsion fluids

Introduction

In previous chapters, we have investigated the effect of subcooling and inclination of wire heater on the nucleate boiling heat transfer inside nanoemulsion fluids and their boiling heat transfer characteristics. To systematically understand the boiling mechanism inside these complex three component colloid system, different base fluids are used to form the nanoemulsion fluids and their boiling heat transfer properties are investigated using the methods introduced before.

PAO, as one of the most commonly used heat transfer fluids, was used to make nanoemulsion fluids; three groups of PAO based nanoemulsion fluids have been tested, and they have shown a greatly enhanced heat transfer capability. So, two different base fluids with different boiling points are tested here:

The different properties of the three base fluids are summarized as follow:

Table 6.1: Comparison of different base fluids

Base Fluids	**Molecular formula**	**Appearance**	**Density**	**Boiling point (oC)**	**Specific heat capacity**	**Latent heat**
Hexadecane	$C_{16}H_{34}$	Colorless liquid	773 kg/m^3	281	499.72J/k/mol	454 kJ/mol
Octane	C_8H_{18}	Colorless liquid	703kg/m^3	125	256 J/k/mol	250kJ/mol
PAO	$C_{10}H_{20}$	Colorless liquid	795kg/m^3	223	602 J/k/mol	203kJ/mol

Ethanol-in-Hexadecane nanoemulsion fluids

First, the effect of non-ionic surfactant concentration on the boiling properties are investigated and they are summarized as follow: we used eight concentrations of surfactant-in-Hexadecane mixture here: 15.4%, 8.3%, 1.8% and 0% surfactant inside base Hexadecane fluid to form the nanoemulsion fluids.

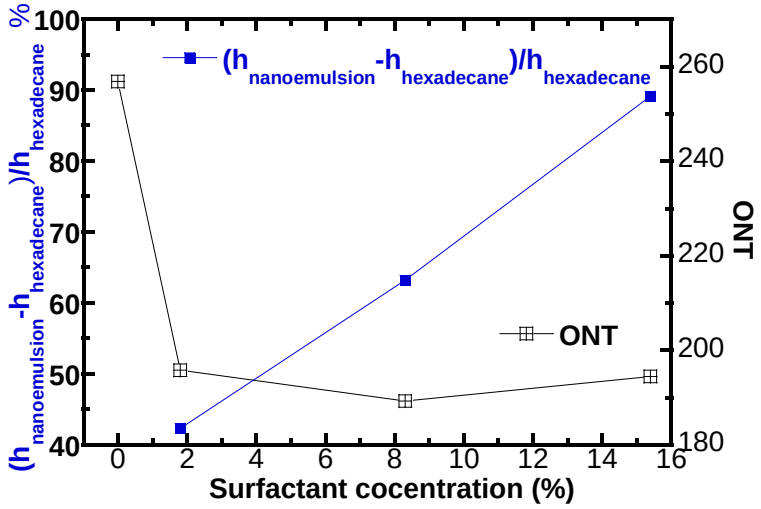

Fig. 6.5 ONT and heat transfer coefficient enhancement for ethanol-in-Hexadecane nanoemulsion fluids at different surfactant concentrations

The comparison of ONTs and relative increase of nucleate heat transfer coefficient is compared above in Figure 6.5; on the left Y axis, the nucleate heat transfer coefficient enhancement compared with pure hexadecane increases almost linearly with higher surfactant concentration, with a maximum around 90% enhancement; on the right Y axis, the figure shows the ONTs variation with surfactant concentration— that it greatly decreased from around 260^{o}C to below 200^{o}C upon the addition of 2% surfactant inside and that it kept almost constant with some fluctuation when surfactant concentration is further increased. It is similar to the trend in the

surfactant/PAO mixtures, only here in surfactant/Hexadecane the trend is more linear which might be due to the longer C-C chain inside hexadecane compared to the PAO.

Ethanol-in-Octane Nanoemulsion fluids

Similar to the Hexadecane and PAO tested before, octane, the one of the lowest boiling point, is used as another base solvent fluid to form nanoemulsion fluids and to compare with the previous two base fluids. However, the ethanol is partially soluble inside octane, so, inner structure can be different from previous nanoemulsion fluids prepared.

1. Ethanol solubility in octane effect:

As ethanol is partially soluble in octane, here the pure octane, octane and ethanol mixture, and ethanol/octane mixture with surfactant inside are tested, and the results are summarized as follow:

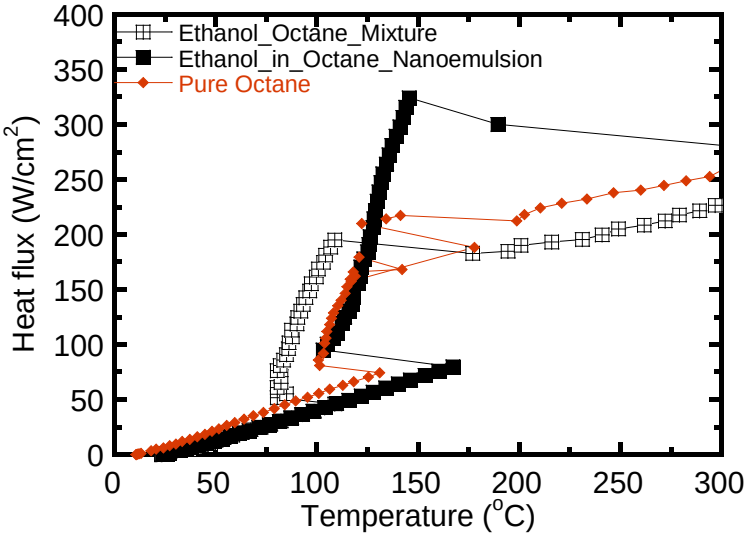

Fig 6.6 Boiling curves for Octane/Ethanol mixture

It can be seen here that 1. the soluble ethanol inside Octane shift the boiling curve to the left compared to pure Octane fluid which greatly decrease the ONT but keeps the CHF almost the same 2. the addition of surfactant inside the mixture of ethanol and octane actually shifts the boiling curve to the right which means the degradation of nucleate boiling heat transfer capability, but it can greatly enhance the critical heat flux with an elevated ONT too. So the addition of surfactant inside can change the inner structure of octane/ethanol mixture to nanodroplets as in nanoemulsion fluids, and their nucleating boiling curve also show the change.

Summary

So far the three base fluids: PAO, Hexadecane, and Octane have been tested here and their boiling heat transfer properties of their based nanoemulsion fluids.

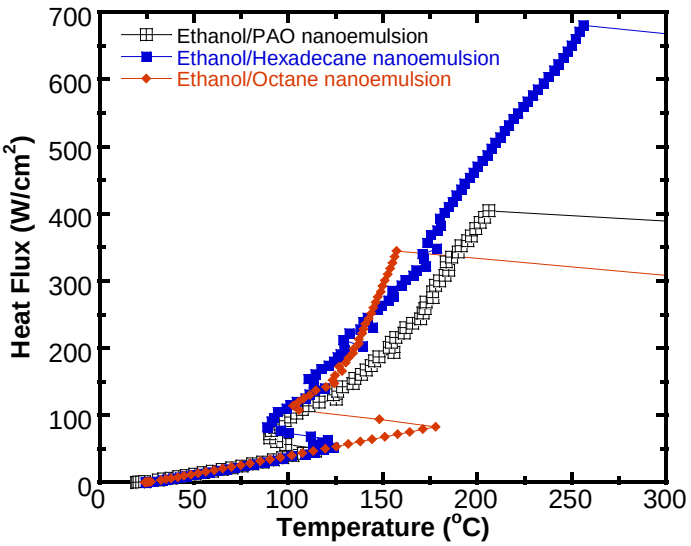

Fig. 6.7 Boiling curves for Ethanol-in-Octane, Ethanol-in-hexadecane and Ethanol-in-PAO nanoemulsion fluids

Three Ethanol-in-Oil nanoemulsion fluids we tested before using same surfactant are compared here in Fig. 6.7. It can be seen that the three boiling curves are almost the same before the incipience of boiling and after the initiation of boiling; the three boiling curves start to be different which might due to the effect of different properties of base fluids and the inner structures because the different chain length of base fluids. Besides, it can also be seen here that the based fluids also have a strong effect on the CHF, where the CHF gradually increases in Octane, PAO, and Hexadecane with longer C-C chains. However, more systematical study is still needed to fully understand the dominating factors inside the different oil based nanoemulsion fluids.

Chapter 7: Bubble Visualization and Modeling

Introduction to bubble visualization methods

Bubble visualization is an important method to help understand the nucleation process within a fluid of unknown properties, especially, for this new nanoemulsion fluid. Here, a high-speed camera (LaVision) is used to visualize the bubble generation and dynamics along the wire heater in the pool-boiling test of pure ethanol and Ethanol-in-PAO nanoemulsion fluids[164].

In general, bubble growth in superheated fluids is of key interest in boiling phenomena, and in particular, flash evaporation. Most of the large amount of research on such bubble growth has been conducted for pure liquids; very little is, therefore, known about bubble growth in superheated solutions with a non-volatile solute. Amongst the small number of papers on bubble growth in superheated binary solutions, Scriven [165, 166] has described the general approach to modeling uniformly-heated spherically-symmetric bubble growth of both pure liquids and binary mixtures, and has derived approximate asymptotic solutions in the heat and mass-transfer controlled regime.

The past research shows that bubble growth in superheated liquids can be characterized as progressing liquids in three consecutive regimes : at first, just when the bubble has nucleated (with radius just larger than the critical), surface tension is

dominant, impeding significant growth for a certain “delay period”. After the nucleus grew somewhat, say doubled its diameter, inertia forces become dominant and the bubble grows primarily due to the difference between the vapor pressure inside the bubble (p_v) and the exterior pressure (p_{inf}). During that period bubble growth is a linear function of time R~t. As the bubble grows further and its wall temperature consequently drops, causing an increased temperature difference between the surrounding liquid and the bubble wall, its growth rate becomes dominated by heat transfer from the surrounding liquid, which causes addition of vapor to the bubble by evaporation at the interface. During that period, the bubble growth is characterized by R~t ^{½}.

Mikic et al[167] have developed a simple general equation for calculating bubble growth rates in pure liquids, starting with a bubble radius of zero, only in the inertia and heat transfer controlled regimes, via.

$$R^+ = \frac{2}{3}[(t^+ + 1)^{\frac{3}{2}} - (t^+)^{\frac{3}{2}} - 1] \qquad (7.1)$$

Where $R^+ = \frac{A^+}{(B^+)^2} R$

$$A^+ = (\frac{2}{3}\frac{h_{fg}\rho_{v\Delta T_s}}{\rho_l T_s})^{1/2}$$

$$B^+ = (\frac{12}{3}\alpha_1)^{1/2}\frac{c_1\rho_1\Delta T}{h_{fg}\rho_v}$$

$$t^+ = (\frac{A^+}{B^+})^2 t$$

The properties of the vapor and liquid in the above equations are based on the saturation temperature (T_s) of the liquid, which corresponds to the pressure (P_{inf}) in the liquid from the bubble, viz

$$p_\infty = (P)_T \qquad (7.2)$$

And the superheat (ΔT) is defined as

$$\Delta T = T_\infty - T_s$$

In the development of this bubble-growth, Mikic et al have assumed that the relationship between the vapor pressure and temperature can be expressed by the linearzied Clasusis-Clapeyron equation, and that the vapor density is constant. Therefore these assumptions may lead to large errors for large initial superheats when the vapor density changes during the process significantly. They have also modified the bubble growth equation to correct this deficiency by using a more realistic dependence of vapor density on temperature.

Unfortunately, getting disparate departure diameter, bubble frequency, and bubble growth correlations to intersect at a single point is near impossible. [98] For a spherical bubble growing in an infinite superheated pool, growth is initially inertia controlled, and bubble radius tends to increase linearly with time. Later, when bubble growth is limited by heat transfer rates, radius tends to increase as the square root of time [168]

For bubble growth near a heated wall, however, consider the Mikic and Rohsenow [169] bubble growth correlation.

$$r(\tau) = \frac{2Ja\sqrt{3\pi\alpha_f \tau}}{\pi}\left\{1 - \frac{T_w - T_\infty}{\Delta T_{sat}}\left[\sqrt{1 + \frac{\tau_w}{\tau}} - \sqrt{\frac{\tau_w}{\tau}}\right]\right\} \quad (7.3)$$

Where

$$Ja = \frac{C_p \rho_f \Delta T_{sat}}{\rho_g h_{fg}}$$

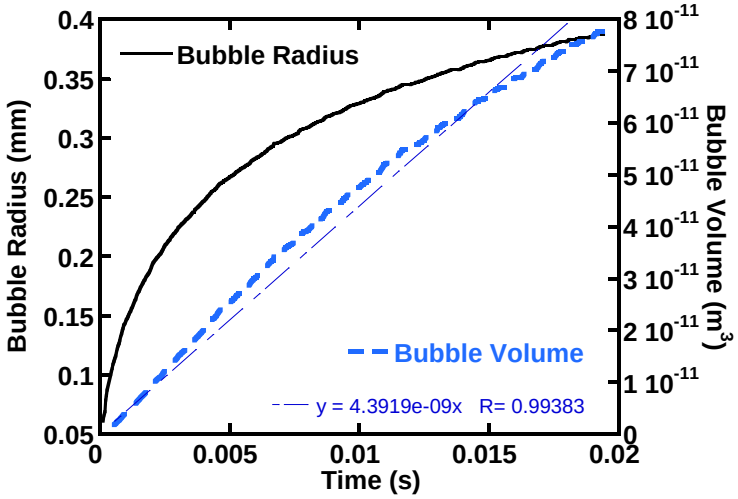

Figure 7.1 Bubble growth rare predicted by Mikic and Rohsenow correlation

Bubble dynamics inside Ethanol-in-PAO nanoemulsion fluids

For the Ethanol-in-PAO nanoemulsion fluids, the best composition of ethanol-in-PAO nanoemulsion is used here. The bubble growth process on the wire is recorded and analyzed, the bubble diameter growth with time until departure is summarized and compared below. Three different wire temperature are compared here: 1. Low flux: 135.79°C with 149.42W/cm^2; 2. High flux: 180.12°C with 289.75W/cm^2.

Three bubbles' growth curves are plotted for each heat flux and shown below:

The bubble dynamics at low heat flux

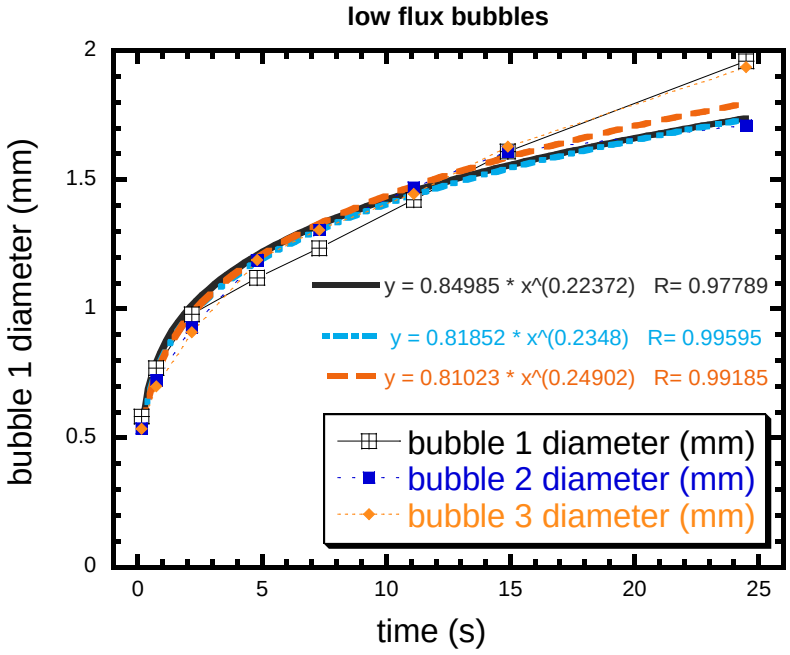

Fig. 7.2 Bubble dynamics with time in ethanol-in-PAO nanoemulsion fluids

A growth curve was obtained by measuring the diameter of an individual bubble from incipience through sliding. All the bubble growth data reported in this work lie in the diffusion controlled regime; the inertial controlled regime lasts for a very short period and is shorter than the time period between successive frames obtained with high speed imaging. The experimental growth rates may be approximated by a power law curve fit:

$$d(t) = Kt^n \qquad (7.4)$$

Where d(t) is the diameter of the bubble, t denotes time, K and n are empirical constants. Because of the stochastic nature of the flow and thermal variations, a set of

three growth curves were measured at various points on the wire heater, and the constants K and n were averaged to estimate the mean growth curve at this condition. From the table it is observed that the growth data fit a power law ranging from about t1/4 to t 1/5 which is very different from previous experiment results.

Table 7.1: High speed camera pictures of bubble dynamics

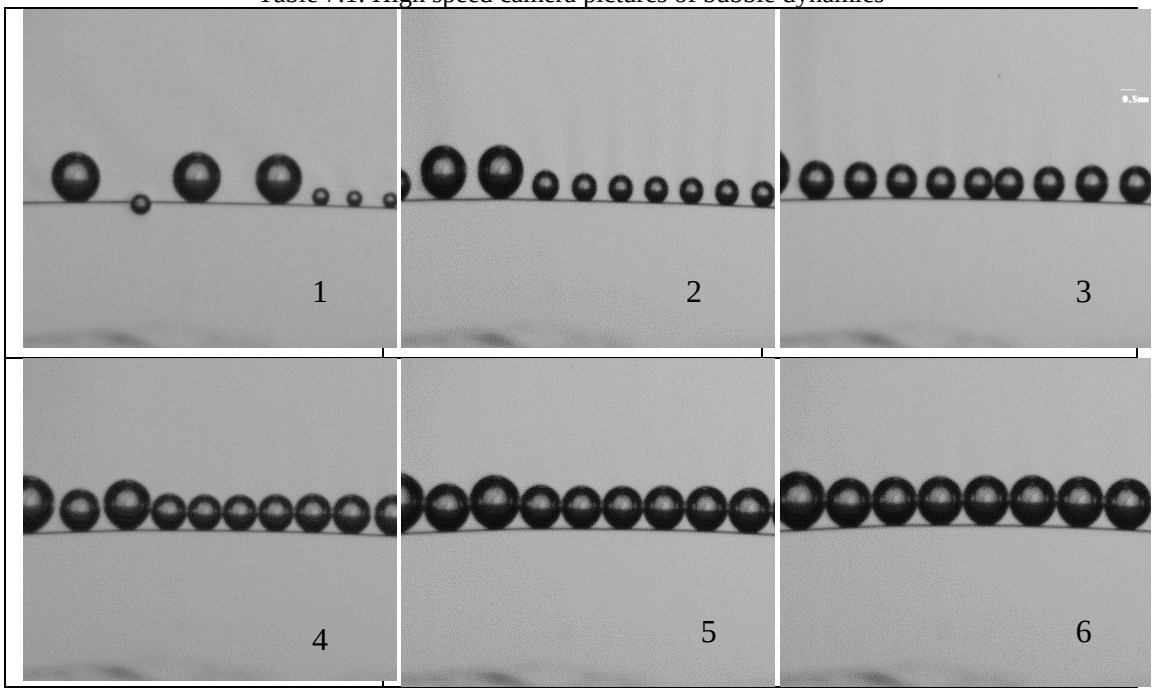

So here in the Table 7.1 above shows the bubble dynamics inside the ethanol-in-PAO nanoemulsion fluids with time under low heat flux. From the top left corner to the right corner, several bubbles start to form on the right side of the wire and they gradually grow in size, continuously moving to the left. In picture.4, the new grown bubble takes the main section of the wire heater and grows to be of a uniform size. From picture. 5 to 6, they keep growing in size and moving to the left and eventually, reach critical size and leave the wire together after picture. 6.

The bubble dynamics at high heat flux

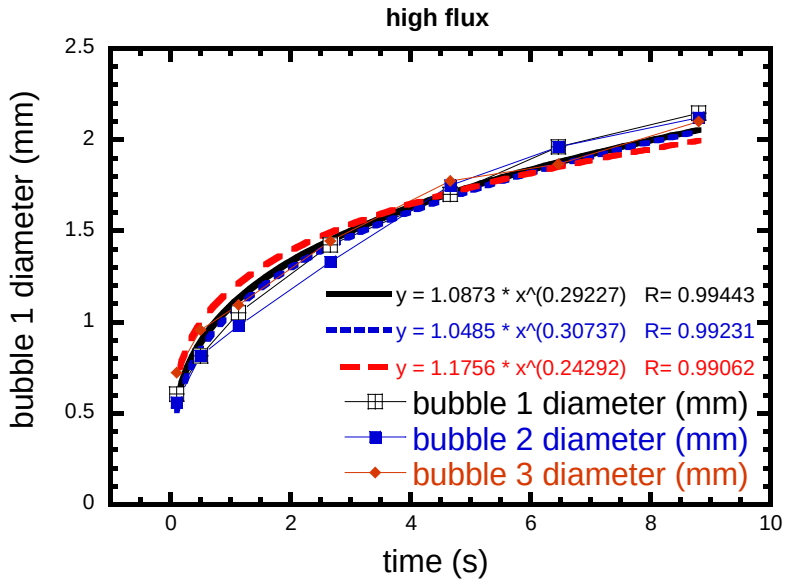

Figure 7.3 Bubble dynamics with time in ethanol-in-PAO nanoemulsion fluids

A growth curve was obtained by measuring the diameter of an individual bubble from incipience through sliding. All the bubble growth data reported in this work lie in the diffusion controlled regime; the inertial controlled regime lasts for a very short period and is shorter than the time period between successive frames obtained with high speed imaging. From the table it is observed that the growth data fit a power law ranging from about t $^{1/3}$ to t ¼, which is very different from previous experiment results.

Table 7.2: High speed camera pictures of bubble dynamics

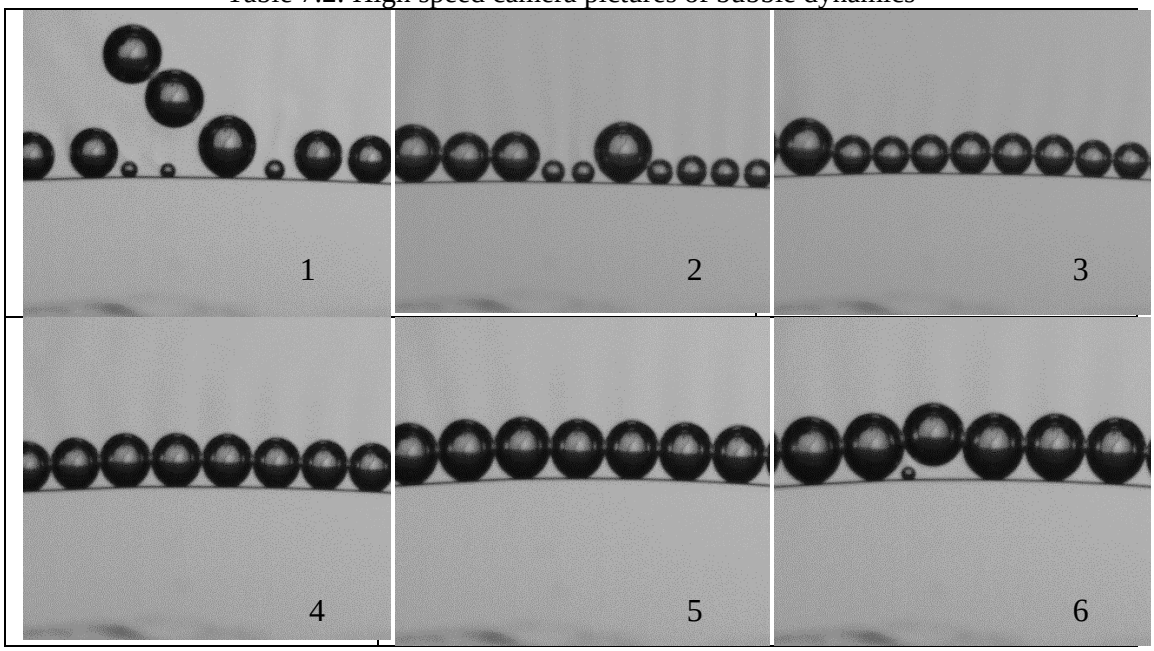

Bubble dynamics inside Ethanol-in-PAO nanoemulsion fluids

The bubble dynamics at low heat flux

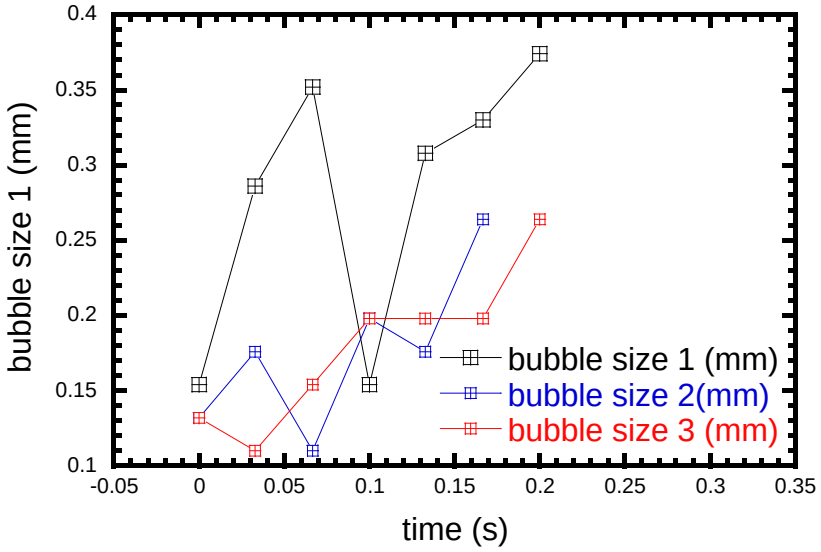

Figure 7.4 Bubble dynamics with time in pure ethanol

A growth curve was obtained by measuring the diameter of an individual bubble from incipience through sliding. All the bubble growth data reported in this work lie in the diffusion controlled regime; the inertial controlled regime lasts for a very short period and is shorter than the time period between successive frames obtained with high speed imaging. The dependence of bubble size is less apparent here partially due to the much smaller departure droplet size and much shorter bubble time on wire/faster bubble departure frequency.

Table 7.3: High speed camera pictures of bubble dynamics inside ethanol

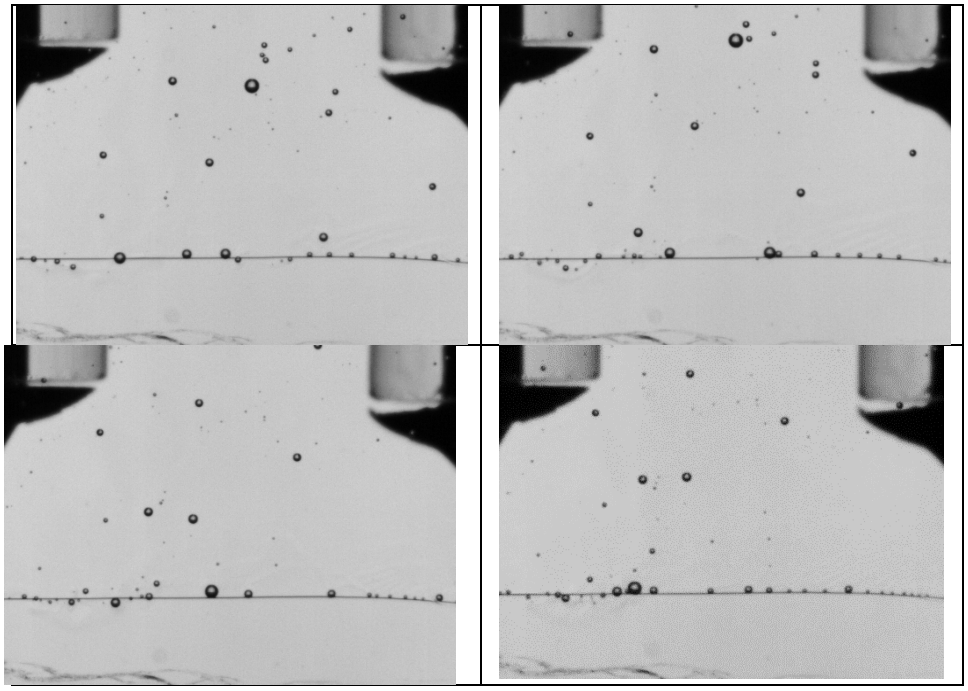

It is shown more apparently here that the inner droplet size of pure ethanol is much smaller and bubble morphology on wire heater is quite different from Ethanol-in-PAO nanoemulsion fluids, which is partially due to the much smaller viscosity inside and the interaction between the ethanol vapor and outer base fluid. A similar

phenomenon is also observed in other ethanol fluids and other PAO based nanoemulsion fluids.

Chapter 8: FC72 and FC40 binary mixture

Introduction

Fluorocarbon (FC) fluids has been extensively studied as a promising fluid for electronic cooling due to its low boiling point and dielectric properties. Pool boiling heat transfer and critical heat flux in FC based mixtures has been of interest for the last four decades. The need for higher pool boiling CHF in electronic cooling applications has led to the use of mixtures of dielectric fluids. Normington et al[170] conducted several experiments with the binary liquid mixtures of the perfluoropolyether liquids. The most noticeable change was a dramatic decrease in the temperature overshoot at the incipience when using mixtures compared to single, pure liquids. The boiling curve shifted towards the right with increasing concentrations of the higher boiling point liquid and the CHF was observed to increase as much as 60%, with increasing subcooling (50K). He also investigated the application of dielectric binary mixtures in electronic cooling with PPGA packages. Two perfluoropolyether liquids were mixed in different volumetric fractions. The observed deterioration in the heat transfer coefficient was similar to the hydrocarbon mixtures. He did not observe a shift in the boiling curve, although two components had saturation temperatures of 81^{o}C and 110^{o}C, respectively, and CHF values were enhanced when the concentration of the higher boiling point liquid was increased.

Recently, M. Arik and Bar-Cohen [171] have extended the available data on mixture CHF enhancement, as well as pool boiling, on polished silicon surfaces to FC72/FC40 mixture ratios of 10%, 15% and 20% of FC=40 by weight, a pressure range of between 1 and 3 atm, and fluid temperature from 22 to 45^{o}C, leading to high subcooling conditions. It is found that peak heat flux can be increased to as high as 56.8 W/cm^2 compared to 25.2W/cm^2 for pure FC72 at 3atm and 22^{o}C. It is believed that the increase in the mixture latent heat of evaporation and surface tension, accompanying the depletion of the lower boiling point fluid in the wall region plays the major role in enhancing the critical heat flux for binary mixtures.

Pool Boiling of the mixture

As before, the effect of FC40 concentration on pool boiling heat transfer inside FC72/FC40 mixture are first investigated, here the following concentrations of FC40 are added 0%, 2. 5% by weight, 10% by weight, and 20% by weight FC40 inside FC72.

First, the pool boiling test of FC40/FC72 mixtures at different mass concentrations are tested and shown below at room temperature (25^{o}C):

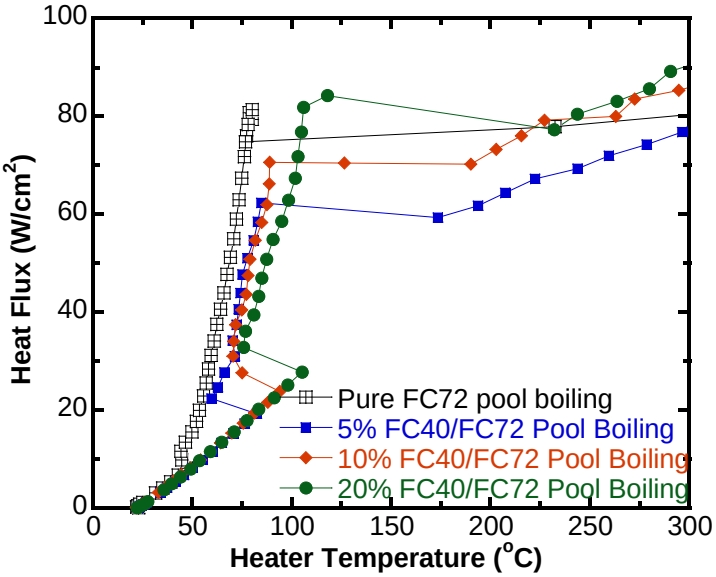

Figure 8.1 Pool Boiling curves for FC40/FC72 mixture at different FC40 mass concentration at 25 degree fluid temperature

It can be seen that the addition of FC40, which has a higher ONT, shifts the boiling curve of the mixture to the right, which gives a higher superheat temperature needed for nucleation and a lower nucleate heat transfer coefficient at the same heater temperature. Another interesting thing here is that the CHF first decreased with higher FC40 loading and gradually increased with higher FC40 loading.

Flow Boiling of the mixture

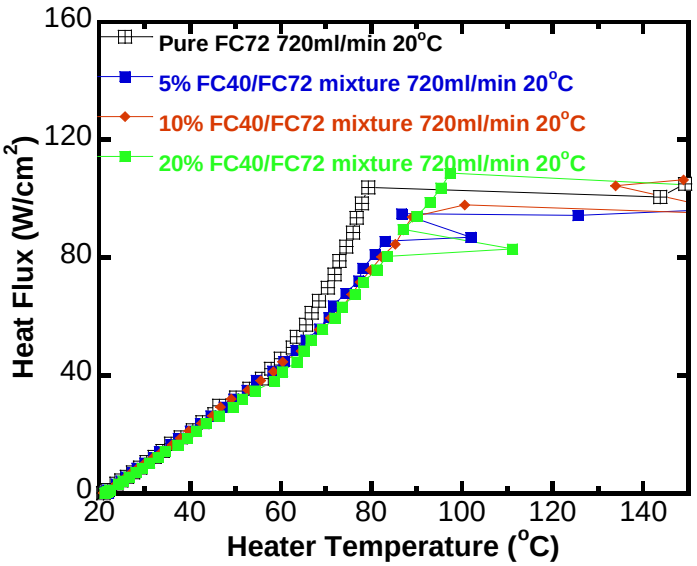

Figure 8.2 Flow Boiling curves for FC40/FC72 mixture at different FC40 mass concentration at 25 degree fluid temperature

It can be seen here that the addition of FC40 shifts the boiling curve of the mixture to the right especially after the nucleation starts, which gives a lower nucleate heat transfer coefficient while the ONT is not affected due to the flow motion around the wire heater. Another interesting thing here is that the CHF doesn't vary much with higher FC40 loading which is quite different from the pool boiling results.

Subcooling effect on the mixture

Also, the effect of subcooling is tested, and their effect on pool boiling of 10% FC40/FC72 mixture is tested under three fluid temperature 0, 25 and 40 degrees:

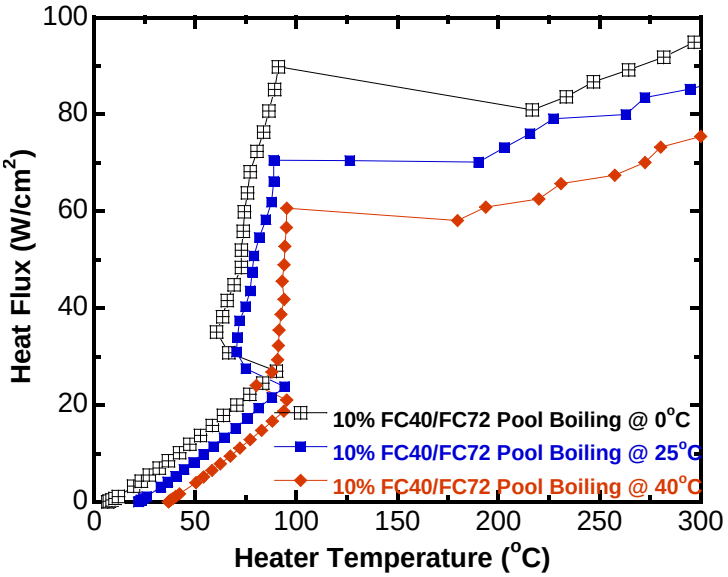

Figure 8.3 Pool Boiling curves for FC40/FC72 mixture at 10% FC40 mass concentration at different fluid temperatures

It can be seen that for 10% mass fraction of FC40/FC72 mixture, the subcooling has a similar effect on the nucleation boiling curves: the boiling curves shift to the right with a low subcooling degree which gives a lower CHF with lower subcooling degree while the ONTs are not affect much. It also agrees well with others findings.

Similarly, the subcooling effect on the flow boiling heat transfer inside 10%FC40/FC72 mixture is also compared as below:

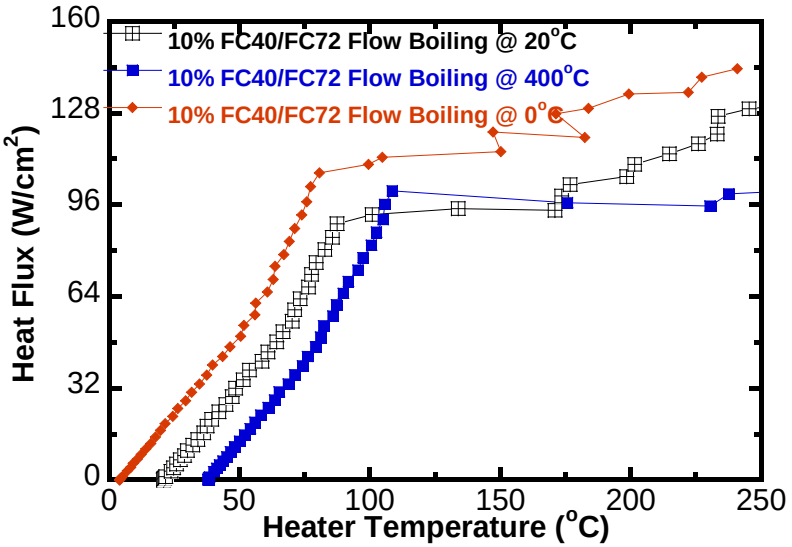

Figure 8.4 Pool Boiling curves for FC40/FC72 mixture at 10% FC40 mass concentration at different fluid temperatures

It can also be seen here that, very similar to the trend observed in pool boiling under different subcooling conditions, here the flow boiling curves shifts to the right with the decreasing of subcooling degree and the boiling curves are parallel to each other. The flow motion seems to have a stronger influence on the CHF so the CHF fluctuates with different subcooling temperature.

Flow speed effect on the mixture

Previously, we have tested the pool boiling heat transfer properties of FC40/FC72 mixtures at different FC40 concentrations and subcooling degrees, and the results agree well with others studies. Now, we are focusing on the study of the flow motion inside the FC40/FC72 mixture. To make the comparison more consistent, all the FC40/FC72 mixtures tested here are kept at room temperature with flow speed varying from 700ml/min to 1000ml/min, and their results are summarized as follow:

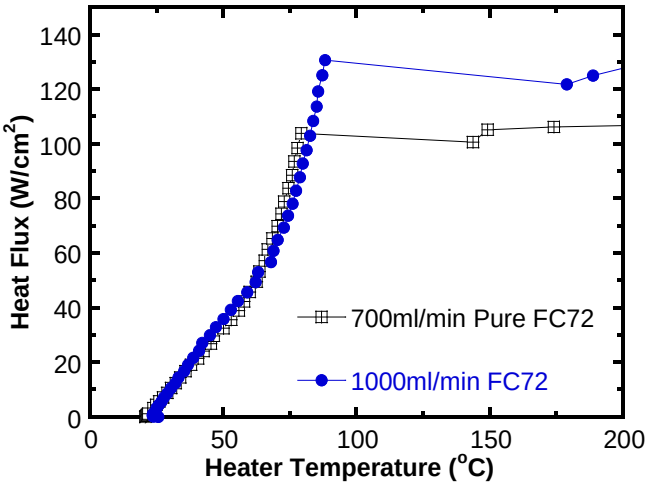

Figure 8.5 Pool Boiling curves for pure FC72 mixture at different flow speeds

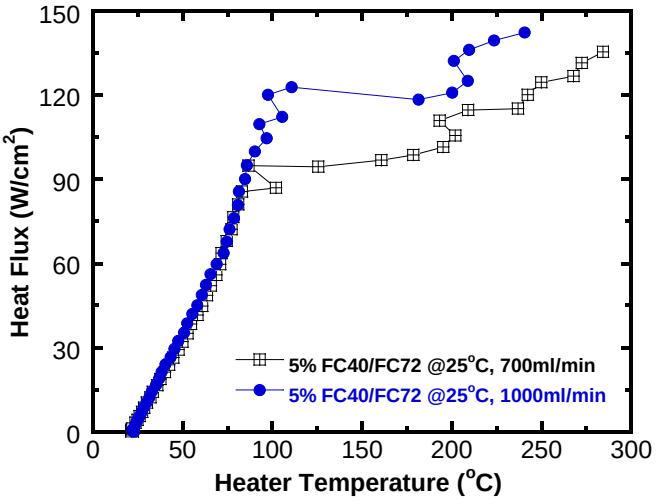

Figure 8.6 Pool Boiling curves for 5% FC40/FC72 mixture at different flow speeds

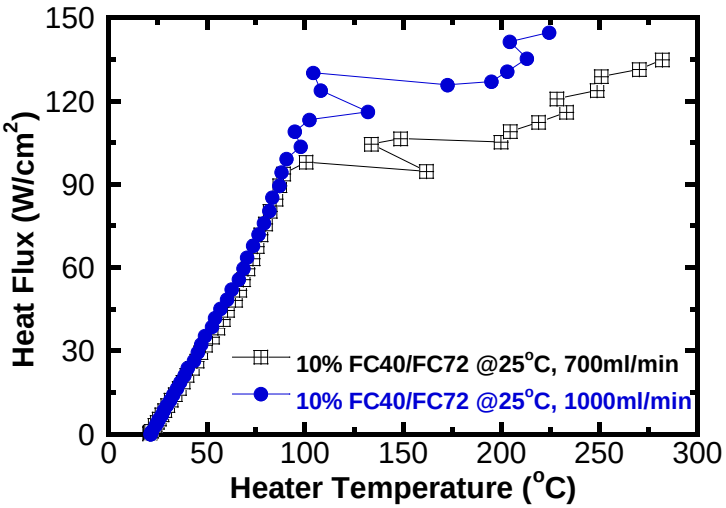

Figure 8.7 Pool Boiling curves for 10% FC40/FC72 mixture at different fluid temperatures

So, the Figure 8.5 to 8.7 as shown above, are the pool boiling curves of FC40 loading inside FC72 with 0%, 5% and 10% FC40 inside under different flow speeds. It can be seen that the addition of FC40 has a negligible effect on flow boiling heat transfer and the CHFs.

Chapter 9: Numerical modeling of thermal transport in nanoemulsion fluids

Introduction

First, the thermal transport properties, including the thermal conductivity and viscosity are theoretically modeled to give an in-depth understanding of the properties of the nanoemulsion fluids. Since investigation of the transport properties of colloidal systems had been carried out since Maxwell's pioneer work and for the simplicity of the modeling process, the nanoemulsion fluids are assumed to be composed of a continuous phase, that is, the base heat transfer fluid, and one or more discontinuous phases, that is, dispersed liquid nanodroplets. It can be predicted that the properties of nanoemulsion fluids will depend on the intrinsic properties of the base fluids and nanodroplets. In addition, the details of the microstructures of nanoemulsion fluids, including the geometry, the dimensions, the volumetric fraction, the distribution and motion of nanodroplets, the properties of the interfaces between base fluids and nanodroplets, etc.

Thermal conductivity modeling

Effective Medium Theory

Ever since the development of nanofluids, the effective medium theory which includes a wide variety of functions only calculate the thermal conductivity enhancement based on the base fluids and the added nanoparticles and the volumetric fraction of the particle count, without taking into consideration of the size, geometry,

and the distribution and motion of dispersed particles. Similarly, this method can be used to quickly estimate the thermal conductivity of the nanoemulsion fluids we prepared here.

The Maxwell method was first brought forth by Maxwell to investigate the thermal conductivity of liquid suspensions analytically by considering a very dilute suspension containing spherical particles and ignoring the interactions among particles. Later his model was adopted and modified by Hamilton and Crosser (HC model) after taking into consideration the particle geometry; their model has been used for the description of the thermal conductivity enhancement of a dilute suspension of spherical/non-spherical particles in a liquid or solid.

$$\kappa_{eff} / \kappa_0 = \left[\frac{\kappa_p + 2\kappa_0 + 2(\kappa_p - \kappa_0)\varphi}{\kappa_p + 2\kappa_0 - (\kappa_p - \kappa_0)\varphi} \right] \qquad (9.1)$$

Based on this equation, the effective thermal conductivity of nanoemulsion fluids, K_{EMT} thus, depends only on thermal conductivity of matrices/base fluids, thermal conductivity of dispersed nanodroplets, and the volumetric fraction of nanodroplets.

In addition to the shape factor, the interfaces between two materials, i.e., liquid base fluids and solid particles acts as a thermal barrier to the heat flow because of the poor chemical bonding between atoms and/or molecules at the interfaces, and the difference in thermal expansion properties of the different materials. It usually can be neglected for macroscopic objects; however, this is not the case for particles with reduced size. It is therefore important that the interfacial resistance, or Kapitza resistance, R_k, should be included in the calculations in order to more accurately predict the temperature distribution, heat flux, and the thermal conductivity of the

liquid suspensions. Interfacial resistance R_k arises from the differences in phonon spectra of the two materials, and subsequently, from the scattering of the phonons at the interfaces. Hasselman and Johnson [170]modified Maxwell's model in order to include a term of the interfacial thermal resistance. The resulting theoretical prediction for the effective thermal conductivity enhancement of the particle-in-liquid colloidal suspensions is given by,

$$K_{EMT} = \frac{K_{droplet}(1+2\Gamma)+5K_{fluid}+2[K_{droplet}(1-\Gamma)-K_{fluid}]\phi}{K_{droplet}(1+2\Gamma)+5K_{fluid}-[K_{droplet}(1-\Gamma)-K_{fluid}]\phi}K_{fluid} \qquad (9.2)$$

Or in another form:

$$\kappa_{EMT}/\kappa_{fluid} = \left[\frac{(\kappa_{droplet}+2\kappa_{fluid})r+2\kappa_{droplet}\kappa_{fluid}/G+2\kappa_{fluid}r+2f((\kappa_{droplet}-\kappa_{fluid})r-2\kappa_{droplet}\kappa_{fluid}/G)}{(\kappa_{droplet}+2\kappa_{fluid})r+2\kappa_{droplet}\kappa_{fluid}/G+2\kappa_{fluid}r-f((\kappa_{droplet}-\kappa_{fluid})r-2\kappa_{droplet}\kappa_{fluid}/G)}\right] \qquad (9.3)$$

In this equation, $\Gamma = \frac{1}{G} = 2R_{bd}K_{fluid}/d_{droplet}$, r is the radius for the dispersed droplet, G is the interfacial thermal conductivity, $d_{droplet}$ is the average nanodroplets diameter, R_{bd} is the interfacial thermal resistance. In the absence of thermal interfacial resistance ($R_{bd} = 0$), the above equation reduces to Maxwell's model.

So here, the Hasselman and Johnson(HJ) model has been used to describe the thermal conductivity enhancement in the water-in-PAO nanoemulsion fluids. The diameter of water nanodroplets is $d_{droplet} \cong 10\,nm$; the thermal conductivity of water is 0.58 W/m.K; the thermal conductivity of PAO is measured by 0.171 W/m.K, i.e., at 25 ^oC The interfacial thermal conductance, G = 600 MW/m^2.K and G = 6GW/m^2.K is used in the calculations and the modeling result have been shown in Figure 9.1.

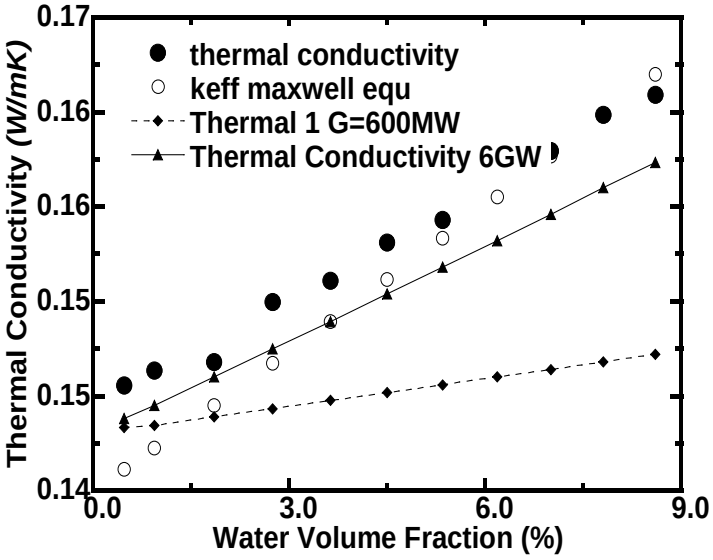

Figure 9.1 Thermal conductivity and numerical simulation data for Water-in-PAO nanoemulsion fluids

As there is no reported G value for this system, the G value is deducted by fitting the curve with experimental data. A minimum of 30MW/m^{2}K for G is needed to make sure the thermal conductivity is increasing with higher ethanol concentration. If the G is increased to 6GW/m^{2}K, it is pretty close to the trend of experimental results and also close to classic Maxwell predictions. The radius variation effect on the thermal conductivity is also verified for both G value and the radius have a minor effect on the thermal conductivity, which will be even weak if the G value is high. So, classic Maxwell equation is able to give good prediction for the correlation of thermal conductivity and water concentration, but still underestimate the absolute value of the nanoemulsion system.

Similarly, the HJ EMT model has been used to describe the thermal conductivity enhancement in the Ethanol-in-PAO nanoemulsion fluids. The diameter of water

nanodroplets is $d_{droplet} \cong 0.9\,nm$; the thermal conductivity of ethanol is 0.171 W/m.K; the thermal conductivity of PAO is measured by 0.143 W/m.K, i.e., at 25 ^{o}C The interfacial thermal conductance, G = 600 MW/m^2.K and G = 6GW/m^2.K is used in the calculations and the modeling result have been shown in Figure 9.2.

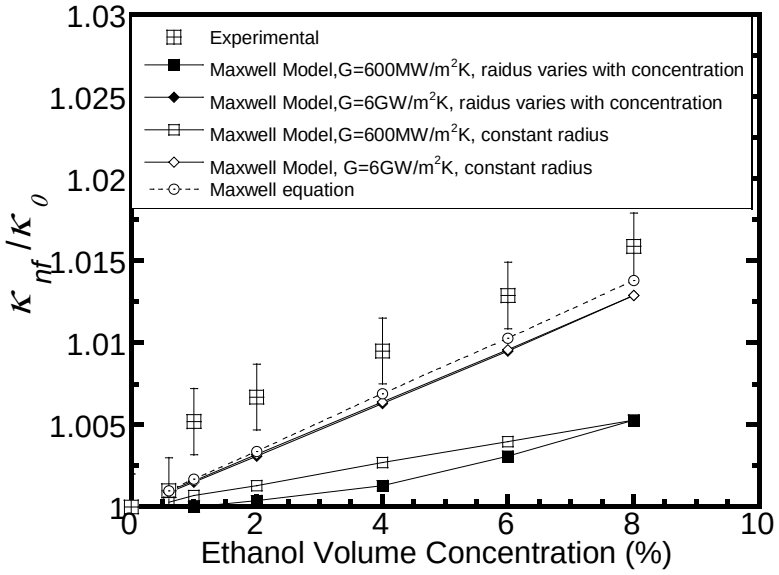

Figure 9.2 Relative thermal conductivity and numerical modeling for Ethanol-in-PAO nanoemulsion fluids

Similarly, the increase of G makes the predicted thermal conductivity value closer to the trend of experimental results. The radius variation effect on the thermal conductivity is also verified that both G value and the radius have a minor effect on the thermal conductivity which will be even weak if the G value is high. Both classic Maxwell equation and HJ EMT models are able to give good prediction for the correlation of thermal conductivity and ethanol concentration, but still underestimate the absolute value of the nanoemulsion system. The larger-than-predicted

conductivity enhancement indicates that there are other mechanisms that contribute to the thermal conductivity enhancement in nanoemulsion fluids.

Brownian motion of Nanodroplets

Based on the previous EMT modeling, it can be seen that the EMT model can't explain the enhancement inside the nanoemulsion fluids that well. So other mechanisms are investigated here.

Back in 2000s, in order to explain the anomalous enhancement in thermal conductivity of nanofluids, Keblinski [172] proposed four possible mechanisms: (1) Brownian Motion of nanoparticles; (2) liquid layering at liquid/particle interface; (3) ballistic nature of heat transport in nanoparticles; (4) nanoparticle clustering in nanofluids. It is believed that micro-convection induced by the Brownian motion of nanoparticles may be one of the main reasons responsible for the increase of nanofluid thermal conductivity. When a particle is immersed in a fluid, it moves randomly due to the interaction between the particle and its surrounding fluid molecules, this random motion is called "Brownian motion". The Brownian motion of large particles is negligibly small and it is not considered in the traditional particulate flow. However, when the size of particle is as small as nanoparticles, the Brownian motion becomes significant. It has been reported that the thermal conductivity enhancement in nanofluids increase substantially with increasing temperature and decreasing particle size, which indicates the contribution of Brownian motion to the thermal conduction in nanofluids.

Conventional EMT models on thermal conductivity of nanofluids are based on an assumption that the heat transports in each phase and between phases are only governed by the diffusion. These models successfully explain the effective thermal conductivity of liquid suspensions containing millimeter or even micrometer sized solid particles. The higher-than-predicted, temperature and size dependent thermal conductivity of nanoemulsion fluids needs discovery of new thermal transport mechanisms of nanoemulsion fluids. Nanoemulsion fluids are homogeneous and are well dispersed systems. Due to the small size of nanodroplets in nanoemulsion fluids, additional energy transport may arise from the Brownian motions induced by stochastic and inter-particle interacting forces. It is already known that the velocity of nanoparticles is inversely proportional to the square of the particle diameter, and with reducing particle size, the drift velocity of nanoparticles increases rapidly.

In order to take that into consideration, Choi [173] introduced a completely new idea that the Brownian motion of nanoparticles would produce a convection-like effect at nanoscale in nanofluids. The contribution of micro-convection to the thermal conductivity of nanofluids is estimated as

$$K_{conv} \propto C \frac{d_{mol,f}}{d_p} K_f Re_{d_{fluid}}^2 Pr\phi \qquad (9.4)$$

In this equation, C is proportional constant, $d_{mol,f}$ is the diameter of the base fluid molecule, and Re_{fluid} is the Reynolds number defined by,

$$Re_{fluid} = \frac{U_{droplet} d_p}{\mu_{droplet}}$$

In which $U_{droplet}$and $\mu_{droplet}$ are the random motion velocity of nanodroplets and dynamic viscosity of the base fluid. $\mu_{droplet}$ has been defined as :

$$\mu_{droplet} = \frac{2K_B T}{\pi \mu_{fluid} d_{droplet}^2}$$

Translational diffusivity, D_B is given in the Stokes equation

$$D_B = \frac{K_B T}{3\pi \mu_{fluid} d_{droplet}}$$

Where K_B is the Boltzmann constant, μ_{fluid} is the viscosity of the base fluid and T is the temperature.

The advantage of this advanced model is that both the temperature's and the size's dependence on thermal conductivity enhancement have been taken into consideration, and the predictions made by this model are in excellent agreement with the experimental data. Conventional EMT models fail to explain these dependences, and the reason lies in that in those models, nanoparticles are considered to be motionless, which holds only for large particles. The new dynamic model, by including the micro-convection mechanism due to the Brownian motion of nanoparticles, not only explains the particle loading and the temperature dependence, but also successfully explains the strong particle size dependence for the first time. This model has shown that the localized micro-convection caused by Brownian motion of nanoparticles plays a key role in enhanced thermal conductivity of nanofluids.

The thermal conductivity enhancement in water-in-PAO nanoemulsion fluids are then described by using the dynamic model, starting from the HJ model (and taking into

consideration of the contribution of the Brownian motion effects of water nanodroplets. The length of C-C bond is about 154 pm, and so, the diameter of PAO molecules is estimated as ~ 0.7 nm. Base on this molecular diameter, the mean free path of PAO molecules can be estimated

$$l_{mol,f} = \frac{1}{\sqrt{2}\pi d_{mol}^2 n} \qquad (9.5)$$

Where n is the density of PAO molecules, which can be estimated as n=2

The enhancement of thermal conductivity in nanoemulsion fluids then comes from two contributions: static thermal conduction and thermal convection caused by Brownian motion of nanoparticles, as shown in the following equation,

$$K_{EMT} = \frac{K_{droplet}(1+2\Gamma) + 2K_{fluid} + 2[K_{droplet}(1-\Gamma) - K_{fluid}]\phi}{K_{droplet}(1+2\Gamma) + 2K_{fluid} - [K_{droplet}(1-\Gamma) - K_{fluid}]\phi} K_{fluid} + C\frac{d_{mol,f}}{d_p}\left(K_f Re_{d_{fluid}}^2\right)^2 Pr\phi K_{fluid} \quad (9.6)$$

This model is used to describe the thermal conductivity of water-in-PAO nanoemulsion fluids and the results are shown in Figure 9.3.

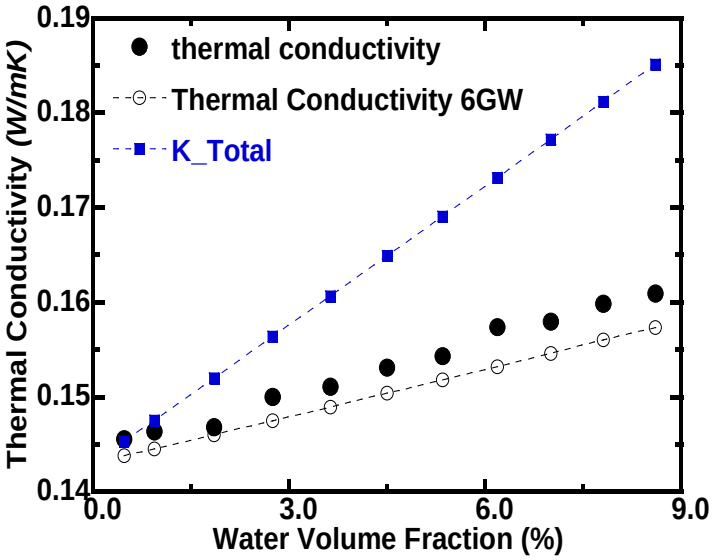

Figure 9.3 Thermal conductivity and numerical simulation for Water-in-PAO nanoemulsion fluids

It can be found that this model greatly overestimated the thermal conductivity enhancement at high concentrations of water nanodroplets when the contribution of the Brownian motion has been considered. This implied that there is no strong Brownian motion inside the Water-in-PAO nanoemulsion fluids even though the water nanodroplets are at 10nm or less in diameter. Similar phenomena are also found in Ethanol-in-PAO nanoemulsion fluids, which have an ethanol diameter of less than 0.9 nm. No anomalous enhancement of thermal conductivity has been found in Ethanol-in-PAO nanoemulsion fluids.

Overall, the thermal conductivity of these nanoemulsion fluids can be modified via adding suitable fluids inside, and no strong effect of Brownian motion on thermal transport are found experimentally in those fluids, even though the nanodroplets are extremely small. The higher thermal conductivity of added nanodroplets has a larger impact on thermal conductivity enhancement. The classic Maxwell equation can be used to estimate the thermal conductivity of nanoemulsion fluids and their variation with concentration of added nanodroplets.

Heat capacity modeling

The heat capacity of nanoemulsion fluid can be enhanced through two different mechanisms: one is due to the high specific heat of the dispersed phase; the other is due to the latent heat of the dispersed phase changeable nanodroplets. The latter one, i.e., use of PCMs, is much more efficient for the heat capacity enhancement. In water in PAO nanoemulsion fluids, the fluid's heat capacity can be

increased by the high specific heat of water (i.e., C_{water}=4.2 J/g C, C_{PAO}=1.88 J/g C) or the latent heat of water ($\Delta H = 334\ J/g$), depending on the operating temperature of the fluids. [174]

When water nanodroplets do not undergo solid-liquid phase change, the specific heat of the water in PAO nanoemulsion fluids follows the simple mixture rule:

$$C_{nanoemulsion} = (1 - \Phi)c_{oil} + \Phi C_{water} \qquad (9.7)$$

where Φ represents the concentration of the "water" phase. The specific heat of the pure PAO and water in PAO nanoemulsion fluids are measured using a Differential Scanning Calorimetry (DSC). DSC is a thermoanalytical technique that has been widely used to measure latent heat of phase change materials[175]. In this method, both the sample and reference are maintained at nearly the same temperature by adjusting heat input to them. The difference in the amount of heat supplied to the sample and the reference is recorded as a function of temperature (or time). In the curve of heat flux versus temperature or versus time, a positive or negative peak corresponds to exothermic or endothermic reactions in the sample, respectively. Enthalpies of phase transitions can be calculated by integrating the peak corresponding to a given transition,

$$\Delta H = c \cdot A \qquad (9.8)$$

where A is the area of the peak and c is the calorimetric constant. In order to determine the sample heat capacity, three measurements are usually carried out: the sample, the baseline and a standard. The baseline is subtracted from the sample record to obtain absolute values of the heat flow to the sample. The heat capacity can be determined by the heat flow, the temperature rise and the sample mass.

The specific heat of PAO and water-in-PAO nanoemulsion fluids is measured using a TA-CC100 DSC.

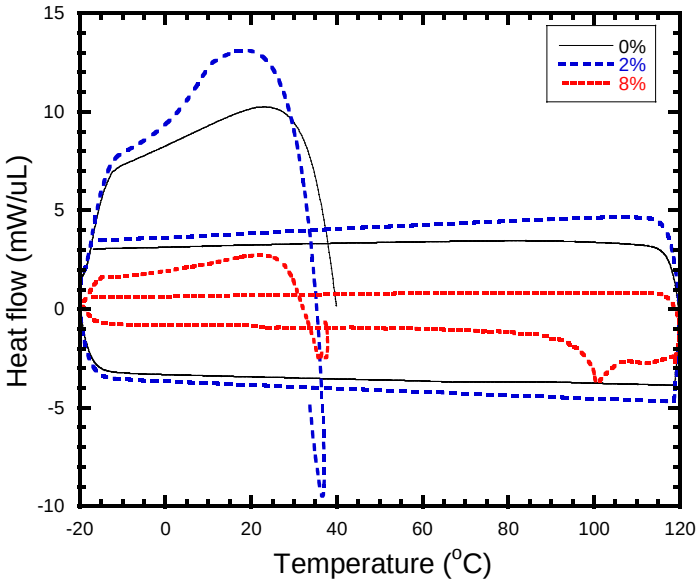

Figure 9.4 DSC cyclic curves of the pure PAO and PAO nanoemulsion fluids. The dispersed water droplets remain in liquid phase during operation.

The measured and calculated heat capacities of the water in PAO nanoemulsion fluids are shown in Figure 9.4. It can be seen that over 10% increase in heat capacity can be achieved for a water volumetric fraction of 8%.

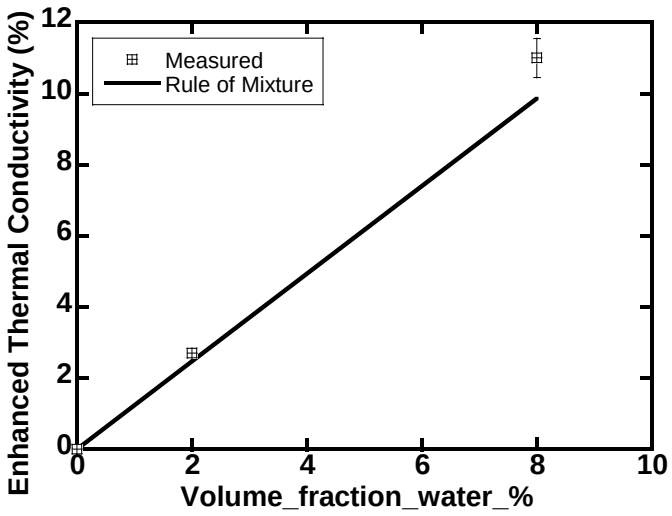

Figure 9.5 DSC measured and calculated heat capacities of water-in-PAO nanoemulsions. The heat capacities of nanoemulsions fluids are also calculated according to the rule of mixture (ROM)

Besides the observed enhancement of heat capacity via adding water into base PAO fluid, another very interesting and useful behavior is that, during the heating and cooling cycle, water nanodroplets undergo melting-freezing transition in the nanoemulsion fluids. The peak at about -20 °C is the exothermic crystallization (freezing) peak for the water nanodroplets in the fluids. These water nanodroplets exhibit a relatively large melting-freezing hysteresis, about 20 °C. The nanodroplet size has a strong effect on the melting-freezing process, so the shape of the freezing peak provides information about the nanodroplet size and thus about the nanoemulsion stability which also coincide with the inner structure change observed in Water-in-PAO nanoemulsion fluids[176]. The presence of a single freezing peak in Figure 9.6 indicates that the nanoemulsion fluids are well dispersed and all water nanodroplets are nearly monodispersed in size. The impact of phase-changeable water nanodroplets on the fluid properties is obvious: the effective specific heat of the fluids

can be significantly boosted. The effective specific heat can be defined as $C_{nanoemulsion} = C_{base\_fluid} + \phi H_{f,droplet} / \Delta T$, where ϕ is the volume fraction of the phase-changeable nanodroplets, $H_{f,droplet}$ is the latent heat of the phase-changeable nanodroplets per unit volume, and ΔT is the temperature difference between the heat transfer surface and the bulk fluid. In this experiment, if assuming ΔT =20 °C, the effective volumetric specific heat can be increased by up to 70% for the nanoemulsion fluid containing 8 vol % water nanodroplets when the water nanodroplets undergo phase transition. The use of phase-changeable nanodroplets is expected to provide a way to simultaneously increase the effective specific heat and thermal conductivity of conventional heat transfer fluids.

The heat of fusion H_f of pure water is 334 J/g, an outstanding value among those of phase change materials. The calculated H_f values of water-in-PAO nanoemulsions for different water loading from 2 to 8 volumetric percent are 7.5 and 30 J/ml, respectively, in agreement of the measured results shown in Figure 9.6, which are 0.3 J/ml, and 22.68 respectively. The volumetric heat capacity of water is about 4.18 J/ml.K, and is over two times the heat capacity of PAO. For a temperature increase from -10 to 0 ℃, 1 ml PAO absorbs 37.6 joules heat. For the nanoemulsion containing 8 vol% water nanodroplets, the melting of ice nanoparticle absorbs 30 Joules heat, which means, upon the melting of ice nanoparticles in the nanoemulsion, the heat capacity of PAO has been increased up by about 100%. Together with the enhancement in heat capacity caused only by the addition of water without phase

change, totally a maximum heat capacity increase of 110% is obtained in the 8 vol.% water-in-PAO nanoemulsion fluids.

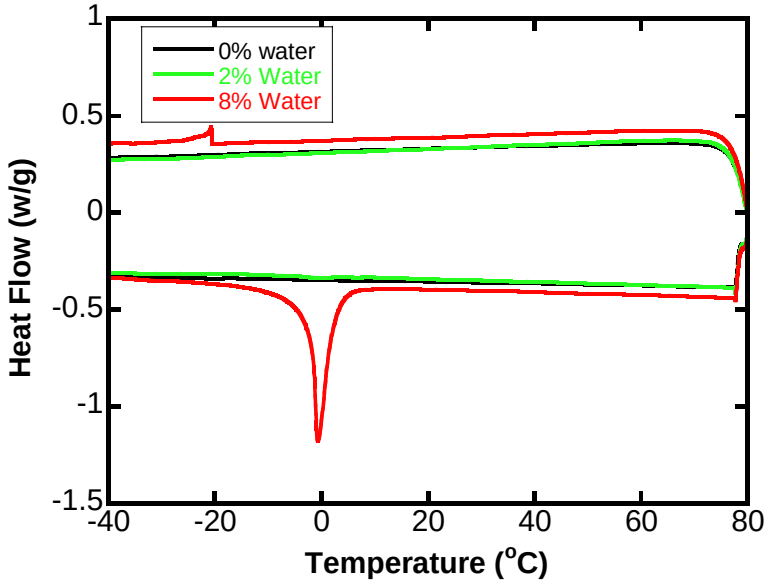

Figure 9.6 DSC cyclic curves of water-in-PAO nanoemulsions for different water loading. Exothermal peaks are observed at -20 ℃, corresponding to the freezing of water nanodroplets, while endothermal peaks are observed at 0 ℃, corresponding to the melting of water nanoparticles

.

Chapter 10: Conclusions, Major contribution and Future Directions:

Conclusion

In this study, a novel heat transfer fluids “nanoemulsion fluids” based on PAO are synthesized by adding conventional heat transfer fluids such as ethanol and water to form phase-changeable nanodroplets as the dispersed phases. They can be formed via two methods via self-assembly. The nanoemulsion fluids are transparent to natural light and can be identified using the Tyndall effect, where the laser beam is scattered by the nanodroplets inside. Several advanced structure characterization methods can be used to characterize the inner structure, and among them, small angle neutron scattering (SANS) is the main method used here. With the help of the ultra-small neutron beam and deturation methods used in SANS measurement, the SANS can measure the structure of concentrated colloidal system with resolutions up to 0.1nm. Following standard protocol and using empirical correlation, the reduced SANS data can be fitted and used to extrapolated the structure information inside the nanoemulsion fluids. The thermal transport properties of nanoemulsion fluids, including thermal conductivity, viscosity, and especially, phase change heat transfer coefficient in convective environment were characterized and modeled. A reliable 3ω-wire method has been established to precisely measure the effect of added nanodroplets on the thermal conductivity of nanoemulsion fluids. Phase change boiling heat transfer capability is also investigated using a homemade pool boiling test loop with ultra-fine (25um DI) platinum wire as the heater. With the help of high

speed camera, the bubble dynamics inside the nanoemulsion fluids are measured and compared with pure base fluid.

Ethanol-in-PAO nanoemulsion fluids are the first type of nanoemulsion heat transfer prepared and demonstrated here. There is a very minor increase (less than 3%) observed in thermal conductivity and up to 35% increase in viscosity. There is no abnormal Brownian motion effect on thermal conductivity observed even though the nanodroplets inside is only a few nanometer in size. Similarly, no abnormal viscosity increase is observed in nanoemulsion fluids, where very strong non-linear dependence of viscosity on nanodroplets concentration was observed. The addition of low-boiling point ethanol greatly decreased the wire heater temperature needed for the nucleation to happen, and the boiling heat transfer coefficient increased over 300% compared to that of base PAO fluid. Before the boiling happened, there was very minor increase in the free convection region that the addition of low-boiling point ethanol has negligible effect on the heat transfer coefficient without undergoing phase change which also agrees well with observed negligible increase in thermal conductivity in Ethanol-in-PAO nanoemulsion fluids. With the advantage of a high speed camera, the bubble dynamics inside pure ethanol and ethanol-in-PAO nanoemulsion fluids was compared and the observed bubble dynamics (bubble size, nucleation rate) were very different from each other. The reduced image data show that the bubble generated inside nanoemulsion fluids grows at a power law ranging from about t1/3 to t ¼, which is very different from pure ethanol. However, more systematical study is still needed to have a better understanding about this system.

Another group of nanoemulsion fluids investigated here is the Water-in-PAO nanoemulsion fluids which use water that has a much higher thermal conductivity compared to base PAO. The added water does increase the overall thermal conductivity, linearly, and can go up to 16% at the highest loading tested here. The observed viscosity has a non-linear dependence with the addition of water inside, which agree well with the observed inner structure change using the SANS method. A similar phenomenon is also observed in boiling heat transfer process where the boiling on the wire heater may follow two different trends, which also coincide with the concentration changes of water. It also agrees with Mori's study that the inner structure of water-in-PAO nanoemulsion fluids depends heavily on the molar ratio of water to surfactant which equals to the water concentration here as we fixed the concentration of surfactant used inside.

Besides the two types of nanoemulsion fluids we developed here, conventional liquid mixture of two fluorocarbon fluids is also studied using the same boiling test configuration here. Similar results can be obtained for pool boiling test which agrees well with Bar-Cohen's data. For flow boiling test, we observed that the flow motion actually has no improvement on the boiling heat transfer curves and it may even decrease the critical heat flux under high flow speed which might due to the instability of the bubble on the wire heater.

Numerical study shows that the currently available theoretical models can't explain all the observed thermal transport phenomena inside nanoemulsion fluids that well

and further study of more experimental data will help to improve the accuracy of the models via providing more supportive data.

Major Contribution

This study provides important and comprehensive information for the design, the synthesis, and the characterization and modeling of nanoemulsion heat transfer fluids, which have been regarded as a potential novel heat transfer fluid with improved thermal transport properties. The major contributions and accomplishments of this research are as follows:

1. Two innovative heat transfer fluids with greatly enhanced heat transfer properties are developed here: Water-in-PAO and Ethanol-in-PAO nanoemulsion heat transfer fluids were successfully synthesized with the presence of appropriate amphiphilic surfactants; the as-prepared Water-in-PAO and Ethanol-in-PAO nanoemulsion fluids are thermodynamically stable. The diameter of ethanol nanodroplets is less than 2 nm, while the shape of water nanodroplets changes from spherical to elongated cylinder of less than 10 nm.

2. A four-wire pool boiling testing loop with controlled subcooling temperature is established and used to characterize the phase change heat transfer characteristics in nanoemulsion heat transfer fluids. A clear observation window allows the direct

visualization of the nucleation process and is used for bubble dynamics study with high speed camera

3. Small Angle Neutron scattering method is used for the inner structure characterization of the nanoemulsion fluids prepared. The small angle neutron scattering method is able to measure complex colloidal system with sub nanometer resolution and does not need dilution of sample. It can also use deuteration methods to enhance the contrast and measure the size of the marked part only. A three-region G-P model is used to characterize the inner structure of water-in-PAO nanoemulsion fluids and explain the observed inner structure change.

4. Phase Changeable Ethanol-in-PAO nanofluids are synthesized and characterized. There is no abnormal Brownian motion effect on the enhancement of thermal conductivity even though the ethanol nanodroplet is at nanometer size. Meanwhile, a negligible thermal conductivity enhancement while a relatively large viscosity increase are observed which also appears to be of a nonlinear dependence with the increasing volume fraction of ethanol.

However, an over 300% enhancement of heat transfer coefficient after the incipience of nucleate pool boiling has been observed.

Furthermore, the low boiling point ethanol nanodroplets can greatly lower the heater temperature during nucleate boiling.

5. Phase Changeable Water-in-PAO nanoemulsion fluids are synthesized and tested here. A 16% increase in thermal conductivity is observed with about 30% increase in viscosity at highest water concentration tested here. Similarly, the addition of water also greatly enhances the effective specific heat by upto 110% and an elevated heat transfer coefficient upto 330% while lowering the heater temperature during pool boiling. These nanoemulsion fluids give a very promising way of simultaneously enhancing thermal conductivity, specific heat and nucleation heat transfer coefficient could show a bright direction for thermal fluid studies.

6. A mixture of two fluorocarbon fluids: FC72 and FC40 is also investigated here, and their pool and flow boiling heat transfer properties are characterized. Similar increase in pool boiling heat transfer is observed here as in Bar-Cohen's study while the flow boiling test shows non-obvious enhancement in heat transfer coefficient while the critical heat flux decreased.

Future Directions

The objective of the nanoemulsion fluids research is to provide possible solution to the emerging heat transfer demands in industry and military applications. We have successfully developed several new heat transfer fluids with greatly enhanced heat transfer capability, obtain comprehensive experimental data and appropriate theoretical models to help understand the nanostructures formed inside and their effect on the heat transfer enhancement, and then these data and models can be used to guide the production of nanoemulsion fluids for different applications, that is, if requirements of nanoemulsion fluids for different applications are proposed, a specific nanoemulsion fluid can be designed to meet such requirements by dispersing particles with specific properties, size and geometry, choosing suitable base fluids, using appropriate additive fluids and forming idealized nanostructure inside.

The exciting results are just demonstrating the potential applications of nanoemulsion fluids in advanced thermal management systems. Both pool and flow boiling experiments have shown encouraging results with greatly enhanced heat transfer coefficient and a lower heater temperature. Although the usage of nanoemulsion fluids in a wide variety of thermal management applications has a brilliant future, the main blockade that hindering the development of nanoemulsion

research and application is that a detailed atomic-leveled understanding of all the mechanisms which are responsible for the observed change of properties is unclear yet. However, there are still several important clues indicating the mechanisms of heat transfer in nanoemulsion fluids, which can include the following based on my limited study:

1. The properties of the dispersed nanodroplets seem to be important. Simply based on the mixing rule, the added nanodroplets with a better thermophysical properties can eventually enhance the overall thermophysical properties of the nanoemulsion fluids which has also been confirmed by our experimental observation.

Meanwhile, thermal transport in nanoemulsion fluids involves the heat transfer during the phase change of added nanodroplets, in the vicinity of the nanodroplets, formed bubbles and base fluid interfaces, so the added nanodroplets with different phase change properties will affect the phase change process of themselves and the heat transfer rate between themselves and base fluids. The added nanodroplets of lower boiling point will initiate the nucleation process and movement of the bubbles will dramatically change the overall heat transfer process and enhance the heat transfer there forth. However, based on the data and understanding currently available, the direct correlation between the thermophyaical and phase change properties of nanodroplets and

formed nanoemulsion fluids is not fully understood yet, plus that there is a third component added inside. Thus it is difficult in the nanoemulsion research to uncouple the effect of particle size on heat transfer from other factors.

2. Size of dispersed nanodroplets seem to be important. With reducing nanodroplets size, the dispersion behavior improves and the surface-to-volume ratio increases.

Similar to the effect of different nanodroplets added inside, the increased surface area will affect the heat transfer rate between nanodroplets and fluids. However, the understanding of the size of nanodroplets and its effect on thermophyical and phase change heat transfer capabilities is very limited, and current available data is obtained over a rather narrow range of sizes. A challenge is to start a systematic study of a series of nanoemulsion fluids and pin-point the effect of the size of the dispersed nanodroplets.

3. Bubble dynamics and interface during phase change process is unclear. The bubble initiation on heater surface is affected by many factors which includes the different compositions of nanoemulsion fluids, heater materials and surface structure etc. After the generation of bubbles on heater surface, the dynamics of bubble on heater surface

is a complex process and currently available high speed camera data can't give quantitatively explanation. On the other hand, classic theories and correlations can't explain the process observed here.

4. Other effects during boiling test such as heating surface and pressure are not investigated here and it may affect the heat transfer greatly. A better understanding of the nucleation process and dominating factors during that process can be achieved after a systematic study of the boiling heat transfer under different testing conditions such as different heating element with different surface conditions, different pressure and subcooling temperature etc. The better understanding of the effect different test conditions, the better we can utilize these novel heat transfer fluids in different systems, and even to redesign the system to future enhance the heat transfer capacity.

5. The temperature dependence of thermal conductivity enhancement may be exploited. Quite a few studies have reported that the thermal conductivity enhancement of nanofluids show a strong temperature dependence. This temperature effect not only provides a clue that the nanodroplets motion in nanoemulsion fluids may play an important role, but also indicates that nanoemulsion fluids are suitable to be used as a type of advanced coolants at elevated temperatures.

6. Phase change nanodroplets are useful to simultaneously improve the thermal conductivity and heat storage capacity of nanoemulsion fluids and further increase the heat transfer efficiency. Two phase-change nanoemulsion fluids have been developed and characterized in this research which gives very promising results. Other combinations of phase change nanoparticles and base fluids are going to be explored.

Publications:

Book chapters:

1. **Jiajun Xu,** Bao Yang, "Novel Heat Transfer Fluids: Self-assembled Nanoemulsion Fluids," "Nanoproperties", ***NANOTECHNOLOGY***, STUDIUM PRESS LLC, Volume 2, Issue 3, May 2013

2. **Jiajun Xu**, Fangyu Cao and Bao Yang "Phase Change Material Particles and Their Application in Heat Transfer Fluids" Low-cost Nanomaterials**: Toward Greener and More Efficient Energy Applications,** by Zhiqun Lin & Jun Wang, 2013

Journal papers:

1. **Jiajun Xu**, Bao Yang, Boualem Hammouda, "Thermophysical Properties and Pool Boiling Characteristics of Water in Polyalphaolefin Nanoemulsion Fluids", ***ASME Journal of Heat Transfer***, HT-12-1328, 2013

2. **Jiajun Xu**, Bao Yang, Boualem Hammouda, "Thermal conductivity and Viscosity of Self-assembly Alcohol/Polyalphaolefin Nanoemulsions" ***Nanoscale Research Letters***, 6:274, 2011

3. **Jiajun Xu**, Bao Yang, “Thermal and Phase Change Characteristics of Self-Assembled Alcohol/Polyalphaolefin Nanoemulsion Fluids”, ***Journal of Thermophysics and heat transfer AIAA*** Vol.24, No.1, January–March 2010.

4. Chunwei Wu, Tae Joon Cho, **Jiajun Xu**, Donggeun Lee, Bao Yang, and Michael R. Zachariah, “Effect of nanoparticle clustering on the effective thermal conductivity of concentrated silica colloids” ***Phys. Rev. E*** 81, 011406, 2010.

Conference Proceedings:

1. **Jiajun Xu**, Bao Yang. "Thermophysical Properties and Pool Boiling Characteristics of Water in Polyalphaolefin Nanoemulsion Fluids", ***ASME 2012 Micro/Nanoscale Heat Transfer International Conference***, Atlanta, GA, Mar. 2012

2. **Jiajun Xu**, Xinan. Liu, Tian Tran, Bao Yang, “Thermal and phase change characteristics of self- assembled PAO nanoemulsion fluids” ***ASME 2nd Micro/Nanoscale Heat Transfer International Conference***, Shanghai, December 18-21, 2009

3. **Jiajun Xu**, Xinan Liu, Bao Yang, “Thermophysical Characteristics of Self-Assembled Alcohol/Polyalphaolefin Nanoemulsion Fluids” ***IMECE2009-12544*** pp. 2023-2026Volume 9, ASME 2009 International Mechanical Engineering Congress and Exposition (IMECE2009) November13–19, 2009

Appendices

Small Angle Neutron Scattering Measurement and Data Reduction:

Introduction: Small-Angle Neutron Scattering (SANS)

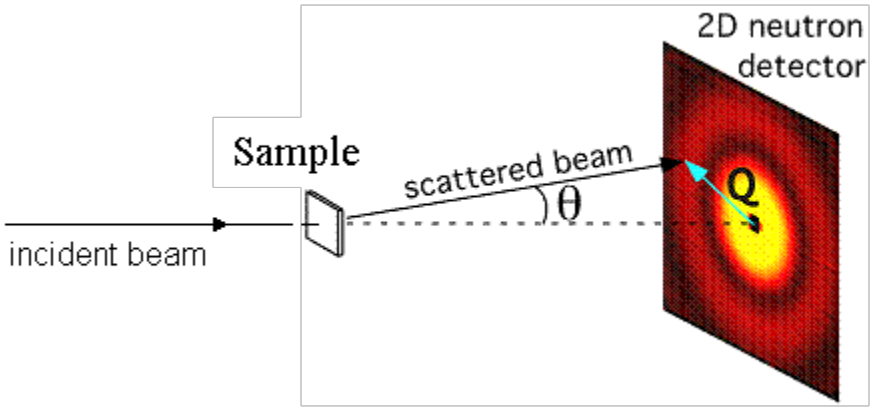

Small-Angle Neutron Scattering (SANS) probes structure in materials on the nanometer (10-9 m) to micrometer (10-6 m) scale. Structure on this length scale is critical to the performance of advanced engineering materials. For example, the toughness of high impact plastics depends on the admixture of stiff and flexible segments of polymer molecules on the nano-to-micro scale.

Nanometer/micrometer structure is also crucial to biological processes in cells, to the storage of information on magnetic disks, to the hardness of steels and superalloys, to the conduction of current in superconductors, and many other materials properties.

In SANS, the neutron wavelength, λ , and scattering angle, θ , determine the length scale probed through the relationship

$$d \approx \frac{\lambda}{\theta} \frac{(\text{wavelength})}{(\text{scattering angle})}$$

Through the use of cold (i.e. long wavelength) neutrons and tight beam collimation, the SANS instruments at the NCNR are able to probe structure on a length scale, d, ranging from 1 nm to nearly 10,000 nm.

Equipment: NG3 30m SANS

Table A-1: NG3 specification and properties

Q-Range	*0.015 nm-1 to 6.0 nm-1*
Size Regime	*1 nm to 500 nm*
Source	*Neutron Guide (NG-3), cross-section: 60 mm x 60 mm*
Monochromator	*Mechanical velocity selector with variable speed and pitch*
Wavelength Range	*5.0 Å to 20.0 Å*
Wavelength Resolution	*10% to 30% Δλ/λ (FWHM)*
Source-to-Sample Distance	*4 m to 16 m in 1.5m steps via insertion of guide sections*
Collimation	*Circular pinhole collimation*
Sample Size	*0 mm to 25 mm diameter*
Sample-to-Detector Distance	*1.3 m to 13.1 m continuously variable*
Detector	*640 mm x 640 mm 3He position-sensitive proportional counter with a 5.08 mm x 5.08 mm resolution*

SANS Data Reduction and Curve Fit Protocol:

The SANS data obtained using NG3 30m beamline is reduced using standard protocol listed on NCNR NIST website and followed the SANS data reduction help file (V5.2). The detailed procedure is listed as below:

1. The SANS Data Reduction using IGOR Pro is an implementation of the VAX data reduction procedures in an easier to use, graphical interface. It is designed to work on Macintosh or PC, and works directly on raw binary data files as collected on the VAX or through ICE. The procedures and software that are available for displaying and processing 2D SANS data (subtracting background, converting to an absolute scale, averaging, etc.) to produce reduced 1D or 2D data in intensity versus wavenumber (I vs. Q) form are described in the following sections.

The raw, 2D (128 rows x 128 columns) data collected at the instruments resides in SANS user accounts in the form of individually named binary files. The format of the data file names is: XXXXXNNN.SAn_INI_AMMM

where XXXXX is a 5-character sample prefix, NNN is an automatically incremented 3-digit run number, and SAn denotes the SANS instrument where the data was collected (n=1 for the NG1 SANS instrument, n=3

for NG3, and n=2 for NG7 SANS). INI denotes the user's initials, and AMMM is a 4-digit alphanumeric run identifier for archiving purposes. Raw data files are stored on a main server and are protected from deletion. During your SANS experiment, as each data file is collected, the raw data files are mirrored to a central server, "Charlotte". If your SANS account is NG3SANS41, your data will be located in the "NG3SANS41" folder on Charlotte.

Charlotte is visible to Macs through Appleshare (connect as a guest), and to Windows through the Network Neighborhood (NCNR group, Map the "SANS Data" folder as a network drive). This central server allows you to (within the building) work directly with the data on Charlotte. The data on the main server remains untouched, as a backup. You can see and reduce the data while at the instrument, in the computer room, or in the user offices. Once your experiment is finished, all of your data – raw data files, averaged data, IGOR Demo version (if needed), SANS Reduction Macros... can be copied from Charlotte onto a USB drive or CD and carried home (a typical SANS session will produce between 2-6 MB of raw data).

The 128x128 data values in the raw data files are never altered; only the file

header, which contains parameters such as the beam center coordinates,

transmission, detector distance, etc. can be modified (using a Patch operation). For analysis, the data are loaded into a working folder "EXT", where EXT is a 3-letter mnemonic of the data "type" that represents the logical function of the data in the reduction sequence or the result of a processing step. For example, SAM, EMP, and BGD represent sample data, empty cell data, and background data, respectively. The data type COR identifies the results of combining the SAM, EMP, and BGD data to produce sample data that has been corrected for background and empty cell scattering. The data in work folders are processed by invoking a protocol that performs a sequence of specific operations, in some cases writing the result to a different work folder, overwriting the previous contents. Ultimately, the corrected data is saved to

disk in the desired format in an "averaging" step. Typically the 2D data is circularly averaged to produce 1D (I vs. Q) ASCII data files. These 1D data files contain instrumental resolution information in addition to the intensity data. The "averaging" step can be configured to save a variety of 1D formats, including 2D ASCII files or PNG graphics images.

2. Initial correction

As data is loaded for use as SAM, EMP or BGD data types, each dataset is normalized to a fixed number of incident neutrons

(corresponding to a monitor count of 108 counts) to facilitate comparisons between data sets. Sample data is corrected for background and empty cell scattering according to the algorithm:

COR = (SAM - BGD) - [Tsam/Temp](EMP - BGD)

where Tsam is the transmission of the sample and Temp is that of the empty cell. Note that Tsam and Temp are taken with respect to the empty beam. Thus, if no cell is used (i.e., empty beam condition), Temp = 1.0. The results of this operation are stored in another work folder, COR.

3. Detector Efficiency Corrections

An important step in the data reduction process involves correcting for the detector response. A data set can be corrected for non-uniformities in the detector efficiency by dividing the data, pixel-by-pixel, by the measured scattering from an isotropic scatterer such as plexiglass or water. Plexiglass runs are measured periodically by the instrument scientists for this purpose and saved as PLEX_DDMMMYY_NGn.DIV files which indicate the date the measurement was made (DDMMMYY) and the instrument used (NGn). These files are stored on Charlotte in a folder named NGn_FILES. The DIV file for the current cycle should be copied to your directory before reducing your data. Subsequently the corrected data, COR, is divided, pixel-by-pixel, by the contents of DIV. This calibrated result is written to a separate work folder, CAL.

4. Masking the dataset

The last step before averaging the data to reduce it to I vs Q form is to mask the dataset. This operation has the effect of marking, or masking, specific pixels in the 2D data field that are to be ignored in the subsequent averaging process.

5. Averaging the dataset

b

6. List the Data Files

All of the raw data files, detector sensitivity files, mask files, etc. must be kept in a single folder for IGOR to access them. From the main panel, click "Pick Path" to set the path to this folder. On a Mac, if your data is inside "Tutorial Data", the dialog should look like this. On Windows, the dialog will look slightly different.

Once the path is set, click "File Catalog" to create a catalog table listing of all of the files in the selected folder. Raw SANS data files will show descriptive header information like the label, counting times, and thickness and transmission. The columns can be resized to see the whole label, etc., or delete columns of information you don't want to see. This table is also used interactively for building data reduction protocols, and is detailed later. Clicking "File Catalog" again will

rebuild the list of files, and should be done if files were added to the folder or to confirm that header information was updated correctly. The table will list all of the files in the data folder, displaying information about raw SANS data files only. Files that are not recognized as raw SANS data are appended to the bottom of the "Filenames" column. Note that in the "Filenames" column, there are two important files listed that are not raw SANS data - these are the mask and detector sensitivity files.

7. Calculate Transmissions

1) Open the Transmission panel by clicking " Transmission" on the Raw Data

tab of the main panel. The following new panel will appear:

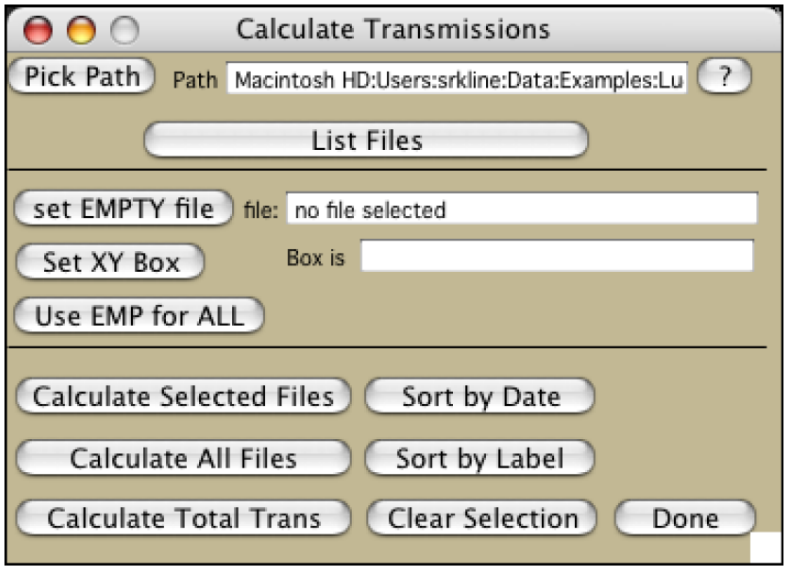

2) Click on "List Files" to build two tables - one with scattering files:

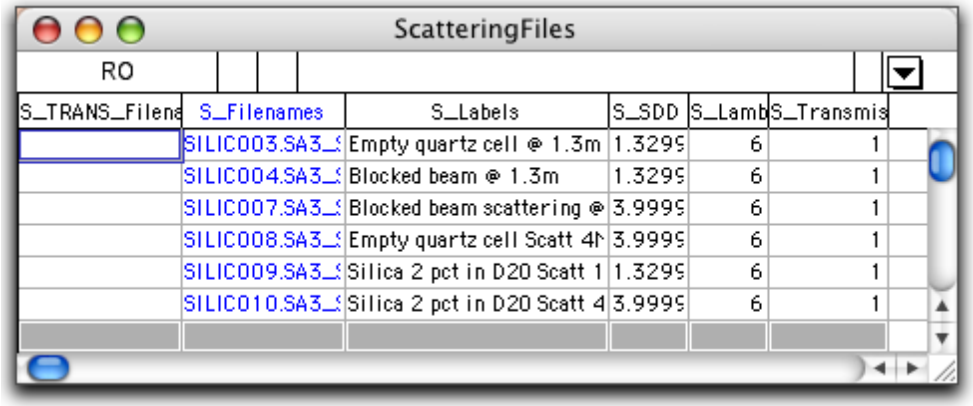

and another with transmission files. The transmission files are automatically separated from the scattering files based on the beamstop location (off-center) in the header of the raw data file.

3) Find the empty beam transmission measurement in the TransmissionFiles table. It is in the blue "T_Filenames" column. For the tutorial, it is file SILIC002.SA3.... Click on this file to select it (just that cell in the table). In the Transmission Panel, click "Set EMPTY File" to set this file as the empty beam. The filename appears, as well as the box coordinates:

4) Now make the associations between the empty beam file and each of the

transmission measurements. Each transmission measurement for a sample must be normalized relative to the empty beam transmission (and should therefore be less than unity). Make the EMPty beam association by selecting the empty beam file (in the blue column),

copying it, and pasting the filename into the "T_EMP_Filename" column. Transmission was only measured of two samples: the silica (2 % by weight of colloidal silica in D2O, held in a quartz cell), and an empty quartz cell. Note the consistent sample and transmission labels (that you enter when you acquire data). Keep the "trans" or "scatter" identifiers at the end of the labels - or drop them altogether. The program already knows the difference.

5) Now make the association between the transmission measurement of the silica (SILIC006) and the scattering file(s) for the same sample. In this case, the silica scattering was measured twice - using two different instrument configurations. The sample is the same, and so is the transmission, so copy the filename of the silica transmission (SILIC006...) from the blue "T_Filenames" column, and paste it into the (2) proper locations in the "S_TRANS_Filenames" column in the ScatteringFiles table

8. Build a protocol

Click "Build Protocol" on the Data Reduction tab of the main panel. This will present a new panel with a list of reduction steps that can be used. Steps that are checked will be performed, steps that are not checked will be skipped (except that you will always supply a sample file, or be prompted for one). For this example, we will use nearly all of

the data reduction steps, and first build a protocol to reduce data taken at a 4 meter sample to detector configuration and use absolute scaling from an empty beam measurement. Click "Show File Catalog" to bring the listing of files to the top, and arrange the windows so the list and the panel are visible.

1) Leave the sample field as "ask" so that the program will prompt us for the sample data file(s) when they are needed. We could specify a file to bypass the dialog, if desired.

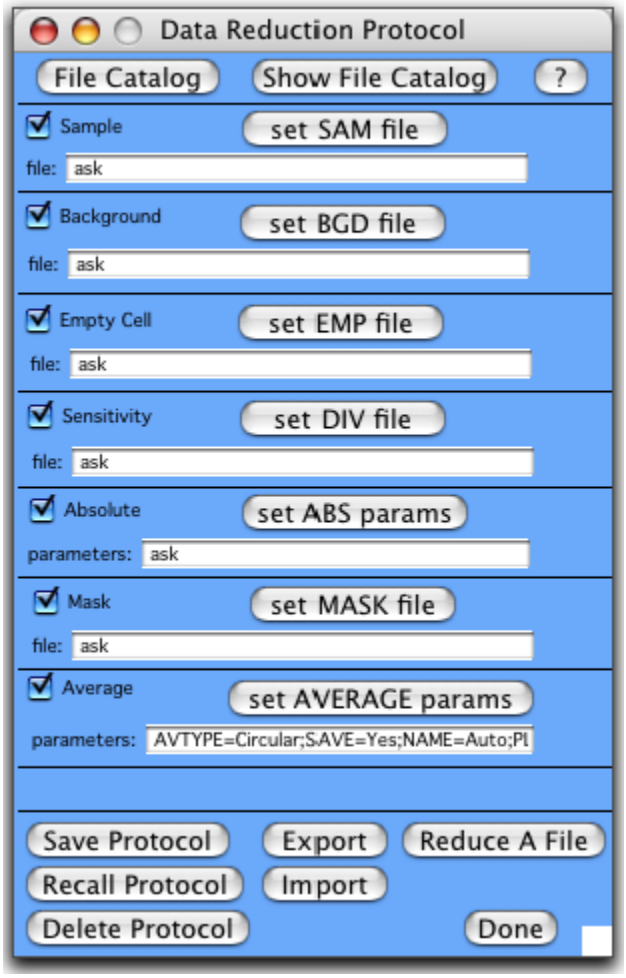

2) Fill in the background file by finding it in the listing (run SILIC007), clicking to select the filename, and then clicking "Set BGD file" on the panel.

Say "Yes" to reset the list of files. This will set this single file (the selected text) as the background file. If several background files were collected and it is desired to add them together, reset the list for the first file, and then select "No" (don't reset) for additional files to add together. These additional files will be listed in the field as well and added together during the data reduction. The EMP (and SAM) file fields are set in an identical fashion.

3) Fill in the EMPty cell file in the same way that the BGD file was set. It is run SILIC008.

4) Set the detector sensitivity (DIV) file. The file is PLEX_2NOV2007_NG3.DIV (at the bottom of the Data File Catalog table). Note that it is not a raw SANS data file, and is not recognized as such by the listing. There can only be one detector sensitivity file assigned to a protocol.

5) Set the absolute scaling parameters.

6) Returning to the Protocol Panel, click on the "DEFAULT.MASK" filename in the listing, which is a simple mask to exclude the edges of the detector. Click "set MASK" to set the filename. The mask file was created either in IGOR Pro or in SANS Image.

7) Default values for a circular average of the data (annulus width is always one pixel) should already be in the field.

8) Once all fields are set to their correct files / parameters, click "Save Protocol" to save these settings for later recall, using a descriptive name for the protocol.

9. Reduce a file

Use the protocol built previously, we can now reduce a file:. Start with the 4-meter protocol. To make sure it's in place, click "Recall Protocol" on the panel, and pick "sdd_4meter", or whatever you named it from the list. Your protocol choices are updated in the panel. At this point, you can choose the 4-meter silica scattering file from the Data File Catalog window, and "Set SAM File", or since the protocol says "ask", just let it prompt you with a file dialog. You could also enter a list of run numbers. When done, click "Reduce A File" on the Protocol Panel. Pick the scattering file from the dialog if prompted (it's run

SILIC010...). The file will be displayed, and you will be prompted to add another sample file, if desired:

The data reduction will proceed through the protocol, showing each intermediate step along the way. Watch closely - if something doesn't look right, go back and check it out after the reduction is done. If something is grossly in error, the reduction can be aborted (cmd-. on Macintosh, or the Abort button at the lower left in Windows. This example will proceed smoothly, of course. The final result should look like this, and the command window should indicate that a data file was written, and what filename was used.

Till now, a standard data reduction procedure for SANS data obtained using NG3 30m has been introduced and now a curve fit protocol will be discussed using water-in-PAO nanoemulsion we prepared for example:

The general procedure for fitting a model to your data is:

1) Load in your SANS data

2) Plot a model function

3) Visually adjust the model parameters

4) Set up the curve fitting parameters

5) Do the fit

6) Make publication-quality graph

1. Loading SANS Data

Upon loading the NCNR Analysis Macros, the Fit Manager and the SANS Model Picker will open, and a SANS Models menu will appear. To load a data set, use the "Load 1D Data" button on the Fit Manager: Here we load “water-in-PAO” data into Igor Pro

2. Plotting a Model Function

When the analysis macros are initially loaded, there are no model functions available. Each model must be included individually, as needed. For this tutorial, include the CoreShell model by selecting it in the list, and clicking "include". The file will appear in the lower list of files that are currently included, and the CoreShell model will appear under the "Function" popup on the Curve Fit Setup panel (the Fit Manager).

Model functions are plotted by selecting the appropriate function from the popup, either resolution smeared, or unsmeared and then the "Plot 1D Function" button. These "Plot" macros will create the x and y waves of model data, a table of adjustable parameters, and graph the model function. Plot the CoreShellSphere function from the panel, taking the default number of points and q-range.

Click "continue" to accept the default ranges, and the following graph is generated, and the coefficients for the model function are inserted in the table.

The table of fitting coefficients appears directly below the set of popups. Plotting a model function creates x and y values with appropriate extensions, xwave_ext and ywave_ext. Coefficient and parameter waves are likewise created for the table. For the Core-shell sphere model, the extension is "css". If you're curious about the details of the model calculation, documentation of each model is available and the code is visible under the Windows- >Procedure Windows menu.

3. Testing the Model

What we really want to see is how the model compares to the experimental data. Add the model data to the experimental data by bringing the graph of the experimental data to the front, then choosing the "Append 1D" button on the Fit Manager. Note that you will be appending the "active" function (whatever is currently selected in the popup) onto the "active" window (whatever is on top).

The model data has been appended to the graph, and is in fact a poor representation of our experimental data. Let's see how changing the parameters affects the model. The model intensity "ywave_css" is a

"dependent object" - that is, the wave depends on the parameter values in the table - change any of the values, and the data in the graph is automatically updated. For the apoferritin sample, we know that it was prepared in deuterated water at a concentration of 1% by volume. From the crystal structure of the protein, it is also known that the structure resembles a hollow spherical shell of protein. So set the scale equal to the

volume fraction, and the scattering length densities of the solvent and the core (which is filled with solvent) to the scattering length density of D2O. If you don't know this number, a very useful tool for calculating scattering length densities can be found at: <http://www.ncnr.nist.gov/resources/sldcalc.html>, along with a growing list of tools for planning your experiment at NIST.

4. Setting up the Fit Parameters

You're ready to fit the core-shell model to the data now. All of the curve fitting setup can be done from the Fit Manager Panel. First, make sure that the data set and function are properly selected.

This will set the data set to fit (using the appropriate statistical weighting, and resolution if fitting to a smeared model) and the function to use, and your initial guesses for the parameters. Since we know the values of the scale and two of the scattering length density

inside and outside (both D2O), we want to hold these values fixed during the fitting. Enter "1" in these rows of the "Hold_css" column of the table. Values of "1" will be fixed at your guesses, and "0" will be automatically adjusted during fitting.

5. Fit Results

Click "Do 1D Fit, and the fit will be performed, updating the model as it (quickly) converges to a solution. The best-fit parameters and one standard deviation are reported to the command window at the bottom of the screen, and reflected in the table. The W_sigma column at the far ritght of the table represents one standard deviation of the fitted parameters. ALWAYS think

about whether the returned values are physically reasonable based on what you know about your sample. Unphysical results may indicate an error in setting up the fit operation or indicate that the model is a poor representation of the sample. "FitYw" is the fitted result, appended automatically to your graph. The model ywave_css also reflects the best-fit coefficients.

6. Other cases

For colloidal systems which does not experience inner structure change, their SANS data can be fitted using one model. However, most colloidal systems including nanoemulsion fluids here, they can undergo

inner structure change with the change of concentration, temperature and sanlity etc. Especially for the water-in-PAO nanoemulsion fluids we prepared, the simple correlation length model can't fit all the SANS curves well for both low and high Q region. The fitting curves using Hard Spere model is shown below:

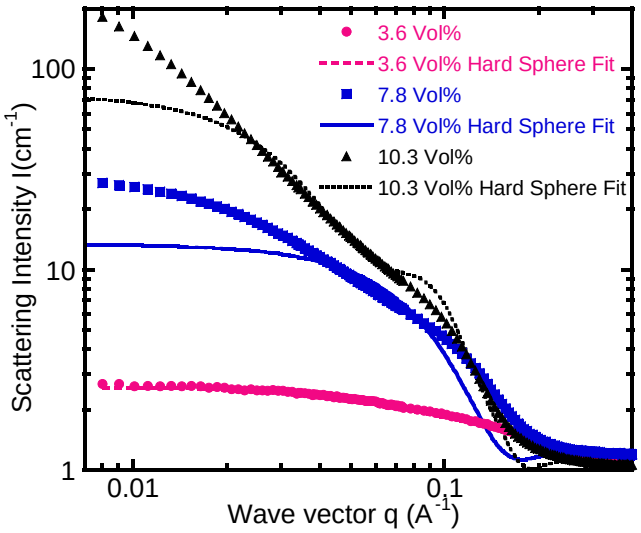

A-1 Small Angle Neutron Scattering curves for Water in PAO nanoemulsion fluids(Solid Symbols) and Hard Sphere Model curve fittings (Colored Lines)

It is also clear that, for D2O/AOT/PAO microemulsion with high D2O concentration, the hard sphere model can not accurately describe its inner structure which shows large discrepancy especially for low q portion. So, a new Guinier-Porod empirical model is used to fit SANS data from spherical to as well as nonspherical objects such as rods or platelets. Generally, the scattering intensity is given by the two contributions in Guinier-Porod model:

$$I(Q) = \frac{G_2}{Q^{S_2}} \exp(\frac{-Q^2 R_{g2}^2}{3 - s_2}) \text{ for } Q \le Q_2,$$

$$I(Q) = \frac{G_1}{Q^{S_1}} \exp(\frac{-Q^2 R_{g1}^2}{3 - s_1}) \text{ for } Q_2 \le Q \le Q_1,$$

$$I(Q) = \frac{D}{Q^d} \text{ FOR } Q \ge Q_1$$

Here $3 - S_2$ and $3 - S_1$ are the dimensionality parameters, and R_{g1} and R_{g2} are the radii of gyration for the short and overall size of the scattering object. This generalized Guinier-Porod model can be used to analyze SANS patterns from nonspherical objects: In general, for scattering objects with spherical symmetry $S_2 = S_1 = 0$ and for cylindrical objects $S_2 = 0$ and $S_1 = 1$. For lamellae with equal width and length, one has $S_2 = 0$ and $S_1 = 2$.

This model is fitted and compared with SANS data in Figure 8 especially to cover the $Q \le Q_1$ range and the results show that the 3-region G-P model fits the low q range pretty well and the measured correlation length is changing from 121.6A to 47.4A when the D_2O volume concentration is changed from 10.3 Vol% to 7.8 Vol%. If take a closer look at the fitting curves, the obtained "dimensionality" parameters $S_2 = 0.22$ and $S_1 = 1.4$ for 10.3 Vol% sample and $S_2 = 0.18$ and $S_1 = 0.97$ for 7.8Vol% one. So $S_2 \approx 0$ and $S_1 \approx 1$ gives a cylinder shaped object inside under these two water volume

concentrations. It is also noteworthy that the $S_2 = 0.04$ and $S_1 = 0.25$ is calculated for the 4.5 Vol% one which can be approximated to $S_2 \approx 0$ and $S_1 \approx 0$ which represents a spherical object just as shown before using Hard Sphere model fitting.

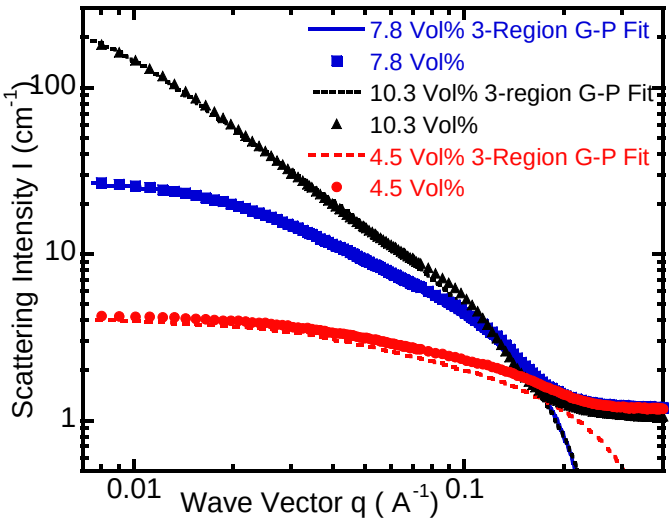

A-2 Small Angle Neutron Scattering curves for Water in PAO nanoemulsion fluids(Solid Symbols) and 3 region Guinier-Porod Model curve fittings (Colored Lines)

Heating Control Module Design

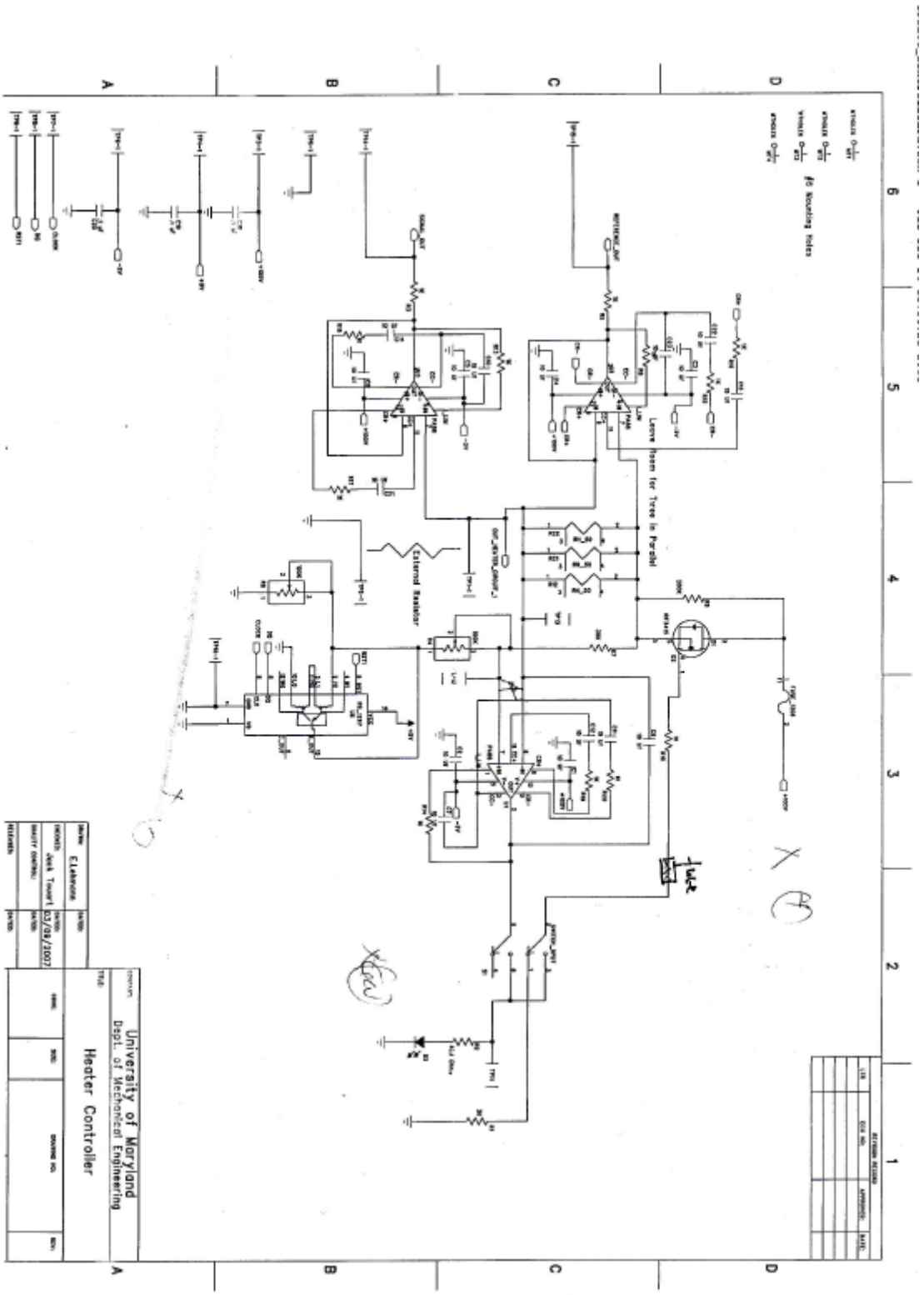

MAG Gear Pump Manual

Flow pump

A model FG213 MAG gear pump is used here for the flow boiling test and its specification is listed below:

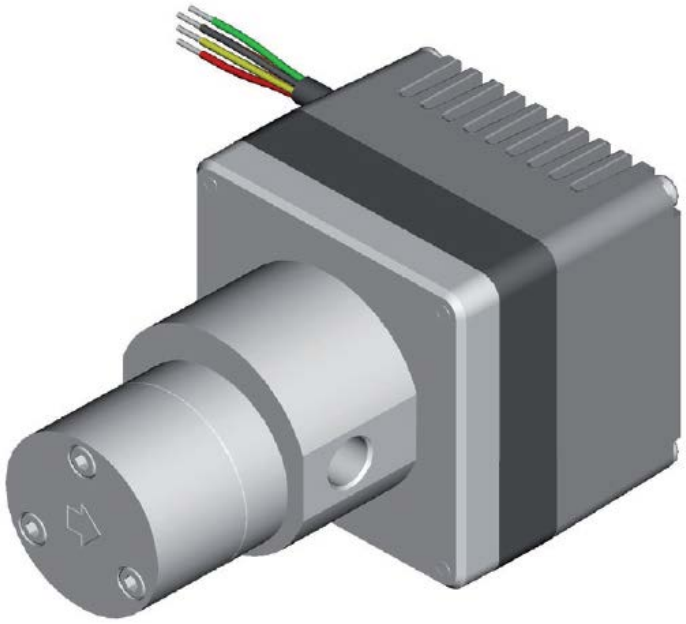

Specification:

Operating working conditions

Nominal torque 100 mN*m @ 3500 rpm
Speed range from 300 to 5000 rpm
Direction of rotation clockwise / counterclockwise*
Max ambient temperature 40°C/104°F at the maximum torque (70°C/158°F at 70 mNm torque)
Max fluid temperature 55°C/131°F at the maximum torque (95°C/203°F at the lower torque)
Unit protection level IP52
Relative humidity 90% or less without condense
Storage temperature - 40°C + 85°C/-104°F + 185°F
* counterclockwise available only for the version without electronic driver

PIN FUNCTION: VERSION WITH ELECTRONIC DRIVER]

WIRE COLOR	SYMBOL	DESCRIPTION	
Red	PWR_VCC	Power supply (+24V)	
Black	PWR_GND	Power ground (0V)	
Orange	SPEED IN	Analog input speed command 0-5V	
		Voltage Input	Output (rpm)
		In < 0.2V	0
		0.3V < In < 5V	300 > Out > 5000 linearity speed vs command +/- 5% with no load
Brown	0V	0V speed command	
Yellow	TACHO OUT (SPEED OUT)	DC output voltage: 0-5V DC output source current: max. 5mA Output square signal frequency: max. 2.7 KHz	
Green	NC	Not connected	

IMPORTANT NOTE:
never connect PWR GND and 0V together, otherwise the integrated elctronic board can be seriously damaged.
* Speed [rpm] = Frequency [Hz] * 60/32

ELCTRICAL CONNECTION

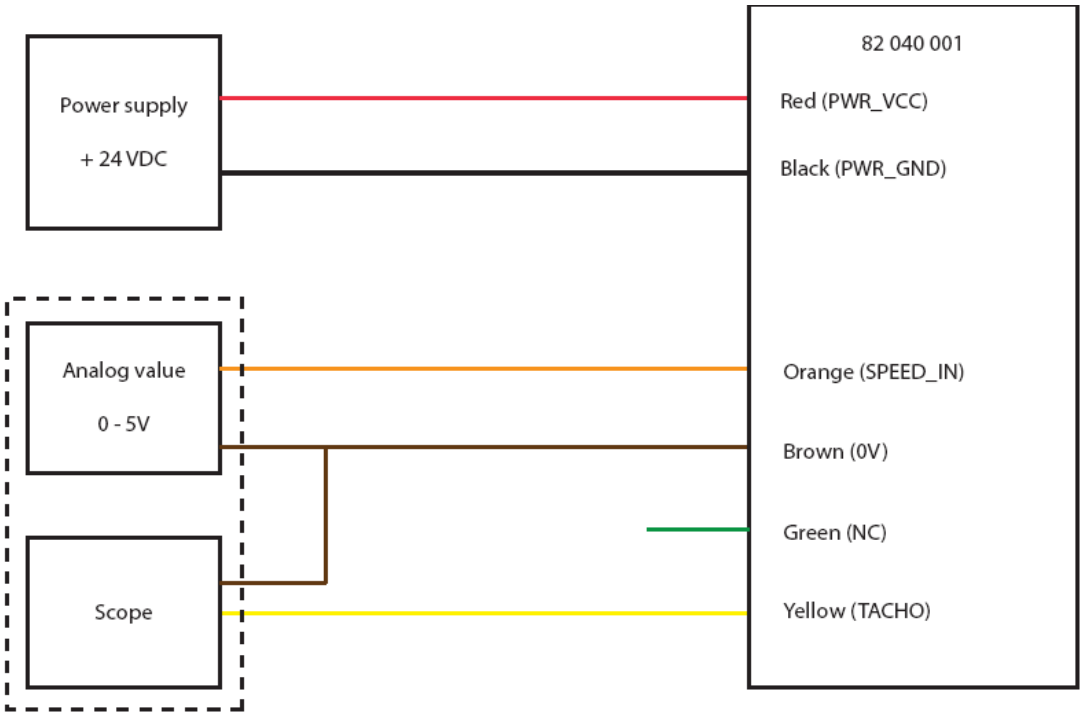

RPM VS VOLTAGE DIAGRAM

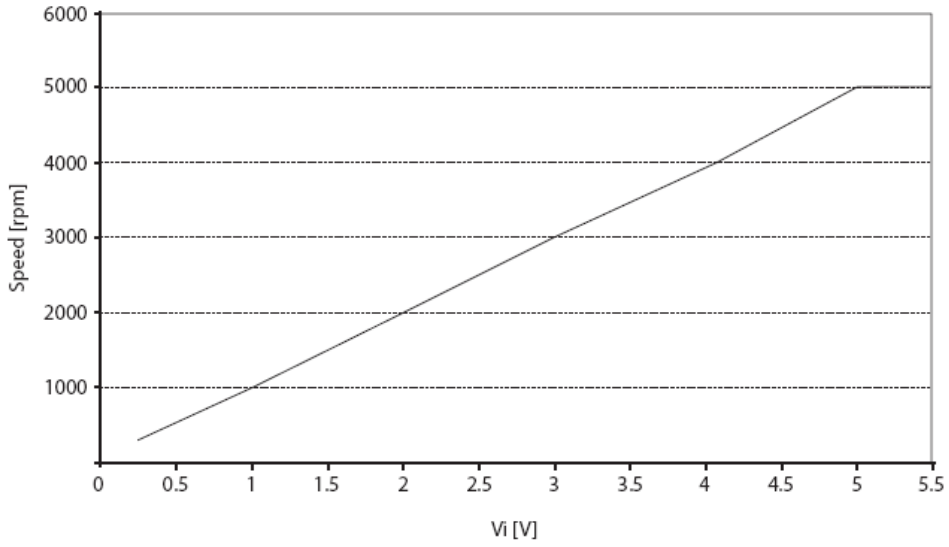

Bubble Visualization Test

High speed camera

Specification:

Resolution	***FPS***
2560 x 1600	1,500
2048 x 1600	1,800
2048 x 1024	2,800
1920 x 1080	2,700
1280 x 800	5,250
1280 x 720	5,850
800 x 600	8,250
640 x 480	12,500
512 x 512	15,000
512 x 384	19,800
256 x 256	39,500
256 x 128	72,000
256 x 64	125,000
256 x 8	300,000

Short Description

The v640 provides a 4 megapixel sensor and greater than 6 gigapixel/second throughput. That means full-resolution frame rates of over 1500 frames-per-second (fps), and 1920 x 1080 HD-resolution frame rates of over 2700 fps.

Throughput/Speed

Max speed at full resolution of 2560 x 1600 is 1500 fps to RAM and 200 fps to CineMag
Max speed at reduced resolution of 128 x 8 is 300,000 fps to RAM
Min frame rate of 10 fps

Sensor Specifications

CMOS sensor 2560 x 1600 pixels
10 µm pixel size
25.6 mm x 16.0 mm
8- and 12-bit depth
ISO 4000 mono, 1000 color
TE cooled
CAR in 256 x 8 increments
Fill factor: 70%
Dynamic range: 55 dB
Read out noise at 45°C (typical): 21e-
QE at 530nm: 57%
Full well capacity (typical): 11500e-

Exposure

1us minimum exposure
Global electronic shutter
Extreme Dynamic Range (EDR)
Auto Exposure
Shutter Off mode for PIV

Memory

8 GB, 16 GB and 32 GB high-speed internal RAM
CineMag compatible (128 GB, 256 GB, 144 GB, 512 GB)

Record Times

3.7 seconds at maximum frame rate, maximum bit depth, largest resolution and into maximum internal memory

Special Features

Segment memory for up to 63 cines in multi-cine mode
Continuous recording
Frame rate profile
Memory gate
Event marking
Frame timestamp

IRIG in/out (modulated and unmodulated)
Shutter off mode for PIV exposure
1.2 µs straddle time
Burst mode
Standard internal mechanical shutter for automatic/remote Current Session Reference (CSR)
Secondary IP address
Field-based firmware upgrade capable

Triggering

Programmable trigger location (pre/post trigger recording)
Image-Based Auto-Trigger
Trigger from software
Hardware trigger BNC

Timing & Synchronization

20 ns timing resolution
Frame synchronization to internal or external clock (FSYNC)
IRIG in/out (modulated or unmodulated)
Ready output
Strobe output

Signaling

Break-out-Box (IRIG-in, IRIG-out, NTSC/PAL Video, Trigger, Event, Strobe, A-Sync, Pre-Trigger/Memgate, Ready, Power In, GenLock)
Dedicated FSYNC, Trigger BNCs on camera body
Range Data input on camera body (Fischer)

Ethernet Connection

Gb Ethernet for both control and data

Camera Control

Phantom Camera Control (PCC)
Remote Control Unit (RCU), connects to Break-out-Box
Phantom Application (legacy)
SDK available

Video Out

Analog video (NTSC or PAL) available on Break-out-Box

Component viewfinder port
Versatile Dual HD-SDI can provide 4:4:4 video (except at 60 fps), or can be two single 4:2:2 HD-SDI ports, one for playback and one always live

Lensing

Nikon F-mount standard
Canon EOS mount optional
PL-mount optional
C-mount optional
(lens not included)

Video Processing

Selectable auto-scaling of 2560 x 1440 to 1920 x 1080 or 1280 x 720 on video out
Brightness
Gain
Gamma
Saturation
Hue
White Balance
Color interpolation algorith
Filters
Color matrix
Image flip and rotate
Crop
Scale

Data Acquisition

National Instruments M- and X-Series DAQ modules with integrated support in PCC

Motion Analysis

Basic measurements via Phantom Application:
Distance
Speed
Acceleration
Angles and Angular Speed
Compatible with 3rd party solutions

Supported File Formats

Cine, Cine Compressed, Cine RAW, AVI, Multipage TIFF, MXF PAL, MXF NTSC, QuickTime, Windows BMP, OS/2 BMP, PCX, TGA, TIFF, LEAD, JPEG, JTIF, RAW, DNG, DPX, h.264 mp4

Power

100 - 240 VAC, 120 Watt power supply included
20 - 36 VDC battery input via Break-out-Box

Mechanical Specifications

12.25 x 5.5 x 5.0 in (L, W, H)
31.1 x 14 x 12.7 cm
Weight: 12 lbs, 5.4 Kg

Environmental Specifications

Temperature and Humidity: 0°C - 40°C @ 8% to 80% RH
Shock: 30G, half sine wave, 11 ms, 10 times all axes (without CineMag or lens)
Vibration: 0.25G, 5-500 Hz, all axes without CineMag

Bubble Dynamics Processing Matlab code

Matlab code for bubble image processing:

```
clear all
%prefix =
'd:\bubbles2010\\w_060306_02p489s_y48p0_zm01p50_02\images_';
prefix = 'F:\8%M\image0';
%prefix =
'C:\bubbles2010\Calibration_060308\shadow_080306_p5_ra';

ext = '.bmp';
ext_out = 'bubbles_a.txt';

FirstIm = input('Please enter the number of the first image in pairs
(FirstIm =?):  ');
go_on = 'Y';
i= 0;


while go_on == 'Y' | go_on == 'y'
  i = i+1;
  ii = FirstIm+(i-1)*2;
```

```
  disp('The present image number: ')
  ii
  filename = strcat(prefix,num2str(ii, '%03g'), ext);
  %filename = strcat(prefix,num2str(ii, '%02g'), ext);
  image = imread(filename, 'bmp');
  BW = im2bw(255-image);
  disp('Click on bubble of interest');
%   imageq1 = image(1:600,1:800);
%   imageq2 = image(1:600,801:1600);
%   imageq3 = image(601:1200, 1:800);
%   imageq4 = image(601:1200, 801:1600);
%   imageq = [imageq1 imageq2; imageq3 imageq4];
  xy = [];
  n=0;
  disp('Left mouse button picks bubbles.');
  disp('Right mouse button picks last bubble.');
  for qk1 = 0:1
     for qk2 = 0:1
        image_show = image(qk1*300+1:(qk1+1)*300,
qk2*800+1:(qk2+1)*800);
        figure(1), imshow(image_show);
  %imshow(image);
        hold on;

       but =1;
      while but == 1
          figure(1);
          [xi, yi, but] = ginput(1);
     %find bubble boundary and then calculate the center and raduis
     %plot the boundaries
          xc = fix(xi)+qk2*800-1;
          yc = fix(yi)+qk1*600-1;
          while BW(yc, xc)
              yc = yc-1;
          end
          yc = yc+1;
          boundary = bwtraceboundary(BW, [yc, xc],'N');
         if (~isempty(boundary))
              hold on;
              boundary(:,2) = boundary(:,2)-qk2*800+1;
              boundary(:,1) = boundary(:,1)-qk1*600+1;
              [x0_c, y0_c, r0] = compute_circle(boundary);
              x0 = x0_c+qk1*600-1;
              y0 = y0_c+qk2*800-1;
              r = fix(r0*1.2);
              if (x0-r<2 | y0-r<2 | y0+r>1630 |x0 +r >1198)
```

```
                    disp('The bubble is too close to the image edge. It is not
collected');
                else
                plot(boundary(:,2), boundary(:,1),'g');
                draw_circ(x0_c, y0_c, r0);
                aa = fitting_tanh(x0,y0,r0, image);
                xc = aa(1);
                yc = aa(2);
                rad = aa(3);
                gray = aa(4);
                beta = aa(5);
                n = n+1;
%            reply = input('Do you want to check the tanh function fitting?
Y/N [N]: ', 's');
%            if isempty(reply)
%                reply = 'N';
%            end
%            if reply == 'Y' | reply =='y'
%                f = plot_tanh_fitting(x0,y0, r0, image);
%            end
                bubble_result(:,n) = [xc;yc;rad;gray;beta];
                end
            end
        end
        hold off;
      end
  end

  out_filename = strcat(prefix,num2str(ii, '%03g'), ext_out);
 % bubble_result = final_bubble_result(bubble_result);
  bubble_result = bubble_result';
  save(out_filename, 'bubble_result', '-ascii');
  clear bubble_result;
%    xc1 = fix(xy(2,:));
%    yc1 = fix(xy(1,:));
%
%    for j=1:n
%        intnsty = 255-image(yc1(j),xc1(j))
%        bound = intnsty/2.;
%    end
go_on = input('Do you want to process next image? Y/N [Y]: ', 's');
if isempty(go_on)
  go_on = 'Y';
end
end
```

References

[1] Eastman, J. A., Phillpot, S. R., Choi, S. U. S., and Keblinski, P., 2004, "Thermal transport in nanofluids," Annual Review of Materials Research, 34, pp. 219-246.
[2] Eastman, L. J., Choi, S. U. S., LI, S., and Thompson, L. J., 1997, "Enhanced thermal conductivity through development of nanofluids,"Nanocrystalline and Nanocomposite Materials II.
[3] Inaba, H., 2000, "New challenge in advanced thermal energy transportation using functionally thermal fluids," International Journal of Thermal Sciences, 39(9-11), pp. 991-1003.
[4] Buongiorno, J., Venerus, D. C., Prabhat, N., McKrell, T., Townsend, J., Christianson, R., Tolmachev, Y. V., Keblinski, P., Hu, L.-w., Alvarado, J. L., Bang, I. C., Bishnoi, S. W., Bonetti, M., Botz, F., Cecere, A., Chang, Y., Chen, G., Chen, H., Chung, S. J., Chyu, M. K., Das, S. K., Di Paola, R., Ding, Y., Dubois, F., Dzido, G., Eapen, J., Escher, W., Funfschilling, D., Galand, Q., Gao, J., Gharagozloo, P. E., Goodson, K. E., Gutierrez, J. G., Hong, H., Horton, M., Hwang, K. S., Iorio, C. S., Jang, S. P., Jarzebski, A. B., Jiang, Y., Jin, L., Kabelac, S., Kamath, A., Kedzierski, M. A., Kieng, L. G., Kim, C., Kim, J.-H., Kim, S., Lee, S. H., Leong, K. C., Manna, I., Michel, B., Ni, R., Patel, H. E., Philip, J., Poulikakos, D., Reynaud, C., Savino, R., Singh, P. K., Song, P., Sundararajan, T., Timofeeva, E., Tritcak, T., Turanov, A. N., Van Vaerenbergh, S., Wen, D., Witharana, S., Yang, C., Yeh, W.-H., Zhao, X.-Z., and Zhou, S.-Q., 2009, "A benchmark study on the thermal conductivity of nanofluids," Journal of Applied Physics, 106(9).
[5] Zimparov, V., 2002, "Energy conservation through heat transfer enhancement techniques," International Journal of Energy Research, 26(7), pp. 675-696.
[6] Dewan, A., Mahanta, P., Raju, K. S., and Kumar, P. S., 2004, "Review of passive heat transfer augmentation techniques," Proceedings of the Institution of Mechanical Engineers Part a-Journal of Power and Energy, 218(A7), pp. 509-527.
[7] Boyd, R. D., 1985, "SUBCOOLED FLOW BOILING CRITICAL HEAT-FLUX (CHF) AND ITS APPLICATION TO FUSION ENERGY COMPONENTS .1. A REVIEW OF FUNDAMENTALS OF CHF AND RELATED DATA-BASE," Fusion Technology, 7(1), pp. 7-30.
[8] Choi, S. U. S., Zhang, Z. G., Yu, W., Lockwood, F. E., and Grulke, E. A., 2001, "Anomalous thermal conductivity enhancement in nanotube suspensions," Applied Physics Letters, 79(14), pp. 2252-2254.
[9] Xu, J. J., Wu, C. W., and Yang, B., 2010, "Thermal- and Phase-Change Characteristics of Self-Assembled Ethanol/Polyalphaolefin Nanoemulsion Fluids," Journal of Thermophysics and Heat Transfer, 24(1), pp. 208-211.
[10] Xu, J., Yang, B., and Hammouda, B., 2011, "Thermal conductivity and viscosity of self-assembled alcohol/polyalphaolefin nanoemulsion fluids," Nanoscale Research Letters, 6.
[11] Xu, J., Hammouda, B., and Yang, B., **2012**, "Thermophysical Properties and Pool Boiling Characteristics of Water in Polyalphaolefin Nanoemulsion Fluids," ASME, Proceedings of ASME Micro/Nanoscale Heat & Mass Transfer International Conference 2012.
[12] Xu, J., and Yang, B., 2012, "Novel Heat Transfer Fluids: Self-assembled Nanoemulsion Fluids," NANTOTECHNOLOGY, D. J. N. Govil, ed., Studium Press LLC.

[13] Yang, B., and Han, Z. H., 2006, "Thermal conductivity enhancement in water-in-FC72 nanoemulsion fluids," Applied Physics Letters, 88(26).
[14] Han, Z. H., Cao, F. Y., and Yang, B., 2008, "Synthesis and thermal characterization of phase-changeable indium/polyalphaolefin nanofluids," Applied Physics Letters, 92(24).
[15] Han, Z. H., and Yang, B., 2008, "Thermophysical characteristics of water-in-FC72 nanoemulsion fluids," Applied Physics Letters, 92(1).
[16] Han, Z. H., Yang, B., Qi, Y., and Cumings, J., 2011, "Synthesis of low-melting-point metallic nanoparticles with an ultrasonic nanoemulsion method," Ultrasonics, 51(4), pp. 485-488.
[17] Thome, J. R., 2006, "The new frontier in heat transfer: Microscale and nanoscale technologies," Heat Transfer Engineering, 27(9), pp. 1-3.
[18] Tuckerman, D. B., and Pease, R. F. W., 1981, "HIGH-PERFORMANCE HEAT SINKING FOR VLSI," Electron Device Letters, 2(5), pp. 126-129.
[19] Kandlikar, S. G., and Grande, W. J., 2004, "Evaluation of single phase flow in microchannels for high heat flux chip cooling - Thermohydraulic performance enhancement and fabrication technology," Heat Transfer Engineering, 25(8), pp. 5-16.
[20] Agostini, B., Fabbri, M., Park, J. E., Wojtan, L., Thome, J. R., and Michel, B., 2007, "State of the art of high heat flux cooling technologies," Heat Transfer Engineering, 28(4), pp. 258-281.
[21] Zhang, H., Mudawar, I., and Hasan, M. M., 2007, "Assessment of dimensionless CHF correlations for subcooled flow boiling in microgravity and earth gravity," International Journal of Heat and Mass Transfer, 50(23-24), pp. 4568-4580.
[22] Sung, M. K., and Mudawar, I., 2009, "CHF determination for high-heat flux phase change cooling system incorporating both micro-channel flow and jet impingement," International Journal of Heat and Mass Transfer, 52(3-4), pp. 610-619.
[23] Maxwell, J. C., 1904, "A treatise on electricity and magnetism," Oxford University Press, Cambridge, UK.
[24] Eastman, J. A., Choi, S. U. S., Li, S., Yu, W., and Thompson, L. J., 2001, "Anomalously increased effective thermal conductivities of ethylene glycol-based nanofluids containing copper nanoparticles," Applied Physics Letters, 78(6), pp. 718-720.
[25] Keblinski, P., Phillpot, S. R., Choi, S. U. S., and Eastman, J. A., 2002, "Mechanisms of heat flow in suspensions of nano-sized particles (nanofluids)," International Journal of Heat and Mass Transfer, 45(4), pp. 855-863.
[26] Das, S. K., Putra, N., Thiesen, P., and Roetzel, W., 2003, "Temperature dependence of thermal conductivity enhancement for nanofluids," Journal of Heat Transfer-Transactions of the Asme, 125(4), pp. 567-574.
[27] Xuan, Y. M., and Li, Q., 2003, "Investigation on convective heat transfer and flow features of nanofluids," Journal of Heat Transfer-Transactions of the Asme, 125(1), pp. 151-155.
[28] Wen, D. S., and Ding, Y. L., 2004, "Effective thermal conductivity of aqueous suspensions of carbon nanotubes (carbon nanotubes nanofluids)," Journal of Thermophysics and Heat Transfer, 18(4), pp. 481-485.
[29] Wen, D. S., and Ding, Y. L., 2004, "Experimental investigation into convective heat transfer of nanofluids at the entrance region under laminar flow conditions," International Journal of Heat and Mass Transfer, 47(24), pp. 5181-5188.
[30] Hong, T., Yang, H., and Choi, C. J., 2005, "Study of the enhanced thermal conductivity of Fe nanofluids," Journal of Applied Physics, 97(6), pp. 64311-64311-64314.
[31] Yang, Y., Zhang, Z. G., Grulke, E. A., Anderson, W. B., and Wu, G. F., 2005, "Heat transfer properties of nanoparticle-in-fluid dispersions (nanofluids) in larninar flow," International Journal of Heat and Mass Transfer, 48(6), pp. 1107-1116.

[32] Ding, Y. L., Alias, H., Wen, D. S., and Williams, R. A., 2006, "Heat transfer of aqueous suspensions of carbon nanotubes (CNT nanofluids)," International Journal of Heat and Mass Transfer, 49(1-2), pp. 240-250.
[33] Heris, S. Z., Etemad, S. G., and Esfahany, A. N., 2006, "Experimental investigation of oxide nanofluids laminar flow convective heat transfer," International Communications in Heat and Mass Transfer, 33(4), pp. 529-535.
[34] Kim, S. J., Bang, I. C., Buongiorno, J., and Hu, L. W., 2006, "Effects of nanoparticle deposition on surface wettability influencing boiling heat transfer in nanofluids," Applied Physics Letters, 89(15).
[35] Li, C. H., and Peterson, G. P., 2006, "Experimental investigation of temperature and volume fraction variations on the effective thermal conductivity of nanoparticle suspensions (nanofluids)," Journal of Applied Physics, 99(8).
[36] Ma, H. B., Wilson, C., Borgmeyer, B., Park, K., Yu, Q., Choi, S. U. S., and Tirumala, M., 2006, "Effect of nanofluid on the heat transport capability in an oscillating heat pipe," Applied Physics Letters, 88(14).
[37] Prasher, R., Evans, W., Meakin, P., Fish, J., Phelan, P., and Keblinski, P., 2006, "Effect of aggregation on thermal conduction in colloidal nanofluids," Applied Physics Letters, 89(14).
[38] Prasher, R., Song, D., Wang, J. L., and Phelan, P., 2006, "Measurements of nanofluid viscosity and its implications for thermal applications," Applied Physics Letters, 89(13).
[39] Yang, B., and Han, Z. H., 2006, "Temperature-dependent thermal conductivity of nanorod-based nanofluids," Applied Physics Letters, 89(8).
[40] Chein, R., and Chuang, J., 2007, "Experimental microchannel heat sink performance studies using nanofluids," International Journal of Thermal Sciences, 46(1), pp. 57-66.
[41] Han, Z. H., Yang, B., Kim, S. H., and Zachariah, M. R., 2007, "Application of hybrid sphere/carbon nanotube particles in nanofluids," Nanotechnology, 18(10).
[42] Khodadadi, J. M., and Hosseinizadeh, S. F., 2007, "Nanoparticle-enhanced phase change materials (NEPCM) with great potential for improved thermal energy storage," Int. Commun. Heat Mass Transf., 34(5), pp. 534-543.
[43] Kim, S. J., Bang, I. C., Buongiorno, J., and Hu, L. W., 2007, "Surface wettability change during pool boiling of nanofluids and its effect on critical heat flux," International Journal of Heat and Mass Transfer, 50(19-20), pp. 4105-4116.
[44] Lee, J., and Mudawar, I., 2007, "Assessment of the effectiveness of nanofluids for single-phase and two-phase heat transfer in micro-channels," International Journal of Heat and Mass Transfer, 50(3-4), pp. 452-463.
[45] Trisaksri, V., and Wongwises, S., 2007, "Critical review of heat transfer characteristics of nanofluids," Renewable & Sustainable Energy Reviews, 11(3), pp. 512-523.
[46] Wang, X.-Q., and Mujumdar, A. S., 2007, "Heat transfer characteristics of nanofluids: a review," International Journal of Thermal Sciences, 46(1), pp. 1-19.
[47] Liu, Z.-h., and Liao, L., 2008, "Sorption and agglutination phenomenon of nanofluids on a plain heating surface during pool boiling," International Journal of Heat and Mass Transfer, 51(9-10), pp. 2593-2602.
[48] Milanova, D., and Kumar, R., 2008, "Heat transfer behavior of silica nanoparticles experiment in pool boiling," Journal of Heat Transfer-Transactions of the Asme, 130(4).
[49] Wang, X. Q., and Mujumdar, A. S., 2008, "A REVIEW ON NANOFLUIDS - PART I: THEORETICAL AND NUMERICAL INVESTIGATIONS," Brazilian Journal of Chemical Engineering, 25(4), pp. 613-630.
[50] Wang, X. Q., and Mujumdar, A. S., 2008, "A REVIEW ON NANOFLUIDS - PART II: EXPERIMENTS AND APPLICATIONS," Brazilian Journal of Chemical Engineering, 25(4), pp. 631-648.

[51] Wen, D., 2008, "Mechanisms of thermal nanofluids on enhanced critical heat flux (CHF)," International Journal of Heat and Mass Transfer, 51(19-20), pp. 4958-4965.
[52] Yang, B., 2008, "Thermal conductivity equations based on Brownian motion in suspensions of nanoparticles (nanofluids)," Journal of Heat Transfer-Transactions of the Asme, 130(4).
[53] Ozerinc, S., Kakac, S., and Yazicioglu, A. G., 2010, "Enhanced thermal conductivity of nanofluids: a state-of-the-art review," Microfluidics and Nanofluidics, 8(2), pp. 145-170.
[54] Kim, S. J., McKrell, T., Buongiorno, J., and Hu, L.-W., 2009, "Experimental Study of Flow Critical Heat Flux in Alumina-Water, Zinc-Oxide-Water, and Diamond-Water Nanofluids," Journal of Heat Transfer-Transactions of the Asme, 131(4).
[55] Shima, P. D., Philip, J., and Raj, B., 2010, "Synthesis of Aqueous and Nonaqueous Iron Oxide Nanofluids and Study of Temperature Dependence on Thermal Conductivity and Viscosity," Journal of Physical Chemistry C, 114(44), pp. 18825-18833.
[56] Kim, H., 2011, "Enhancement of critical heat flux in nucleate boiling of nanofluids: a state-of-art review," Nanoscale Research Letters, 6.
[57] Rana, P., and Bhargava, R., 2011, "Numerical study of heat transfer enhancement in mixed convection flow along a vertical plate with heat source/sink utilizing nanofluids," Communications in Nonlinear Science and Numerical Simulation, 16(11), pp. 4318-4334.
[58] Barber, J., Brutin, D., and Tadrist, L., 2011, "A review on boiling heat transfer enhancement with nanofluids," Nanoscale Research Letters, 6.
[59] Sohel Murshed, S. M., Nieto de Castro, C. A., Lourenco, M. J. V., Lopes, M. L. M., and Santos, F. J. V., 2011, "A review of boiling and convective heat transfer with nanofluids," Renewable & Sustainable Energy Reviews, 15(5), pp. 2342-2354.
[60] Sergis, A., and Hardalupas, Y., 2011, "Anomalous heat transfer modes of nanofluids: a review based on statistical analysis," Nanoscale Research Letters, 6.
[61] Ahn, H. S., and Kim, M. H., 2012, "A Review on Critical Heat Flux Enhancement With Nanofluids and Surface Modification," Journal of Heat Transfer-Transactions of the Asme, 134(2).
[62] Kim, S. J., McKrell, T., Buongiorno, J., and Hu, L.-W., 2008, "Alumina nanoparticles enhance the flow boiling critical heat flux of water at low pressure," Journal of Heat Transfer-Transactions of the Asme, 130(4).
[63] Shima, P. D., Philip, J., and Raj, B., 2009, "Magnetically controllable nanofluid with tunable thermal conductivity and viscosity," Applied Physics Letters, 95(13).
[64] Philip, J., and Shima, P. D., 2012, "Thermal properties of nanofluids," Advances in Colloid and Interface Science, 183, pp. 30-45.
[65] Pak, B. C., and Cho, Y. I., 1998, "Hydrodynamic and heat transfer study of dispersed fluids with submicron metallic oxide particles," Experimental Heat Transfer, 11(2), pp. 151-170.
[66] Coursey, J. S., and Kim, J., 2008, "Nanofluid boiling: The effect of surface wettability," International Journal of Heat and Fluid Flow, 29(6), pp. 1577-1585.
[67] Jeong, Y. H., Chang, W. J., and Chang, S. H., 2008, "Wettability of heated surfaces under pool boiling using surfactant solutions and nano-fluids," International Journal of Heat and Mass Transfer, 51(11-12), pp. 3025-3031.
[68] Eapen, J., Li, J., and Yip, S., 2007, "Mechanism of thermal transport in dilute nanocolloids," Physical Review Letters, 98(2).
[69] Younes, H., Christensen, G., Luan, X., Hong, H., and Smith, P., 2012, "Effects of alignment, pH, surfactant, and solvent on heat transfer nanofluids containing Fe2O3 and CuO nanoparticles," Journal of Applied Physics, 111(6).
[70] Angayarkanni, S. A., and Philip, J., 2012, "Role of surface charge, morphology, and adsorbed moieties on thermal conductivity enhancement of nanofluids," Applied Physics Letters, 101(17).

[71] Bulanov, N. V., Skripov, V. P., and Khmylnin, V. A., 1984, "Heat Transfer to Emulsion with superheating of its disperse phase,"J. Eng. Phys.,, pp. 1-3.
[72] Bulanov, N. V., Skripov, V. P., and Khmylnin, V. A., 1993, "Heat Transfer to Emulsion with a low-boiling disperse phase,"Heat Transfer Res, pp. 786-789.
[73] Bulanov, N. V., 2001, "An analysis of the heat flux density under conditions of boiling internal phase of emulsion," High Temperature, 39(3), pp. 462-469.
[74] Bulanov, N. V., and Gasanov, B. M., 2005, "Experimental setup for studying the chain activation of low-temperature boiling sites in superheated liquid droplets," Colloid Journal, 67(5), pp. 531-536.
[75] Bulanov, N. V., Gasanov, B. M., and Turchaninova, E. A., 2006, "Results of experimental investigation of heat transfer with emulsions with low-boiling disperse phase," High Temperature, 44(2), pp. 267-282.
[76] Bulanov, N. V., and Gasanov, B. M., 2008, "Peculiarities of boiling of emulsions with a low-boiling disperse phase," International Journal of Heat and Mass Transfer, 51(7-8), pp. 1628-1632.
[77] Mori, Y. H., Inui, E., and Komotori, K., 1978, "POOL BOILING HEAT-TRANSFER TO EMULSIONS," Journal of Heat Transfer-Transactions of the Asme, 100(4), pp. 613-617.
[78] Roesle, M. L., and Kulacki, F. A., 2010, "Boiling of Dilute Emulsions-Toward a New Modeling Framework," Industrial & Engineering Chemistry Research, 49(11), pp. 5188-5196.
[79] Mills, A. F., 1999, Basic heat and mass transfer, Prentice Hall, Inc., New Jersey.
[80] Sharma, S., Kitano, H., and Sagara, K., 2004, "Phase Change Materials for Low Temperature Solar Thermal Applications " Res. Rep. Fac. Eng. Mie Univ., 29, pp. 31-64.
[81] Osterman, E., Tyagi, V. V., Butala, V., Rahim, N. A., and Stritih, U., 2012, "Review of PCM based cooling technologies for buildings," Energy Build., 49, pp. 37-49.
[82] Chen, S. J., Evans, D. F., and Ninham, B. W., 1984, "PROPERTIES AND STRUCTURE OF 3-COMPONENT IONIC MICROEMULSIONS," Journal of Physical Chemistry, 88(8), pp. 1631-1634.
[83] Ruckenstein, E., 1986, "THE SURFACE OF TENSION, THE NATURAL RADIUS, AND THE INTERFACIAL-TENSION IN THE THERMODYNAMICS OF MICROEMULSIONS," Journal of Colloid and Interface Science, 114(1), pp. 173-179.
[84] Siano, D. B., Bock, J., Myer, P., and Russel, W. B., 1987, "THERMODYNAMICS AND HYDRODYNAMICS OF A NONIONIC MICROEMULSION," Colloids and Surfaces, 26, pp. 171-190.
[85] Chen, Z. Q., Chen, L. D., Hao, C., and Zhang, C. Z., 1990, "THERMODYNAMICS OF MICROEMULSION .1. THE EFFECT OF ALKYL CHAIN-LENGTH OF ALKYL AROMATICS," Acta Chimica Sinica, 48(6), pp. 528-533.
[86] Moulik, S. P., Das, M. L., Bhattacharya, P. K., and Das, A. R., 1992, "THERMODYNAMICS OF MICROEMULSION FORMATION .1. ENTHALPY OF SOLUTION OF WATER IN BINARY (TRITON-X 100 + BUTANOL) AND TERNARY (HEPTANE + TRITON-X 100 + BUTANOL) MIXTURES AND HEAT-CAPACITY OF THE RESULTING SYSTEMS," Langmuir, 8(9), pp. 2135-2139.
[87] Moulik, S. P., and Ray, S., 1994, "THERMODYNAMICS OF CLUSTERING OF DROPLETS IN WATER/AOT/HEPTANE MICROEMULSION," Pure and Applied Chemistry, 66(3), pp. 521-525.
[88] Ray, S., Bisal, S. R., and Moulik, S. P., 1994, "THERMODYNAMICS OF MICROEMULSION FORMATION .2. ENTHALPY OF SOLUTION OF WATER IN BINARY-MIXTURES OF AEROSOL-OT AND HEPTANE AND HEAT-CAPACITY OF THE RESULTING SYSTEMS," Langmuir, 10(8), pp. 2507-2510.
[89] Strey, R., 1994, "MICROEMULSION MICROSTRUCTURE AND INTERFACIAL CURVATURE," Colloid and Polymer Science, 272(8), pp. 1005-1019.

[90] Bergenholtz, J., Romagnoli, A. A., and Wagner, N. J., 1995, "VISCOSITY, MICROSTRUCTURE, AND INTERPARTICLE POTENTIAL OF AOT/H2O/N-DECANE INVERSE MICROEMULSIONS," Langmuir, 11(5), pp. 1559-1570.
[91] Mukherjee, K., Mukherjee, D. C., and Moulik, S. P., 1997, "Thermodynamics of microemulsion formation .3. Enthalpies of solution of water in chloroform as well as chloroform in water aided by cationic, anionic, and nonionic surfactants," Journal of Colloid and Interface Science, 187(2), pp. 327-333.
[92] Kumar, P., and Mittal, K. L., 1999, Handbook of microemulsion science and technology, New York: Marcel Dekker.
[93] Talegaonkar, S., Azeem, A., Ahmad, F. J., Khar, R. K., Pathan, S. A., and Khan, Z. I., 2008, "Microemulsions: a novel approach to enhanced drug delivery," Recent patents on drug delivery & formulation, 2(3), pp. 238-257.
[94] Haque, O., and Scamehorn, J. F., 1986, "THERMODYNAMICS OF MICROEMULSION FORMATION BY MIXTURES OF ANIONIC AND NONIONIC SURFACTANTS," Journal of Dispersion Science and Technology, 7(2), pp. 129-157.
[95] De, M., Bhattacharya, S. C., Panda, A. K., and Moulik, S. P., 2009, "Interfacial Behavior, Structure, and Thermodynamics of Water in Oil Microemulsion Formation in Relation to the Variation of Surfactant Head Group and Cosurfactant," Journal of Dispersion Science and Technology, 30(9), pp. 1262-1272.
[96] 1983, "THERMAL-ANALYSIS AND CONTROL OF ELECTRONIC EQUIPMENT - KRAUS,AD, BARCOHEN,A," Solid State Technology, 26(8), pp. 282-282.
[97] Zuber, N., 1957, "ON THE CORRELATION OF DATA IN NUCLEATE POOL BOILING FROM A HORIZONTAL SURFACE," Aiche Journal, 3(3), pp. S9-S11.
[98] Dhir, V. K., 1998, "Boiling heat transfer," Annual Review of Fluid Mechanics, 30, pp. 365-401.
[99] Barthau, G., 1992, "ACTIVE NUCLEATION SITE DENSITY AND POOL BOILING HEAT-TRANSFER - AN EXPERIMENTAL-STUDY," International Journal of Heat and Mass Transfer, 35(2), pp. 271-278.
[100] Wang, C. H., and Dhir, V. K., 1993, "EFFECT OF SURFACE WETTABILITY ON ACTIVE NUCLEATION SITE DENSITY DURING POOL BOILING OF WATER ON A VERTICAL SURFACE," Journal of Heat Transfer-Transactions of the Asme, 115(3), pp. 659-669.
[101] Basu, N., Warrier, G. R., and Dhir, V. K., 2002, "Onset of nucleate boiling and active nucleation site density during subcooled flow boiling," Journal of Heat Transfer-Transactions of the Asme, 124(4), pp. 717-728.
[102] Wasekar, V. M., and Manglik, R. M., 1999, "A review of enhanced heat transfer in nucleate pool boiling of aqueous surfactant and polymeric solutions," Journal of Enhanced Heat Transfer, 6(2-4), pp. 135-150.
[103] Wu, W. T., Yang, Y. M., and Maa, J. R., 1998, "Effect of surfactant additive on pool boiling of concentrated lithium bromide solution," International Communications in Heat and Mass Transfer, 25(8), pp. 1127-1134.
[104] Hetsroni, G., Zakin, J. L., Lin, Z., Mosyak, A., Pancallo, E. A., and Rozenblit, R., 2001, "The effect of surfactants on bubble growth, wall thermal patterns and heat transfer in pool boiling," International Journal of Heat and Mass Transfer, 44(2), pp. 485-497.
[105] Manglik, R. M., Wasekar, V. M., and Zhang, J. T., 2001, "Dynamic and equilibrium surface tension of aqueous surfactant and polymeric solutions," Experimental Thermal and Fluid Science, 25(1-2), pp. 55-64.
[106] Wasekar, V. M., and Manglik, R. M., 2002, "The influence of additive molecular weight and ionic nature on the pool boiling performance of aqueous surfactant solutions," International Journal of Heat and Mass Transfer, 45(3), pp. 483-493.

[107] Prosperetti, A., and Plesset, M. S., 1978, "VAPOR-BUBBLE GROWTH IN A SUPERHEATED LIQUID," Journal of Fluid Mechanics, 85(MAR), pp. 349-368.
[108] Barry, B. W., and Wilson, R., 1978, "CMC COUNTERION BINDING AND THERMODYNAMICS OF ETHOXYLATED ANIONIC AND CATIONIC SURFACTANTS," Colloid and Polymer Science, 256(3), pp. 251-260.
[109] Kotchaph.P, and Williams, M. C., 1970, "ENHANCEMENT OF NUCLEATE POOL BOILING WITH POLYMERIC ADDITIVES," International Journal of Heat and Mass Transfer, 13(5), pp. 835-&.
[110] Shulman, Z. P., and Levitskiy, S. P., 1996, "Growth of vapour bubbles in boiling polymer solutions .1. Rheological and diffusional effects," International Journal of Heat and Mass Transfer, 39(3), pp. 631-638.
[111] Fainerman, V. B., Makievski, A. V., and Miller, R., 1993, "THE MEASUREMENT OF DYNAMIC SURFACE TENSIONS OF HIGHLY VISCOUS-LIQUIDS BY THE MAXIMUM BUBBLE PRESSURE METHOD," Colloids and Surfaces a-Physicochemical and Engineering Aspects, 75, pp. 229-235.
[112] Persson, B., Nilsson, S., and Sundelof, L. O., 1996, "On the characterization principles of some technically important water-soluble nonionic cellulose derivatives .2. Surface tension and interaction with a surfactant," Carbohydrate Polymers, 29(2), pp. 119-127.
[113] Shafiq-un-Nabi, S., Shakeel, F., Talegaonkar, S., Ali, J., Baboota, S., Ahuja, A., Khar, R. K., and Ali, M., 2007, "Formulation development and optimization using nanoemulsion technique: A technical note," Aaps Pharmscitech, 8(2).
[114] Moulik, S. P., and Paul, B. K., 1998, "Structure, dynamics and transport properties of microemulsions," Advances in Colloid and Interface Science, 78(2), pp. 99-195.
[115] Chen, S. H., 1986, "SMALL-ANGLE NEUTRON-SCATTERING STUDIES OF THE STRUCTURE AND INTERACTION IN MICELLAR AND MICROEMULSION SYSTEMS," Annual Review of Physical Chemistry, 37, pp. 351-399.
[116] Smith, R. D., Blitz, J. P., and Fulton, J. L., 1989, "STRUCTURE OF REVERSE MICELLE AND MICROEMULSION PHASES IN NEAR-CRITICAL AND SUPERCRITICAL FLUID AS DETERMINED FROM DYNAMIC LIGHT-SCATTERING-STUDIES," Acs Symposium Series, 406, pp. 165-183.
[117] Hirai, M., Kawaihirai, R., Yabuki, S., Takizawa, T., Hirai, T., Kobayashi, K., Amemiya, Y., and Oya, M., 1995, "AEROSOL-OT REVERSED MICELLAR FORMATION AT LOW WATER-SURFACTANT RATIO STUDIED BY SYNCHROTRON-RADIATION SMALL-ANGLE X-RAY-SCATTERING," Journal of Physical Chemistry, 99(17), pp. 6652-6660.
[118] Soderman, O., and Nyden, M., 1999, "NMR in microemulsions. NMR translational diffusion studies of a model microemulsion," Colloids and Surfaces a-Physicochemical and Engineering Aspects, 158(1-2), pp. 273-280.
[119] Hirai, M., Hirai, R. K., Iwase, H., Arai, S., Mitsuya, S., Takeda, T., Seto, H., and Nagao, M., 1999, "Dynamics of w/o AOT microemulsions studied by neutron spin echo," Journal of Physics and Chemistry of Solids, 60(8-9), pp. 1359-1361.
[120] Koper, G. J. M., Sager, W. F. C., Smeets, J., and Bedeaux, D., 1995, "AGGREGATION IN OIL-CONTINUOUS WATER SODIUM BIS(2-ETHYLHEXYL)SULFOSUCCINATE OIL MICROEMULSIONS," Journal of Physical Chemistry, 99(35), pp. 13291-13300.
[121] Eicke, H. F., and Shepherd, J. C., 1974, "DIELECTRIC PROPERTIES OF APOLAR MICELLE SOLUTIONS CONTAINING SOLUBILIZED WATER," Helvetica Chimica Acta, 57(7), pp. 1951-1963.
[122] Sjoblom, J., Jonsson, B., Nylander, C., and Lundstrom, I., 1983, "SOME DIELECTRIC-PROPERTIES OF REVERSED MICELLAR SYSTEMS WITH DIFFERENT

ALKALICARBOXYLATES AND NORMAL-ALCOHOLS," Journal of Colloid and Interface Science, 96(2), pp. 504-516.
[123] Peyrelasse, J., and Boned, C., 1985, "STUDY OF THE STRUCTURE OF WATER AEROSOL OT DODECANE SYSTEMS BY TIME DOMAIN DIELECTRIC-SPECTROSCOPY," Journal of Physical Chemistry, 89(2), pp. 370-379.
[124] Vandijk, M. A., Joosten, J. G. H., Levine, Y. K., and Bedeaux, D., 1989, "DIELECTRIC STUDY OF TEMPERATURE-DEPENDENT AEROSOL OT/WATER ISOOCTANE MICROEMULSION STRUCTURE," Journal of Physical Chemistry, 93(6), pp. 2506-2512.
[125] Chen, H. M., and Schelly, Z. A., 1995, "LASER-INDUCED TRANSIENT ELECTRIC BIREFRINGENCE AND LIGHT-SCATTERING IN AEROSOL-OT/CCL4 REVERSE MICELLES," Langmuir, 11(3), pp. 758-763.
[126] Lisy, V., and Brutovsky, B., 2000, "Interpretation of static and dynamic neutron and light scattering from microemulsion droplets: Effects of shape fluctuations," Physical Review E, 61(4), pp. 4045-4053.
[127] de Geyer, A., Molle, B., Lartigue, C., Guillermo, A., and Farago, B., 2004, "Dynamics of caged microemulsion droplets: a neutron spin echo and dynamic light scattering study," Physica B-Condensed Matter, 350(1-3), pp. 200-203.
[128] Tomsic, M., Bester-Rogac, M., Jamnik, A., Kunz, W., Touraud, D., Bergmann, A., and Glatter, O., 2006, "Ternary systems of nonionic surfactant Brij 35, water and various simple alcohols: Structural investigations by small-angle X-ray scattering and dynamic light scattering," Journal of Colloid and Interface Science, 294(1), pp. 194-211.
[129] Marion, G., Graciaa, A., and Lachaise, J., 1988, "DYNAMIC INVESTIGATION OF A CONCENTRATED MIDDLE-PHASE MICROEMULSION FROM QUASI-ELASTIC LIGHT-SCATTERING," Journal of Physical Chemistry, 92(6), pp. 1553-1557.
[130] Waaler, D., Strand, K. A., Stromme, G., and Sikkeland, T., 1989, "DYNAMIC LIGHT-SCATTERING OBSERVATION OF DROPLET AGGREGATION IN A WINSOR TYPE W/O MICROEMULSION SYSTEM," Journal of Chemical Physics, 91(6), pp. 3360-3367.
[131] Hellweg, T., and von Klitzing, R., 2000, "Evidence for polymer-like structures in the single phase region of a dodecane/C12E5/water microemulsion: a dynamic light scattering study," Physica A, 283(3-4), pp. 349-358.
[132] Regev, O., Ezrahi, S., Aserin, A., Garti, N., Wachtel, E., Kaler, E. W., Khan, A., and Talmon, Y., 1996, "A study of the microstructure of a four-component nonionic microemulsion by cryo-TEM, NMR, SAXS, and SANS," Langmuir, 12(3), pp. 668-674.
[133] Vinson, P. K., Sheehan, J. G., Miller, W. G., Scriven, L. E., and Davis, H. T., 1991, "VIEWING MICROEMULSIONS WITH FREEZE-FRACTURE TRANSMISSION ELECTRON-MICROSCOPY," Journal of Physical Chemistry, 95(6), pp. 2546-2550.
[134] Belkoura, L., Stubenrauch, C., and Strey, R., 2004, "Freeze fracture direct imaging: A new freeze fracture method for specimen preparation in cryo-transmission electron microscopy," Langmuir, 20(11), pp. 4391-4399.
[135] Wolf, L., Hoffmann, H., Talmon, Y., Teshigawara, T., and Watanabe, K., 2010, "Cryo-TEM imaging of a novel microemulsion system of silicone oil with an anionic/nonionic surfactant mixture," Soft Matter, 6(21), pp. 5367-5374.
[136] Jahn, W., and Strey, R., 1988, "MICROSTRUCTURE OF MICROEMULSIONS BY FREEZE-FRACTURE ELECTRON-MICROSCOPY," Journal of Physical Chemistry, 92(8), pp. 2294-2301.
[137] Sakai, T., Kamogawa, K., Harusawa, F., Momozawa, N., Sakai, H., and Abe, M., 2001, "Direct observation of flocculation/coalescence of metastable oil droplets in surfactant-free oil/water emulsion by freeze-fracture electron microscopy," Langmuir, 17(2), pp. 255-259.

[138] Burauer, S., Belkoura, L., Stubenrauch, C., and Strey, R., 2003, "Bicontinuous microemulsions revisited: a new approach to freeze fracture electron microscopy (FFEM)," Colloids and Surfaces a-Physicochemical and Engineering Aspects, 228(1-3), pp. 159-170.
[139] Wellert, S., Karg, M., Imhof, H., Steppin, A., Altmann, H. J., Dolle, M., Richardt, A., Tiersch, B., Koetz, J., Lapp, A., and Hellweg, T., 2008, "Structure of biodiesel based bicontinuous microemulsions for environmentally compatible decontamination: A small angle neutron scattering and freeze fracture electron microscopy study," Journal of Colloid and Interface Science, 325(1), pp. 250-258.
[140] Touloukian, Y. S., Liley, P. E., and Saxena, S. C., 1970, "Thermal conductivity for nonmetallic liquids & gases," Washiongton: IFI/PLENUM, Thermophysical Properties of Matters.
[141] Cahill, D. G., 1990, "THERMAL-CONDUCTIVITY MEASUREMENT FROM 30-K TO 750-K - THE 3-OMEGA METHOD," Review of Scientific Instruments, 61(2), pp. 802-808.
[142] Nan, C. W., Birringer, R., Clarke, D. R., and Gleiter, H., 1997, "Effective thermal conductivity of particulate composites with interfacial thermal resistance," Journal of Applied Physics, 81(10), pp. 6692-6699.
[143] Chiesa, M., Garg, J., Kang, Y. T., and Chen, G., 2008, "Thermal conductivity and viscosity of water-in-oil nanoemulsions," Colloids and Surfaces a-Physicochemical and Engineering Aspects, 326(1-2), pp. 67-72.
[144] Wu, C., Cho, T. J., Xu, J., Lee, D., Yang, B., and Zachariah, M. R., 2010, "Effect of nanoparticle clustering on the effective thermal conductivity of concentrated silica colloids," Physical Review E, 81(1).
[145] Batra, U., Russel, W. B., and Huang, J. S., 1999, "Viscosity anomaly and charge fluctuations in dilute AOT microemulsions with X < 20," Langmuir, 15(11), pp. 3718-3725.
[146] Incropera, F. P., DeWitt, D. P., Bergman, T. L., and Lavine, A. S., 2001, "Fundamentals of Heat and Mass Transfer," Wiley, p. 944.
[147] Hammouda, B., Krueger, S., and Glinka, C. J., 1993, "SMALL-ANGLE NEUTRON-SCATTERING AT THE NATIONAL-INSTITUTE-OF-STANDARDS-AND-TECHNOLOGY," Journal of Research of the National Institute of Standards and Technology, 98(1), pp. 31-46.
[148] Hammouda, B., 2010, "SANS from Polymers-Review of the Recent Literature," Polymer Reviews, 50(1), pp. 14-39.
[149] Batchelor , G. K., 1967, "An Introduction to Fluid Dynamics," Cambridge University Press.
[150] Park, H. C., Byun, K. T., and Kwak, H. Y., 2005, "Explosive boiling of liquid droplets at their superheat limits," Chemical Engineering Science, 60(7), pp. 1809-1821.
[151] Shepherd, J. E., and Sturtevant, B., 1982, "RAPID EVAPORATION AT THE SUPERHEAT LIMIT," Journal of Fluid Mechanics, 121(AUG), pp. 379-402.
[152] Dong, Z. Y., Huai, X. L., and Liu, D. Y., 2005, "Experimental study on the explosive boiling in saturated liquid nitrogen," Progress in Natural Science, 15(1), pp. 61-65.
[153] Hammouda, B., 2010, "A new Guinier-Porod model," Journal of Applied Crystallography, 43, pp. 716-719.
[154] 2002, "Synfluid PAO Databook," Chveron Philips Chemical LP, *Synfluid PAO Databook*.
[155] Lienhard, J. H., and Watanabe, K., 1964, "On Correlating the Peak and Minimum Boiling Heat Fluxes With Pressure and Heater Configuration," Journal of Heat Transfer-ASME, pp. 94-99.
[156] C., G. F., and Kreith, F., 1950, "*Photographic Study of Bubble Formation in Heat Transfer to Subcooled Water*,"JPL Progress Report.

[157] Rule, T. D., and Kim, J., 1999, "Heat transfer behavior on small horizontal heaters during pool boiling of FC-72," Journal of Heat Transfer-Transactions of the Asme, 121(2), pp. 386-393.
[158] Baboi, N. F., Bologa, M. K., and Klyukanov, A. A., 1968, "Some features of ebullition in an electric field," USSR, Appl. Electr. Phenom., pp. 57-70.
[159] Snyder, T. J., Chung, J. N., and Schneider, J. B., 1998, "Competing effects of dielectrophoresis and buoyancy on nucleate boiling and an analogy with variable gravity boiling results," Journal of Heat Transfer-Transactions of the Asme, 120(2), pp. 371-379.
[160] Nishikawa, K., Fujita, Y., Uchida, S., and Ohta, H., 1984, "EFFECT OF SURFACE CONFIGURATION ON NUCLEATE BOILING HEAT-TRANSFER," International Journal of Heat and Mass Transfer, 27(9), pp. 1559-1571.
[161] Chen, L. T., 1978, "HEAT-TRANSFER TO POOL-BOILING FREON FROM INCLINED HEATING PLATE," Letters in Heat and Mass Transfer, 5(2), pp. 111-120.
[162] Yang, S. H., Baek, W. P., and Chang, S. H., 1997, "Pool-boiling critical heat flux of water on small plates: Effects of surface orientation and size," International Communications in Heat and Mass Transfer, 24(8), pp. 1093-1102.
[163] Hampton, M. A., Nguyen, T. A. H., Nguyen, A. V., Xu, Z. P., Huang, L. B., and Rudolph, V., 2012, "Influence of surface orientation on the organization of nanoparticles in drying nanofluid droplets," Journal of Colloid and Interface Science, 377, pp. 456-462.
[164] Lu, J. F., and Peng, X. F., 2007, "Bubble jet flow formation during boiling of subcooled water on fine wires," International Journal of Heat and Mass Transfer, 50(19-20), pp. 3966-3976.
[165] Scriven, L. E., 1959, "ON THE DYNAMICS OF PHASE GROWTH," Chemical Engineering Science, 10(1-2), pp. 1-&.
[166] Scriven, L. E., 1962, "ON THE DYNAMICS OF PHASE GROWTH," Chemical Engineering Science, 17(1), pp. 55-55.
[167] Mikic, B. B., Rohsenow, W. M., and Griffith, P., 1970, "ON BUBBLE GROWTH RATES," International Journal of Heat and Mass Transfer, 13(4), pp. 657-&.
[168] V.P.Carey, 2007, "Liquid Vapor Phase Change Phenomena: An introduction to the Thermophysics of Vaporization and Condensation Processes in Heat Transfer EQUIPMENT," Taylor&Francis.
[169] Shai, I., and Rohsenow, W. M., 1969, "MECHANISM OF AND STABILITY CRITERION FOR NUCLEATE POOL BOILING OF SODIUM," Journal of Heat Transfer, 91(3), pp. 315-&.
[170] Normington, P. J. C., Mahalingam, M., and Lee, T. Y. T., 1992, "THERMAL MANAGEMENT CONTROL WITHOUT OVERSHOOT USING COMBINATIONS OF BOILING LIQUIDS," Ieee Transactions on Components Hybrids and Manufacturing Technology, 15(5), pp. 806-814.
[171] Arik, M., and Bar-Cohen, A., 2010, "Pool boiling of perfluorocarbon mixtures on silicon surfaces," International Journal of Heat and Mass Transfer, 53(23-24), pp. 5596-5604.
[172] Evans, W., Fish, J., and Keblinski, P., 2006, "Role of Brownian motion hydrodynamics on nanofluid thermal conductivity," Applied Physics Letters, 88(9).
[173] Jang, S. P., and Choi, S. U. S., 2004, "Role of Brownian motion in the enhanced thermal conductivity of nanofluids," Applied Physics Letters, 84(21), pp. 4316-4318.
[174] 3M, "Fluorinert™ Electronic Liquid FC-72 Product Information."
[175] Watson, E. S., and O'Neill, M. J., 1962, "U.S. Patent 3,263,484."
[176] Kotlarchyk, M., Chen, S. H., and Huang, J. S., 1982, "TEMPERATURE-DEPENDENCE OF SIZE AND POLYDISPERSITY IN A 3-COMPONENT MICRO-EMULSION BY SMALL-ANGLE NEUTRON-SCATTERING," Journal of Physical Chemistry, 86(17), pp. 3273-3276.